CERN-THESIS-2008-231

SINGLE TOP PRODUCTION
ASPECTS OF PERTURBATIVE QCD

ACADEMISCH PROEFSCHRIFT

ter verkrijging van de graad van doctor
aan de Universiteit van Amsterdam
op gezag van de Rector Magnificus
prof. dr. D.C. van den Boom
ten overstaan van een door het college voor promoties
ingestelde commissie,
in het openbaar te verdedigen in de Agnietenkapel
op vrijdag 25 januari 2008, te 14:00 uur

door

Patrick Motylinski

geboren te Århus, Denemarken

Promotor: Prof. dr. E.L.M.P. Laenen

Faculteit der Natuurwetenschappen, Wiskunde en Informatica

To my parents Jerzy and Zdzisława Urszula

Contents

The material presented in this thesis is based on the following publications:

chapter 2
R. Basu, E. Laenen, A. Misra and P. Motylinski, Phys. Rev. D **76** (2007) 014010 [arXiv:0704.3180 [hep-ph]].

chapter 4
S. Frixione, E. Laenen, P. Motylinski and B. R. Webber, JHEP **0603** (2006) 092 [arXiv:hep-ph/0512250].

chapter 5
S. Frixione, E. Laenen, P. Motylinski and B. R. Webber, JHEP **0704** (2007) 081 [arXiv:hep-ph/0702198].

chapter 6
S. Frixione, E. Laenen, F. Maltoni, P. Motylinski, B. R. Webber and C. White "Single-top production through the Wt mode" (***in preparation***)

Introduction

The Standard Model of particle physics will soon be celebrating its 40 year anniversary. It describes three of the fundamental forces of nature: the strong force, the weak force and the electromagnetic force. The gravitational force is not described by the Standard Model. It is a remarkably successful theory in that almost all its predictions have been verified experimentally.
The model incorporates particles of matter which are all spin-1/2 particles, i.e. fermions. These matter-particles interact with each other through exchange of force-carrying spin-1 particles, i.e. bosons. So far all particles, except for one, have been discovered. The one still missing is the Higgs particle (or Higgs boson). The Standard Model is a non-abelian gauge theory, based on the symmetry group

$$SU(3)_{strong} \times SU(2)_{I_W} \times U(1)_{Hypercharge} \tag{1}$$

The labels refer to the three fundamental forces described by the Standard Model, in the sense that the spin-1 gauge particles associated with each symmetry group factor are precisely the force-mediators. Although the symmetries in (1) are symmetries of the interactions, the Standard Model posits that it is not a symmetry of the ground state. This is known as spontaneous symmetry breaking. Its consequenses are among others, that the weak force-mediators $W^{\pm}$ and Z become massive whereas the photon remains massless. Accordingly, part of the SM symmetry is broken as follows

$$SU(2)_{I_W} \times U(1)_{Hypercharge} \rightarrow U(1)_{electromagn.} \tag{2}$$

The energy scale associated with the breaking is $v = 246\text{GeV}$ at which the Higgs field acquires a vacuum expectation value.

The Top Quark

The top quark was, in a sense, seen before it was discovered in 1995 [1, 2]. With its mass of around $m_t = 171\text{GeV}$ it is by far the heaviest Standard Model particle. This separates it from the other fermions in the model, due to different decay

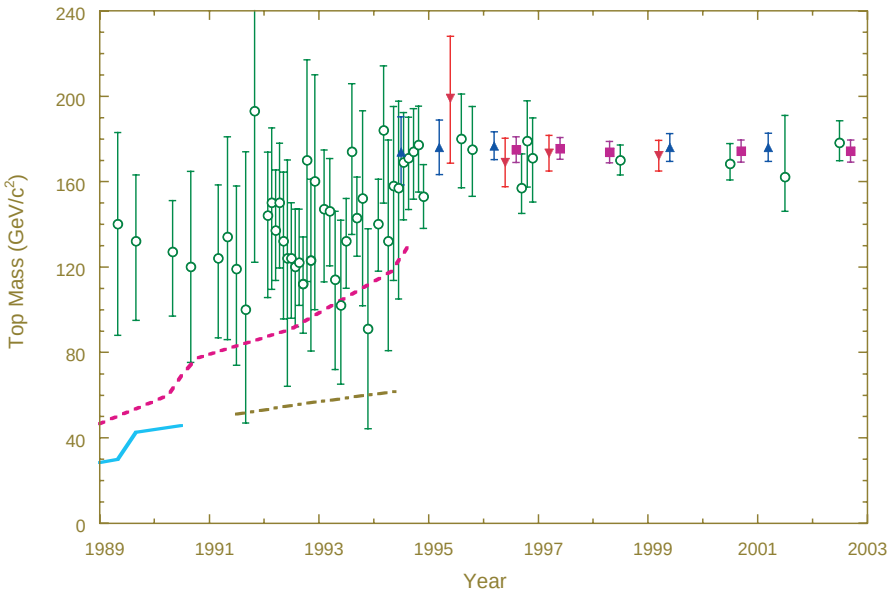

Figure 1: Figure showing the predicted top mass (before 1995) and the top mass after the discovery in 1995.

properties.
The indirect discovery was possible due to the following prediction of the Standard Model: certain precision measurements are very sensitive to the mass of the top quark. The ρ-parameter [3] is to leading order given by:

$$\rho = \frac{M_W^2}{M_Z^2 \cos^2 \theta_W} = 1 \tag{3}$$

where M_W is the mass of the W-boson, M_Z the mass of the Z-boson and θ_W the Weinberg-angle. To one-loop the parameter is given by approximately

$$\rho \simeq 1 + \frac{3G_F m_t^2}{8\sqrt{2}\pi^2} \tag{4}$$

where G_F is the weak coupling constant. By comparing this equation with accurate data it was possible to constrain the top mass quite well. In fig. 1 we see how the top mass was inferred prior to its discovery as well as after the discovery in 1995. The processes that are particularly sensitive to the top mass are depicted in fig. 2.
The top quark was discovered at Fermilab in 1995 by both the CDF and the D0 experiment [1, 2] by studying top pair production. In these reactions pairs of tops and anti-tops are produced via the strong interaction.
In December 2006 Fermilab released a press statement claiming a three sigma

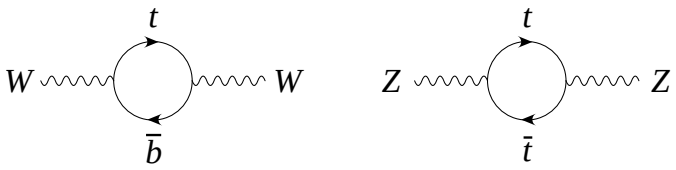

Figure 2: Figure showing corrections to the ρ-parameter involving the top quark.

evidence of single top production[1]. Compared with the $t\bar{t}$-production the single-top has a small cross section at the energies available at Tevatron which, together with a difficult background, makes the search for single-top events very difficult. Thus the physics community looks also for this reason with great expectations to the Large Hadron Collider (LHC) at CERN, which is expected to be capable of producing top quarks (in both $t\bar{t}$ and single-top events) at much higher rates than before.

Single Top Production

The single top process is the main subject of this dissertation. Its experimental discovery will be crucial in the further study of the Standard Model, and it could very well be a gateway to physics beyond the Standard Model. Here we are going to present some motivations for studying the single top process.

The Higgs boson couples to both left- and right-handed fermions, hence also quarks, in the Standard Model. The coupling between the Higgs boson and the top quark is a Yukawa coupling, y_t. The corresponding mass term in the lagrangian density for the top quark can be expressed in terms of y_t and the electroweak symmetry breaking scale v, i.e.

$$m_t \bar{t}t = \frac{y_t v}{\sqrt{2}} \bar{t}t \tag{5}$$

Since $m_t \simeq 171\text{GeV}$ and $v \simeq 246\text{GeV}$, which is the electroweak symmetry breaking scale, we see that the top-Yukawa coupling is of order unity. This means that the top quark couples strongly to the Higgs field or to whatever else might break the EW symmetry, if not the Higgs mechanism. This makes the top quark very important in the search and study of the Higgs boson.

The Standard model predicts that the coupling of the top quark to the W-field is of the form

$$\frac{g_w}{\sqrt{2}} V_{tq} (\bar{t} \gamma^\mu q_L) W_\mu^+ \tag{6}$$

[1]Single-tops, i.e. without their anti-partner can be produced via the weak interaction.

where V_{tq} is the CKM matrix element describing the mixing between a top quark and another d-type quark, and g_w is the electroweak coupling constant. We see that the predicted coupling is flavour changing and purely left-handed. This means that the top quark in a single-top process should be purely polarized when produced. A further advantage of the top quark is its mass, which is so large that, in contrast to other quarks in the Standard Model, it decays before it has a chance to hadronize. This means that by studying the decay products of the top quark the suggested polarization can be measured directly. The feasibility of this is further boosted by the fact that the top quark has a strong angular correlation with its decay products (discussed in chapter 5). A direct measurement of the single-top processes would allow for verification of this, and hence adds to the importance of the study of single-top physics.
The top couples to the Z-field through a flavour preserving coupling of the form

$$\frac{g_w}{4\cos\theta_w}\bar{t}\left((1-\frac{8}{3}\sin^2\theta_w)\gamma^\mu-\gamma^\mu\gamma^5\right)tZ_\mu \tag{7}$$

An interesting scenario is that, at sufficiently high energies, the top quark would couple to a, hitherto unknown, flavour changing neutral currents, i.e. with a coupling of the form

$$G\bar{t}\left(k_1\gamma^\mu+k_2\gamma^\mu\gamma^5\right)uW^* \tag{8}$$

where W^* is a flavour changing field that is heavier than the W and Z. Again, a direct measurement on the single-top process would allow for verification of the existence of such a channel.

Assuming that there are only three generation of quarks and that the CKM matrix is unitary we already know that the CKM matrix is given by

$$V_{CKM}=\begin{pmatrix} 0.9739-0.9751 & 0.221-0.227 & 0.0029-0.0045 \\ 0.221-0.227 & 0.9730-0.9744 & 0.039-0.044 \\ 0.0048-0.014 & 0.037-0.043 & 0.9990-0.9992 \end{pmatrix} \tag{9}$$

and thus the V_{tb} is the best known of the matrix elements. If, however, there would be a fourth generation of quarks we are forced to slack on the constraint on V_{tb} [4] in that we only know that

$$V_{tb}=0.11-0.9992$$

This means, that if a value of V_{tb} considerably below 1 would be measured then we enter the realm of new physics. A way of measuring V_{tb} directly is the following. First one extracts the branching ratio of a top decaying into a b-quark and a

W-boson by "comparing" the experimentally measured $t\bar{t}$-cross section with the theoretically calculated cross section, i.e.

$$\sigma_{t\bar{t}}^{experimental} = \sigma_{t\bar{t}}^{theoretical} \mathrm{Br}[t \to bW]^2 \tag{10}$$

Having extracted $\mathrm{Br}[t \to bW]$, V_{tb} can be measured by a similar comparison between the experimental and theoretical cross section, this time for the single-top process

$$\sigma_{t}^{experimental} = \sigma_{t}^{theoretical} |V_{tb}|^2 \mathrm{Br}[t \to bW] \tag{11}$$

We see that the measurement of V_{tb} is rather sensitive the amount of statistics available, the precise measurement of $\mathrm{Br}[t \to bW]$ and the accuracy of the theoretical cross sections.
But before entering top quark physics we consider certain aspects of perturbation theory.

References

[1] F. Abe et al. Observation of top quark production in anti-p p collisions. *Phys. Rev. Lett.*, 74:2626–2631, 1995.

[2] S. Abachi et al. Observation of the top quark. *Phys. Rev. Lett.*, 74:2632–2637, 1995.

[3] D. A. Ross and M. J. G. Veltman. Neutral currents in neutrino experiments. *Nucl. Phys.*, B95:135, 1975.

[4] Johan Alwall et al. Is v(tb) = 1? *Eur. Phys. J.*, C49:791–801, 2007.

Chapter 1

Perturbation Theory And Resummation

In present-day particle physics we are interested in methods that allow for optimal calculation of cross sections. This is a highly non-trivial task. At hadron colliders we face the problem that on the one hand we measure hadronic cross sections but on the other hand we are only able to calculate the partonic (quarks and gluons) cross section using Feynman rules. The translation from hadron level to parton level thus demands a description that carries predictive power. The required understanding of this translation is contained in so-called parton distribution functions (PDF's). How the partons are distributed within a hadron is governed by low energy dynamics whereas the partonic collision is a high-energy process. Hence we have to separate *long-distance* from *short-distance effects*. Because of *asymptotic freedom* (see below) the latter are in principle calculable in perturbation theory whereas the former are not. Factoring out the PDF's the short-distance part of the cross section, also called the hard part, remains. Predictive power now rests upon the PDF's being universal, allowing their inference from other processes, as well as the hard part being calculable. The quality of the prediction then is determined to a large extent by how well the hard part can be calculated in perturbation theory. The key is that this factorization holds to all orders in perturbation theory [1, 2]. Below we shall not review the proof of this factorization, but rather make it plausible.

Let us begin by describing the simple parton model. In the centre-of-mass (CM) frame the colliding hadrons are Lorentz contracted. At the same time the dynamics of the residing partons is subject to time dilation. The partons of one hadron have very little time to interact with those of the other, whose dynamics are, in addition, slowed down by time dilation. Thus partons in one of the hadrons view the partons in the other as non-interacting. The struck partons will have a certain momentum fraction, x, of the hadron in which they reside, with $0 < x < 1$.

One defines a parton distribution $f_{a/H}(x)$ as the probability that a parton of type a in hadron H is encountered with momentum fraction x. Summing over all parton species and allowed momentum fractions, the parton model cross section becomes

$$\sigma_{\text{Hadronic}} = \sum_{i,j} \int dx_1 dx_2 f_i(x_1) f_j(x_2)\, \sigma_{\text{Partonic}}(x_1, x_2) \tag{1.1}$$

The QCD factorization theorem now states that, when one includes perturbative QCD interactions the formula becomes

$$\sigma_{\text{Hadronic}} = \sum_{i,j} \int dx_1 dx_2 f_i(x_1, \mu^2) f_j(x_2, \mu^2)\, \sigma_{\text{Partonic}}(x_1, x_2, Q, \mu, \alpha_s(\mu)) + \mathcal{O}\left(\frac{\Lambda^2}{Q^2}\right) \tag{1.2}$$

The structure of eqn. (1.1) is essentially unchanged, up to the indicated power corrections $\mathcal{O}(\Lambda^2/Q^2)$, and predictive power is present. The PDF's are in fact shown to be universal and the partonic cross section written here is in principle calculable to all orders in perturbation theory. In practice this is an impossible task. In QCD the task becomes even more difficult due to the peculiar nature of the strong coupling, α_s which is not fixed but scale dependent. The scale dependence is such that α_s increases when the scale becomes small, and decreases as the scale grows. The latter is called *asymptotic freedom* [3, 4]. Since the coupling constant, used as an expansion parameter, is large for small energy scales it becomes very questionable to approach the problem perturbatively. Thus, in many cases involving low energy QCD, not involving collider observables, it is possible to apply lattice gauge methods. For higher energy scales, which are relevant for the physics described here, the coupling constant is sufficiently low that one has good reason to use perturbation theory. Perturbation theory however quickly reveals its limitations as one goes up in order with respect to α_s. For each order the number of diagrams that needs to be calculated grows exponentially, and often the integrals that need to be solved when considering the virtual components become very cumbrous. However, experience shows that many leading order calculations already are close to the experimental measurements. To verify that the perturbative approach is plausible it is, however, in most cases necessary to go at least one order up in perturbation theory. Even though considerable improvement in making predictions is achieved by going beyond one or two orders beyond leading order there are situations that remain poorly described by this procedure. One example of this is prompt photon production, which we discuss later.

It can happen that certain parts of the full higher order calculation for some observable become (very) large in some kinematical regime. One example is the emission of soft photon/gluon radiation near a kinematic threshold so that this

radiation must be soft. Typically at some fixed order in the higher order calculation there will be a series of logarithms of ratios of energy scales, that will be considerably larger than the other terms in the expansion at that order. For example, when the kinematical limit is a threshold the logarithms of ratios of the small radiation energy and the large threshold energy become large.

Resummation deals with the summation of large logarithms[1] to all orders. When these logarithms become large perturbation theory loses its predictive power. It has been shown that within certain kinematical limits it is possible to sum leading and sub-leading logarithmic contributions to all orders. Some of these scenarios are considered in this and the subsequent chapter. Thus, to sketch, resummation arranges the large logarithms as follows:

$$\begin{aligned} d\sigma =& 1 + \alpha_s(L^2 + L + 1) + \alpha_s^2(L^4 + L^3 + L^2 + L + 1) + \cdots \\ =& \exp\left(\underbrace{\underbrace{L\underbrace{g_1(\alpha_s L)}_{LL} + g_2(\alpha_s L) + \alpha_s g_3(\alpha_s L)}_{NLL}}_{} \right) \underbrace{C(\alpha_s)}_{\text{constants}} \\ &+ \cdots \end{aligned} \tag{1.3}$$

where L is the potentially large logarithm, and "1" represents other, non-logarithmic terms. The g_i are suitable functions, examples of which are discussed later in this chapter. The reader may now view resummation as a possibly incomplete approach to perturbation theory. But this is not the case. It should be viewed as complimentary to fixed-order perturbation theory. Note that the accuracy of the resummation may be parametrically improved from Leading Logarithmic (LL) to Next-to-Leading Logarithmic (NLL) etc, as indicated in eqn. (1.3).

1.1 Sudakov Enhancement And Suppression

One of the most clear-cut arguments in favour of using resummation becomes apparent when Sudakov enhancement and suppression is considered. First we motivate the discussion with a physical argument. Near threshold it becomes less probable that soft gluons will be emitted since the phase space is limited. This is known as Sudakov suppression. Thus the near-threshold hadronic cross section for prompt photon production should fall off. This is a well-known observed effect, and can be reproduced in theoretical predictions by resummation. The partonic cross section may however be enhanced in threshold resummation, and predict signifantly larger cross sections than a low order calculation. Here we discuss why

[1] The term resummation is not limited to (re)-summation of logarithms only.

this may be so. When performing a next-to-leading order (NLO) calculation it is necessary to introduce plus-distributions, defined by

$$\left(\frac{f(x)}{(1-x)}\right)_+ = \frac{f(x)}{1-x} - \delta(1-x)\int_0^1 dx' \frac{f(x)}{1-x'} \tag{1.4}$$

which only have meaning when integrated with a smooth test function. The finite, subtracted NLO cross section can be written as

$$\frac{d\hat{\sigma}^{(1)}}{dQ^2} = \frac{d\sigma^{(1)}}{dQ^2}(\epsilon) - 2\phi^{(1)}(\epsilon) \tag{1.5}$$

where the ϵ-dependence here symbolizes the divergent parts. The LHS is not ϵ-dependent by which we imply that it is finite. Now the leading logarithm in the first term, when written out explicitly, becomes

$$\alpha_s C_F\left(\frac{1}{1-x}\int_0^{Q^2(1-x)^2}\frac{d\lambda}{\lambda^{1+\epsilon}} - \delta(1-x)\int_0^1\frac{dx'}{1-x'}\int_0^{Q^2(1-x)^2}\frac{d\lambda}{\lambda^{1+\epsilon}}\right) \tag{1.6}$$

while in the second it can be written as:

$$-\alpha_s C_F\left(\frac{1}{1-x}\int_0^{\mu_F^2}\frac{d\lambda}{\lambda^{1+\epsilon}} - \delta(1-x)\int_0^1\frac{dx'}{1-x'}\int_0^{\mu_F^2}\frac{d\lambda}{\lambda^{1+\epsilon}}\right) \tag{1.7}$$

The resummed prediction will contain these expressions in the exponent. The upper limit in the λ-integral is in the first formula dictated by phase space, in the latter by factorization scale. In both cases we see that the second term can be interpreted as a *virtual* gluon emission since the δ-function ensures that $x = 1$. What is apparent from the expressions is that the presence of virtual gluons lowers the probability of having no extra emissions. Thus, virtual gluons cause, in general, Sudakov suppression. We see that in the subtraction (1.5) the (negative) virtual gluon contribution from the unsubtracted hard part PDF's is oversubtracted, leading to Sudakov enhancement for $\hat{\sigma}$. In other terms the gluons are responsible for an over-subtraction (Sudakov suppression) which the partonic cross section has to compensate for. Thus, schematically we have

$$\underbrace{\sigma_{\text{Hadron}}}_{\text{Sudakov suppressing}} \sim \underbrace{\phi}_{\text{Sudakov suppressing}} \times \underbrace{\phi}_{\text{Sudakov suppressing}} \times \underbrace{\hat{\sigma}}_{\text{Sudakov enhancing}} \tag{1.8}$$

Note that in this expression the PDF's may be evaluated at different scales. Their scale dependence is in fact calculable, as we now briefly discuss.

1.2 Parton Evolution

The scale-dependence of Mellin transforms of quark and gluon distributions is given by the renormalization group equation

$$\mu\frac{\partial}{\partial\mu}q_i(N,\mu) = \frac{\alpha_s(\mu)}{2\pi}\gamma_{q_iq_j}(N,\alpha_S(\mu))q_j(N,\mu) \tag{1.9}$$

The functions $\gamma_{p_1p_2}$ are *anomalous dimensions* of certain composite parton operators. They are related to the Altarelli-Parisi [5] splitting functions $P_{p_1p_2}$ by

$$\gamma_{p_1p_2} = -\int_0^1 dx\, x^{N-1}P_{p_1p_2}(x,\alpha_s) \tag{1.10}$$

This transformation from x to N space (N may be complex) is known as a Mellin transform, about which more later. The $P_{p_1p_2}$ are to be interpreted as the probability densities of finding a parton p_1 in a parton of type p_2 with momentum fraction x of the longitudinal parent-parton momentum. At leading order the anomalous dimensions have expansions in terms of N, and are given by

$$\begin{aligned}\gamma_{qq}^{\mathrm{LO}} &= -\alpha_s C_F\left(\frac{1}{2} - \frac{1}{N(N+1)} + 2\sum_{k=2}^{N}\frac{1}{k}\right)\\ \gamma_{qg}^{\mathrm{LO}} &= -\alpha_s T_R\left(\frac{(2+N+N^2)}{N(N+1)(N+2)}\right)\end{aligned} \tag{1.11}$$

There are $2f+1$ partons to keep track of (f quark flavours, f anti-quark flavours and 1 gluon). By combining these into non-singlet and singlet combinations the $2f+1$ by $2f+1$ set of coupled equations are reduced to solving $2f-1$ uncoupled equations plus a coupled set of 2 equations

$$\begin{aligned}\mu\frac{\partial}{\partial\mu}\begin{pmatrix}\Sigma(N,\mu)\\ g(N,\mu)\end{pmatrix} =& \frac{\alpha_s(\mu)}{2\pi}\times\\ &\begin{pmatrix}\gamma_{qq}(N,\alpha_s(\mu)) & 2f\gamma_{qg}(N,\alpha_s(\mu))\\ \gamma_{gq}(N,\alpha_s(\mu)) & \gamma_{qq}(N,\alpha_s)\end{pmatrix}\begin{pmatrix}\Sigma(N,\mu)\\ g(N,\mu)\end{pmatrix}\end{aligned} \tag{1.12}$$

from a set of initial distributions at some reference scale μ_0. Here $\Sigma \equiv \sum_i(q_i+\bar{q}_i)$ is the so-called singlet contribution. Solving eqs. (1.9) and (1.12) allows for evaluation of the PDF's at an arbitrary scale. Numerical solutions most often use momentum space, but this may also be profitably done in complex N space [6].

1.3 Exponentiation

In general resummation deals with finding functions $g_1, g_2, \ldots$ so that if we have large logarithmic corrections L we can take these into account by writing

$$\sigma = C(\alpha_s)\,\exp(Lg_1(\alpha_s L) + g_2(\alpha_s L) + \alpha_s g_3(\alpha_s L) + \ldots) + \ldots \tag{1.13}$$

We shall see explicit realizations of this expression later in this section. To first clarify the pattern of radiative corrections due to infrared emissions that lead to exponentiation we examine emissions of photons which, unlike gluons, are not complicated by colour structures. In Quantum Electrodynamics (QED) infrared singularities arise from soft photons, where soft means having energy low with respect to some suitable cut-off.

Why do soft radiation effects exponentiate? We consider a hard QED process [7] with an incoming electron of momentum p and an outgoing electron with momentum p'. Starting with the outgoing leg, consider n photons that are radiated off with corresponding momenta $k_1, \ldots, k_n$, and which are assumed to be soft. This leads to the following expression:

$$\begin{aligned}\bar{u}(p')(-ie\gamma^{\mu_1})\frac{i(\not{p}' + \not{k}_1 + m)}{2p'\cdot k_1}(-ie\gamma^{\mu_2})\cdots \\ (-ie\gamma^{\mu_n})\frac{i(\not{p}' + \not{k}_1 + \cdots \not{k}_n + m)}{2p'\cdot(k_1+\cdots k_n)+i\epsilon}(i\mathcal{M}_{\rm hard})\end{aligned} \tag{1.14}$$

Since we assumed the emissions to be soft we neglect the k's in the numerators and keep only the lowest power of k in the denominators (this is known as the eikonal approximation). Using the Dirac equation the expression in eqn. (1.14) becomes

$$\bar{u}(p')\left(e\frac{p'^{\mu_1}}{p'\cdot k_1}\right)\cdots\left(e\frac{p'^{\mu_n}}{p'\cdot(k_1+\cdots+k_n)}\right)\mathcal{M}_{\rm hard} \tag{1.15}$$

There are $n!$ diagrams to sum and hence $n!$ permutations to take into account, and it can be shown[2] that summing over all possible permutations eqn. (1.15) yields

$$\bar{u}(p')\left(e\frac{p'^{\mu_1}}{p'\cdot k_1}\right)\cdots\left(e\frac{p'^{\mu_n}}{p'\cdot k_n}\right)\mathcal{M}_{\rm hard} \tag{1.16}$$

By similar means one can include the effect of the initial state radiation. Since the propagators for the incoming electron line are $p-k_1, \ldots, p-\sum_i k_i$ one can show that the expression in eqn. (1.16) modifies to:

$$\big[\bar{u}(p')\mathcal{M}_{\rm hard}u(p)\big]e\left(\frac{p'^{\mu_1}}{p'\cdot k_1}-\frac{p^{\mu_1}}{p\cdot k_1}\right)\cdots e\left(\frac{p'^{\mu_n}}{p'\cdot k_n}-\frac{p^{\mu_n}}{p\cdot k_n}\right) \tag{1.17}$$

[2] One uses the identity $\frac{1}{p'\cdot k_1}\frac{1}{p'\cdot(k_1+k_2)}+\frac{1}{p'\cdot k_2}\frac{1}{p'\cdot(k_1+k_2)}=\frac{1}{p'\cdot k_1}\frac{1}{p'\cdot k_2}$ and its generalizations.

Calculating the cross section we need to multiply with the complex conjugate amplitude, with the photon polarization vectors, sum over polarizations, integrate over the photon phase space, and include a symmetry factor $1/n!$. For each photon momentum we get a factor of the form

$$\mathcal{R} = \int \frac{d^3k}{(2\pi)^3}\frac{1}{2k}e^2(-g_{\mu\nu})\left(\frac{p'^\mu}{p'\cdot k} - \frac{p^\mu}{p\cdot k}\right)\left(\frac{p'^\nu}{p'\cdot k} - \frac{p^\nu}{p\cdot k}\right) \tag{1.18}$$

$$= e^2 \int \frac{d^3k}{(2\pi)^3}\frac{1}{2k}\frac{p\cdot p'}{(p\cdot k)\,(p'\cdot k)} \tag{1.19}$$

Hence if n are emitted one gets n such factors and thus after summing one finds

$$\sum_{n=0}^{\infty}\frac{d\sigma}{d\Omega}(\mathbf{p}\to\mathbf{p}'+n\gamma) = \frac{d\sigma}{d\Omega}(\mathbf{p}'\to\mathbf{p})\sum_{n=0}^{\infty}\frac{1}{n!}\mathcal{R}^n = \frac{d\sigma}{d\Omega}(\mathbf{p}'\to\mathbf{p})\,\exp(\mathcal{R}) \tag{1.20}$$

Parametrizing $k^\mu = E(1,0,\sin\theta,\cos\theta)$, where θ is the angle between $\vec{p}$ and $\vec{k}$, eqn. (1.18) becomes for small E and small θ (i.e. for soft and collinear radiation)

$$\mathcal{R} \sim \int^{E_{cut}} \frac{dE}{E}\frac{d\theta}{\theta} \tag{1.21}$$

The leading form of $\mathcal{R}$ is

$$\mathcal{R} \sim \ln^2\left(E_{cut}^2\right) \tag{1.22}$$

In a similar way it is possible to show that the virtual contributions also exponentiate. The real and virtual contribution can then be combined in the exponent.

1.3.1 QCD and Colour Factors

We have in the above only considered the abelian case of QED. The generators of the strong interaction gauge group, which are present in each vertex of the graph, constitute, however, a non-abelian algebra. Therefore, at first glance, it seems far from obvious that one can obtain similar results by replacing the photons with gluons. Nevertheless, this is possible [8, 9, 10].

Non-abelian eikonal exponentiation deals with including colour structure in the exponentiation of the (potentially) divergent contributions stemming from soft gluon radiation. One can show that the sum of virtual and real eikonal gluon diagrams can be written as the exponent of a specific subset of them with modified colour structure (so-called *webs*). To illustrate this, consider the virtual diagrams in fig. 1.1. We denote the colour of graph b by $C(\,|\,)$ etc. The colour structures

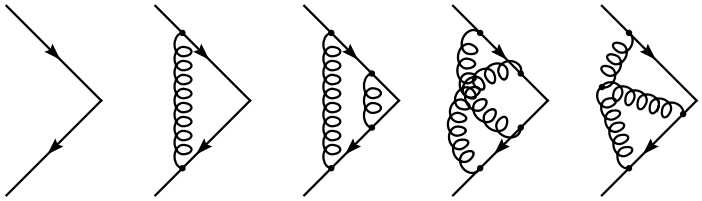

Figure 1.1: Virtual eikonal diagrams of zeroth, first and second order.

obey relations

$$\begin{aligned} C(\,|\,|\,) &= C(\,|\,)^2 \\ C(\,\times\,) &= C(\,|\,|\,) + C(\,\curlywedge\,) = C(\,|\,)^2 + C(\,\curlywedge\,) \\ &\vdots \end{aligned} \tag{1.23}$$

where $C(\,|\,) = C_F$ and $C(\,\times\,) = -C_A C_F/2$. At the same time the eikonal approach for the momentum part of the amplitudes leads to the pattern we saw in the previous section. Combining the various parts of the eikonal factors with their relevant colour weights leads to exponentiation

$$\exp\Big(C(\,|\,)F(\,|\,) + C(\,\curlywedge\,)F(\,\times\,)\Big) \tag{1.24}$$

For real emissions a similar exponentiation holds. Via a Laplace transform [3] we can fix the energy of the emitted radiation. Expressing the contribution from the webs in terms of the function $w(k)$ the result may be written as

$$\exp\Big[\int \frac{d^d k}{(2\pi)^d} w(k^2, k^+k^-, \alpha(\mu^2), \mu^2, \epsilon)\,(e^{-N(k^0/Q)} - 1)\Big] \tag{1.25}$$

where the real and virtual contributions are proportional to $\exp(-N(k^0/Q))$ and -1 respectively. Such an exponentiation is at the heart of QCD resummed cross sections.

1.4 Convolution And Mellin Transforms

When calculating hadronic cross sections it is necessary to get acquainted with the concepts of convolution and Mellin transforms. For definiteness, let us temporarily

[3] Equivalent here to a Mellin transform up to $\mathcal{O}(1/N)$ terms.

consider the inclusive production of a vector boson of mass Q in hadronic collisions, via the partonic process

$$q_i(p_1) + q_j(p_2) \to V(Q) + X \tag{1.26}$$

where X is any extra radiation at the parton level. The factorization theorem expresses the hadronic cross sections as a convolution beween the parton distribution functions and the hard (partonic) sub-process as follows

$$\begin{aligned}\sigma_{\text{Hadronic}}(\tau = \frac{Q^2}{S}, P_1, P_2) = &\sum_{i,j} \int_\tau^1 dx_1 dx_2 f_i(x_1, \mu_F^2) f_j(x_2, \mu_F^2) \\ &\times \sigma_{\text{Partonic}}(p_1, p_2, \alpha_s(\mu_R^2), Q^2/\mu_R^2, , Q^2/\mu_F^2) + \mathcal{O}(\Lambda^2/Q^2)\end{aligned} \tag{1.27}$$

Here P_1 and P_2 are the momenta of the incoming hadrons, and are related to p_1 and p_2 by the relations $p_i = x_i P_i$, for $i \in \{1, 2\}$. The process dependent scale of the hard interaction is given by Q and the scales μ_R and μ_F are the renormalization and factorization scale, respectively. Furthermore, the functions $f_{1,2}$ are the parton distribution functions. Finally, σ_{Partonic} is the cross section for the scattering of the partons 1 and 2. As mentioned in the beginning of this chapter this function is also called the short distance cross section, since it describes typically hard (high momentum) cross sections. Here it is appropriate to say a few words about the factorization scale, μ_F. The factorization scale separates long-distance physics from short-distance physics. This can be qualitatively understood in the following way. An emitted parton carrying large transverse momentum should belong to the short-distance cross section, whilst a low transverse momentum parton should be seen as part of the internal structure of the hadron. The scale μ is most often chosen to be equal to, or close to the characteristic hard scale, Q, in order to avoid unnecessary large logs $\ln(\mu_F/Q)$.

A useful tool in dealing with factorization is the already mentioned Mellin transform, whose definition is

$$(Mf)(N) \equiv \phi(N) = \int_0^1 x^{N-1} f(x) dx \tag{1.28}$$

i.e. it amounts to take the N'th moment of f. The inverse of the transform is given by

$$(M^{-1}\phi)(x) = f(x) = \frac{1}{2\pi i} \int_{c-i\infty}^{c+i\infty} x^{-N} \phi(N) dN \tag{1.29}$$

where c lies in the complex N-plane to the right of all singularities. The form of the factorization theorem ensures that when applying the Mellin transform

with respect to τ to the hadronic cross section in eqn. (1.34) it changes from a convolution to a product

$$\begin{aligned}(M\sigma_{\text{Hadronic}}(N,P_1,P_2)) = &\sum_{i,j} f_i(N,\mu^2) f_j(N,\mu^2) \\ &\times \sigma_{\text{Partonic}}(N,\alpha_s(\mu^2),Q^2/\mu^2)\end{aligned} \tag{1.30}$$

where for convenience we have put $\mu_F = \mu_R = \mu$ and omitted the power corrections. The leading large logarithms that occur when considering n emissions near threshold in momentum space are the particular plus-distributions (see eqn. (1.4))

$$\alpha_s^n \left[\frac{\ln^{2n-1}(1-z)}{1-z}\right]_+ \tag{1.31}$$

where $z = \tau/x_1x_2$. After a Mellin transform these become $\alpha_s^n \ln^{2n} N$ plus terms subleading in powers of $\ln N$. Threshold is approached by increasing N.

1.5 Threshold Resummation

Threshold resummation involves summing the radiative effects of bremsstrahlung due to a production threshold. For definiteness and with an eye to later application we discuss threshold resummation here for the case of prompt photon production, which is defined at lowest order by the partonic reaction

$$a(p_b) + b(p_b) \to \gamma(p_\gamma) + c(p_c) \tag{1.32}$$

where a, b can be $q\bar{q}$, qg or $\bar{q}g$. We shall discuss the phenomenological importance of this process in section 1.8 below. Here, it suffices to say that we wish to detect a photon at a fixed transverse momentum p_T, so that the energy threshold for this process is $2p_T$. Accordingly, let $x_T^2 \equiv 4p_T^2/S$ ($x_T^2 < 1$) be the hadronic scaling variable, and $\hat{x}_T^2 \equiv 4p_T^2/\hat{s}$ the analogous partonic scaling variable ($x_T^2 < \hat{x}_T^2 < 1$). S is the hadronic centre-of-mass energy, p_T of the produced particle and $\hat{s} = x_a x_b S$ is the partonic centre-of-mass energy squared. Near threshold the phase space for bremsstrahlung is rather constrained. This limitation manifests itself by introducing large logarithmic corrections (due to soft and collinear radiation) to the cross section.

Having introduced the relevant variables we are now ready to state the resummed expression for the cross section. The threshold-resummed p_T distribution for prompt photon production stemming from hadron collisions is, to leading power

in p_T^2/S, given by [11, 12, 13]

$$\begin{aligned}\frac{p_T^3 d\sigma_{AB\to\gamma+X}^{(\text{resum})}}{dp_T} =& \sum_{ab} \frac{p_T^4}{8\pi S^2} \int_{\mathcal{C}} \frac{dN}{2\pi i} f_{a/A}(N,\mu_F) f_{b/B}(N,\mu_F) \\ &\times \underbrace{C_{ab\to\gamma}(\alpha_s) \times \exp(E_{ab\to\gamma c}(N))}_{\text{Partonic cross section, } \hat{\sigma}}\end{aligned} \tag{1.33}$$

The variable N is Mellin-conjugate to x_T^2. The exponent is further resolved as

$$\exp(E_{ab\to\gamma c}(N)) = \exp(E_a + E_b + F_c + G_{abc}) \tag{1.34}$$

where E_a, E_b are exponents containing the N-dependent soft and collinear logarithms from the initial state partons, F_c contains final state logarithms and G_{abc} controls soft wide-angle radiation. The function E_i takes, to NLL accuracy, the form

$$\begin{aligned}E_i(N,Q,\mu_F) =& -\int_{Q^2/\bar{N}}^{Q^2} \frac{dk_T^2}{k_T^2} \Big\{ A_i(\alpha_s(k_T)) \ln\left(\frac{Q}{k_T}\right) + B_i(\alpha_s(k_T)) \Big\} \\ &+ \int_{\mu_F^2}^{Q^2/\bar{N}} \frac{dk_T^2}{k_T^2} \big\{ -\ln \bar{N} A_i(\alpha_s(k_T)) - B_i(\alpha_s(k_T)) \big\}\end{aligned} \tag{1.35}$$

where $\bar{N} = N\exp(\gamma_E)$. The function A is given by

$$\begin{aligned}A_a(\alpha_s) =& \sum_k \left(\frac{\alpha_s}{\pi}\right)^k A_a^{(k)} \\ A_a^{(1)} =& C_a \\ A_a^{(2)} =& \frac{1}{2} C_a K = \frac{1}{2} C_a \left[C_A \left(\frac{67}{18} - \frac{\pi^2}{6} \right) - \frac{10}{9}\, T_R N_f \right]\end{aligned} \tag{1.36}$$

where we have listed the terms of the "cusp anomalous dimension" A_a up to 2nd order [14] necessary for NLL calculations. Furthermore we have that $C_q = C_F$ and $C_g = C_A$. We only need the first term in $B_a = (\alpha_s/\pi)B^{(1)} + \mathcal{O}(\alpha_s^2)$

$$B_q^{(1)} = -\frac{3}{4} C_F, \quad B_g^{(1)} = -\pi b_0 \tag{1.37}$$

where $b_0 = (11C_A - 2n_f)/12\pi$. Performing the integration in eqn. (1.35) gives:

$$E_i(N,Q,\mu_F) = \frac{1}{\alpha_s(\mu)} h_i^{(0)}(\lambda) + h_i^{(1)}(\lambda, Q, \mu, \mu_F) \tag{1.38}$$

where $\lambda = b_0\alpha_s \ln \bar{N}$, $\bar{N} = Ne^{\gamma_E}$ where γ_E is the Euler-Mascheroni constant, and

$$\begin{aligned}
h_i^{(0)}(\lambda) =& \frac{1}{2\pi b_0 \lambda}\Big(2\lambda + (1-2\lambda)\ln(1-2\lambda)\Big) \\
h_i^{(1)}(\lambda) =& \frac{A_i^{(1)} b_1}{2\pi b_0^3}\left[\frac{1}{2}\ln^2(1-2\lambda) + \frac{2\lambda + \ln(1-2\lambda)}{1-2\lambda}\right] + \frac{B_i^{(1)}}{\pi b_0}\ln(1-2\lambda) \\
&+ \frac{1}{2\pi b_0}\left[A_i^{(1)}\ln\left(\frac{Q^2}{\mu^2}\right) - \frac{A_i^{(2)}}{\pi b_0}\right]\left[\frac{2\lambda}{1-2\lambda} + \ln(1-2\lambda)\right]
\end{aligned}$$

The final state exponent is given by

$$F_i(N,Q) = \frac{1}{\alpha_s(\mu)} f_i^{(0)}(\lambda) + f_i^{(1)}(\lambda, q, \mu) \tag{1.39}$$

where the f functions are related to the h functions in the following manner:

$$\begin{aligned}
f_i^{(0)}(\lambda) =& 2h^{(0)}(\lambda/2, \lambda/2) - h^{(0)}(\lambda, \lambda) \\
f_i^{(1)}(\lambda, Q, \mu) =& h^{(1)}(\lambda/2, \lambda/2, Q, \mu, Q) - h^{(1)}(\lambda, \lambda, Q, \mu, Q) \\
&+ \frac{A^{(1)}\ln 2}{\pi b_0}(\ln(1-2\lambda) - \ln(1-\lambda)) - \frac{B^{(1)}}{\pi b_0}\ln(1-\lambda)
\end{aligned} \tag{1.40}$$

The functions $C_{ab\to\gamma}$ in eqn. (1.33) are independent of N and constitute the matching terms between the resummed and finite order approach. They are computable as perturbative expansions[4] in α_s, i.e.

$$\begin{aligned}
&C_{ab\to\gamma}(\alpha_s(\mu^2), Q^2/\mu^2; Q^2/\mu_F) = \\
&1 + \frac{\alpha_s(\mu^2)}{\pi} C^{(1)}_{ab\to\gamma}(\alpha_s(Q^2/\mu^2; Q^2/\mu_F) + \mathcal{O}(\alpha_s^2)
\end{aligned} \tag{1.41}$$

The cross section in eqn. (1.33) can be evaluated numerically as written by implementing the analytically derived Mellin transforms, followed by an integration in the (complex) N-space [15].

1.6 Examples

The effect of adding orders of logarithms in the large N limit is best illustrated with an example involving the Drell-Yan process, which is defined at lowest order by the partonic process

$$q(p_1) + \bar{q}(p_2) \to \gamma^*(Q^2) \tag{1.42}$$

[4] They are currently only known to 1st order.

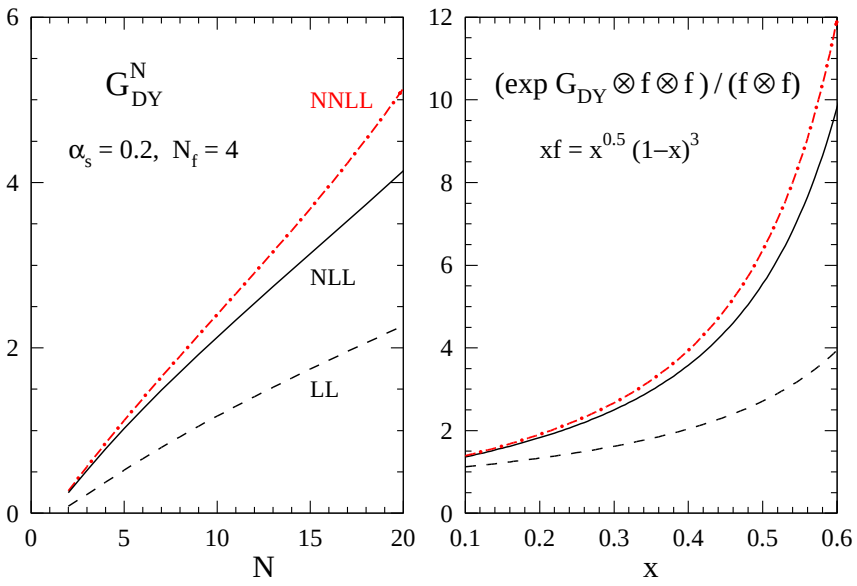

Figure 1.2: The left pane shows the LL, NLL and $NNLL$ exponents for the Drell-Yan process. The right pane shows the exponentiated exponents convoluted with parton distributions [16].

Its threshold-resummed expression can schematically be written as [16]

$$\sigma(N, Q^2) = f_q(N) f_{\bar{q}}(N) \times C(Q^2) \exp(G^N_{DY}(Q^2)) \tag{1.43}$$

where $G^N_{DY} = Lg_1(\lambda) + g_2(\lambda) + \alpha_s g_3(\lambda) + \ldots$, the successive terms increasing logarithmic accuracy. In fig. 1.2 we see the exponent as function of N when LL, NLL and NNLL contributions are included, respectively. The step from LL to NLL is considerable, while the progression from NLL to NNLL is more moderate. When combining the result with (toy) PDF's in the rightmost figure in fig. 1.2 ones sees that also the increases in the cross section become successively smaller as more subleading logarithms are taken into account. These studies illustrate the viability of threshold resummation in providing reliable estimates of cross sections.

1.7 Joint Resummation

Besides large logarithms from emission near an energy threshold, as discussed in section 1.5, other large logarithms occur when considering hadroproduction of, say, a vector boson with small transverse momentum Q_T. The leading logarithms in

momentum space then are

$$\alpha_s^n \frac{\ln^{2n-1} Q_T}{Q_T} \tag{1.44}$$

which again arise from soft and collinear radiation. In the context of the factorization theorem non-zero Q_T is a consequence of recoil against parton emission, the resummation of logarithms in eqn. (1.44) is known as recoil resummation. In analogy to the Mellin transform in threshold resummation here a Fourier transform with respect to Q_T to impact parameter b is used. The reason for this is the following. In general the recoil part of the hadronic cross section will be of the form

$$d\sigma_{\mathrm{H}} \sim \delta^2(Q_T - \sum_i k_{i,T}) \prod_i F_i(k_i) \tag{1.45}$$

which just states that Q_T is the aggregate result of recoil against an arbitrary number of parton emissions. The factors F_i are related to various parts of the collision process, see e.g. [17] and references therein. This can be simplified using the identity

$$\delta^2(Q_T - \sum_i k_{i,T}) = \frac{1}{(2\pi)^2} \int d^2b \exp\big(- ib \cdot (Q_T - \sum_i k_{i,T})\big) \tag{1.46}$$

Inserting this into eqn. (1.45) we get:

$$\begin{aligned} d\sigma_{\mathrm{H}} &\sim \prod_i dk_{i,T} \delta^2(Q_T - \sum_i k_{i,T}) \prod_i F_i(k_i) \\ &\sim \int d^2b \exp\big(- ib \cdot Q_T) \prod_i \tilde{F}_i(b) \end{aligned} \tag{1.47}$$

Thus all the functions $\tilde{F}_i$ depend on the *same* parameter b, making transverse momentum conservation easy to implement.

Joint resummation [17, 18] is the simultaneous resummation of both threshold ($\ln N$) and recoil logarithms ($\ln b$). It is possible because both types of logarithmic effects arises from the same soft and collinear regions of phase space. As a result, the overall form of the joint-resummed partonic cross section is similar to that in threshold resummation.

Let us consider here again the production of a prompt photon with transverse momentum p_T. The joint resummation formalism here effectively incorporates the notion that, when radiating off soft gluons, the process as a whole can recoil with momentum Q_T, leaving only $p'_T = p_T - Q_T/2$ to be produced in the actual hard scattering. Accordingly, the partonic scaling variable is modified to

$$\tilde{x}_T^2 \equiv \frac{4|\mathbf{p}_T - Q_T/2|^2}{\tilde{s}} \equiv \frac{4|\mathbf{p}'_T|^2}{\tilde{s}} \tag{1.48}$$

As stated, the exponent of the jointly resummed cross section is now, in addition to N, also dependent on b. This dependence comes through a modification of the integration limits of the integrals in eqn. (1.35). This modification involves the lower limit of integration in the first term eqn. (1.35) with a function of the two conjugate variables [19, 20]

$$\chi(N,b) = \bar{b} + \frac{\bar{N}}{1+\frac{\eta\bar{b}}{N}} \tag{1.49}$$

where $\bar{b} = bQe^{\gamma_E}/2$. The joint-resummed hadronic cross section becomes

$$\begin{aligned}\frac{p_T^3 d\sigma^{(\mathrm{resum})}_{AB\to\gamma+X}}{dp_T} &= \sum_{ab}\frac{p_T^4}{8\pi S^2}\int_{\mathcal{C}}\frac{dN}{2\pi i}\, f_{a/A}(N,\mu_F) f_{b/B}(N,\mu_F) \\ &\quad\times\int_0^1 d\tilde{x}_T^2\left(\tilde{x}_T^2\right)^N \frac{|M_{ij}(\tilde{x}_T^2)|^2}{\sqrt{1-\tilde{x}_T^2}}\; C^{(ab)}(\alpha_s(\mu),\tilde{x}_T^2) \\ &\quad\times\int\frac{d^2Q_T}{(2\pi)^2}\left(\frac{S}{4{p'_T}^2}\right)^{N+1} \\ &\quad\times\int d^2b\, \mathrm{e}^{ib\cdot Q_T}\,\exp\left[E_{ab\to\gamma c}(N,b)\right]\,.\end{aligned} \tag{1.50}$$

and now bears an additional b-dependence. The exponent can again be split as in eqn. (1.34). This expression will be discussed in more detail in the next chapter. Let us remark here that the initial state exponent for parton a reads

$$\begin{aligned}E_a(N,Q,\mu_F) = &-\int_{Q^2/\chi^2(N,b)}^{Q^2}\frac{dk_T^2}{k_T^2}\left\{A_a(\alpha_s(k_T))\ln\left(\frac{Q}{k_T}\right)+B_a(\alpha_s(k_T))\right\} \\ &+\int_{\mu_F^2}^{Q^2/\bar{N}}\frac{dk_T^2}{k_T^2}\big\{-\ln\bar{N}A_a(\alpha_s(k_T))-B_a(\alpha_s(k_T))\big\}.\end{aligned} \tag{1.51}$$

Further elaborations upon this result can be found in the next chapter.

1.8 Prompt Photon Production: Motivation And Description

As already mentioned earlier, a prompt photon is a photon produced directly by parton-parton collisions, as opposed to bremsstrahlung from final state charge particles e.g. This is a quite interesting class of processes to study. The photon thus produced can be seen as a messenger from the heart of the sub-nuclear interactions

when two nucleons collide. In this way studying prompt photons can tell us something about the parton distributions in protons and neutrons. Also in this process it is interesting to examine the effects of soft gluons. From a theoretical viewpoint, prompt photon production provides the simplest theoretical laboratory for $2 \to 2$ processes, just as Drell-Yan and deep-inelastic scattering are for $2 \to 1$ processes. Prompt photon processes also seem to be fairly clean tests of QCD since the final state is less prone to hadronization. Parton-level processes in which a prompt photon is produced are quark gluon Compton process, quark anti-quark annihilation and fragmentation processes, shown in fig. 1.3. The Compton process dominates

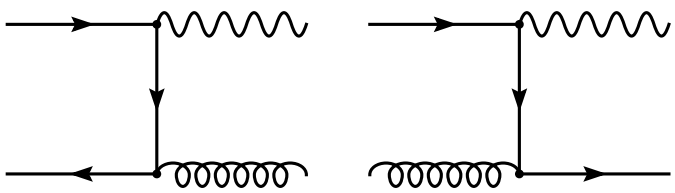

Figure 1.3: Two channels for lowest order prompt photon production: quark anti-quark annihilation, and the Compton process.

in pp-collision (for large x_T), because in this region the anti-quark distributions are rather small. Annihilation, on the other hand, can be significant in $p\bar{p}$-collisions due to the symmetry of particles and anti-particles in the proton and anti-proton, respectively. One of the perhaps most interesting benefits of prompt photon studies is the determination of the gluon content of protons. In particular the study of the qg-channel of prompt photon production combined with the knowledge of the quark distribution functions, allows in principle for measurements of the gluon content. In contrast to deep-inelastic scattering e.g., in prompt photon production the gluon distribution enters in lowest order[5]. Prompt photon data are sensitive to gluon distributions, and could particularly at larger x values help draw a more complete picture of gluon distributions. There are however difficulties [21] connected with the study of prompt photons. This is mainly due to the fact that it is very cumbrous to separate the photons coming from the hard interaction itself from photons which have their origin in decays of π^0, η etc. An often used experimental criterion is the application of an isolation cone, which demands only limited hadronic activity near a photon in the event. This criterion considerably limits the contribution coming from photons having origin in the fragmentation

[5]In deep-inelastic scattering the gluon distribution is only sensitive to the region of rather small x-values, where it is comparable to the quark distributions. The gluon distribution enters only in the next-to-leading order and contributes to the slope of the Q^2-dependence at leading order.

component compared to the direct (prompt) photons. This isolation cone however also introduces difficulties on the theoretical side [22, 23, 24].

As it turns out, NLO QCD is unable [25, 21] to fully account for fixed target and collider prompt photon data. For the former it seems that for small-x_T values soft gluons may play an important role [18]. In the next chapter we will examine some aspects of soft-collinear effects in prompt photon production.

References

[1] John C. Collins, Davison E. Soper, and George Sterman. Factorization of hard processes in qcd. in *Perturbative Quantum Chromodynamics*, A.H. Mueller ed., World Scientific, Singapore, 1989.

[2] Geoffrey T. Bodwin. Factorization of the drell-yan cross-section in perturbation theory. *Phys. Rev.*, D31:2616, 1985.

[3] D. J. Gross and Frank Wilczek. Ultraviolet behavior of non-abelian gauge theories. *Phys. Rev. Lett.*, 30:1343–1346, 1973.

[4] H. David Politzer. Asymptotic freedom: An approach to strong interactions. *Phys. Rept.*, 14:129–180, 1974.

[5] G. Altarelli and G. Parisi. Asymptotic freedom in parton language. *Nucl. Phys.*, B126:298, 1977.

[6] A. Vogt. Efficient evolution of unpolarized and polarized parton distributions with qcd-pegasus. *Comput. Phys. Commun.*, 170:65–92, 2005.

[7] Michael E. Peskin and D. V. Schroeder. An introduction to quantum field theory. Reading, USA: Addison-Wesley (1995) 842 p.

[8] J. G. M. Gatheral. Exponentiation of eikonal cross-sections in nonabelian gauge theories. *Phys. Lett.*, B133:90, 1983.

[9] J. Frenkel and J. C. Taylor. Nonabelian eikonal exponentiation. *Nucl. Phys.*, B246:231, 1984.

[10] G. Sterman. Infrared divergences in perturbative qcd. In *Tallahassee 1981, Proceedings, Perturbative Quantum Chromodynamics*, 22-40.

[11] Eric Laenen, Gianluca Oderda, and George Sterman. Resummation of threshold corrections for single particle inclusive cross-sections. *Phys. Lett.*, B438:173–183, 1998.

[12] Stefano Catani, Michelangelo L. Mangano, and Paolo Nason. Sudakov resummation for prompt photon production in hadron collisions. *JHEP*, 9807:024, 1998.

[13] Stefano Catani, Michelangelo L. Mangano, Paolo Nason, Carlo Oleari, and Werner Vogelsang. Sudakov resummation effects in prompt photon hadroproduction. *JHEP*, 9903:025, 1999.

[14] Jiro Kodaira and Luca Trentadue. Summing soft emission in qcd. *Phys. Lett.*, 112B:66, 1982.

[15] D. Graudenz, M. Hampel, A. Vogt, and Christoph Berger. The mellin transform technique for the extraction of the gluon density. *Z. Phys.*, C70:77–82, 1996.

[16] A. Vogt. Next-to-next-to-leading logarithmic threshold resummation for deep-inelastic scattering and the drell-yan process. *Phys. Lett.*, B497:228–234, 2001.

[17] Eric Laenen, George Sterman, and Werner Vogelsang. Recoil and threshold corrections in short-distance cross sections. *Phys. Rev.*, D63:114018, 2001.

[18] Eric Laenen, George Sterman, and Werner Vogelsang. Higher-order qcd corrections in prompt photon production. *Phys. Rev. Lett.*, 84:4296, 2000.

[19] Anna Kulesza, George Sterman, and Werner Vogelsang. Joint resummation in electroweak boson production. *Phys. Rev.*, D66:014011, 2002.

[20] Anna Kulesza, George Sterman, and Werner Vogelsang. Joint resummation for higgs production. *Phys. Rev.*, D69:014012, 2004.

[21] Patrick Aurenche, Michel Fontannaz, Jean-Philippe Guillet, Eric Pilon, and Monique Werlen. A new critical study of photon production in hadronic collisions. *Phys. Rev.*, D73:094007, 2006.

[22] Edmond L. Berger, Xiao-feng Guo, and Jian-wei Qiu. Breakdown of conventional factorization for isolated photon cross sections. *Phys. Rev. Lett.*, 76:2234–2237, 1996.

[23] P. Aurenche, M. Fontannaz, J. P. Guillet, A. Kotikov, and E. Pilon. Is factorization for isolated photon cross sections broken? *Phys. Rev.*, D55:1124–1126, 1997.

[24] S. Catani, M. Fontannaz, and E. Pilon. Factorization and soft-gluon divergences in isolated-photon cross sections. *Phys. Rev.*, D58:094025, 1998.

[25] P. Aurenche et al. A critical phenomenological study of inclusive photon production in hadronic collisions. *Eur. Phys. J.*, C9:107–119, 1999.

Chapter 2

Soft-collinear effects in prompt photon production

The perturbative QCD description of many observables measured at colliders is plagued by large corrections arising from soft and collinear parton emission, even for fairly generic kinematical conditions. For example, near threshold, large logarithmic corrections remain [1, 2] after cancellation of singular virtual and real gluon contributions, their large size being a result of the nearby threshold restricting the real gluons to be soft. In terms of a (Mellin) variable N, in terms of which threshold is approached by $N \to \infty$, such large threshold corrections take the form ($L = \ln N$),

$$\alpha_s^i \sum_j^{2i} a_{ij} L^j \,, \tag{2.1}$$

where the a_{ij} depend in general on the process. Another example [3, 4, 5, 6, 7, 8] is when an identified part F_P of a final state has acquired small transverse momentum by soft recoil (Q_T) against the remaining, unmeasured part of the final state. Then the perturbative expression for the differential cross section with respect to p_T of F_P takes again the form of eqn. (2.1), but with different coefficients a_{ij} and with $L = \ln b$, b being the impact parameter Fourier conjugate to Q_T.

Such large logarithmic corrections can be brought under control by all-order resummation, and there exists a large literature demonstrating the viability, where applicable, of threshold, recoil as well as their joint resummation, for a wide variety of observables. It is interesting to try to extend all-order control to classes of large terms beyond the logarithmic corrections. One such new set consists of numerically large constants ("π^2 terms") originating from the same infrared-sensitive regions of those Feynman diagrams that also produce the logarithms [9, 10, 11].

Another important class of potentially large terms, of soft-collinear origin, can

be represented as

$$\alpha_s^i \sum_j^{2i-1} d_{ij} \frac{\ln^j N}{N} \,. \tag{2.2}$$

Their phenomenological importance was first demonstrated in Ref. [12] in which the leading terms $j = 2i-1$ were also summed to all orders for Higgs production and Drell-Yan. The assessment of these terms was made more meaningful in the context of a complete next-to-next-leading order (NNLO) [13, 14, 15, 16, 17, 18, 19] calculation, and a consistent next-to-next-leading logarithmic (NNLL) threshold-resummed result [20]. It is not yet clear how to sum next-to-leading terms in (2.2).

In this chapter we examine the impact of the leading terms in (2.2) for a single particle inclusive observable, the p_T spectrum of prompt photons produced in hadronic collisions. We do this in the context of both a threshold [21, 22, 23, 24, 25] and joint [26, 27, 28, 29] resummed calculation for this spectrum.

The chapter is organized as follows. In section 2 we review briefly the threshold and joint resummed prompt photon p_T distribution. In section 3 we describe and motivate our extension to include the leading $\alpha_s^k \frac{\ln^{2k-1} N}{N}$ terms. In section 4 we assess the numerical impact of these corrections, and we conclude in section 5.

2.1 Threshold and joint resummation for prompt photon production

We consider the inclusive p_T distribution of prompt photons produced in hadron-hadron collisions at centre of mass (cm) energy $\sqrt{S}$

$$h_A(p_A) + h_B(p_B) \to \gamma(p_c) + X \,, \tag{2.3}$$

where $h_{A,B}$ refer to the two incoming hadrons and X to the unobserved part of the final state. The lowest order QCD processes producing the prompt photon at partonic cm energy $\sqrt{s}$ are

$$\begin{aligned} q(p_a) + \bar{q}(p_b) &\to \gamma(p_c) + g(p_d) \,, \\ g(p_a) + q(p_b) &\to \gamma(p_c) + q(p_d) \,. \end{aligned} \tag{2.4}$$

The distance to threshold is customarily measured by the variable $1 - x_T^2$, where $x_T^2 = 4p_T^2/S$. At the parton level this distance is given by $1 - \hat{x}_T^2 = 1 - 4p_T^2/s$. Below we review the result for the joint resummed prompt photon p_T distribution. At the end of this section we recall how the threshold resummed result may be derived from it.

The joint resummation formalism for prompt photon production [26, 27] implements the notion that, in the presence of soft QCD radiation with summed transverse momentum $\mathbf{Q}_T$ of soft recoiling partons, the actual transverse momentum produced by the hard collision is not $\mathbf{p_T}$ but rather $\mathbf{p'_T} = \mathbf{p_T} - \mathbf{Q_T/2}$. Stated more precisely: in the context of a refactorization analysis [27] one can identify a short-distance process at cm energy Q that produces a prompt photon with momentum $\mathbf{p'_T}$ in a recoiling frame. One defines accordingly $\tilde{x}_T^2 = 4{p'}_T^2/Q^2$. The extreme situation $Q_T = 2p_T$ in which all transverse momentum is produced through soft recoil leads to a singularity in the short-distance process, which we avoid by imposing an upper limit $\bar{\mu}$ on Q_T [26]. A recently proposed extension [28] of joint resummation avoids this singularity.

The joint resummed p_T distribution of prompt photons in hadronic collisions is written as

$$\begin{aligned}\frac{p_T^3 d\sigma^{(\mathrm{resum})}_{AB\to\gamma+X}}{dp_T} &= \sum_{ij} \frac{p_T^4}{8\pi S^2} \int_{\mathcal{C}} \frac{dN}{2\pi i}\, f_{i/A}(N,\mu_F) f_{j/B}(N,\mu_F) \\ &\times \int_0^1 d\tilde{x}_T^2 \left(\tilde{x}_T^2\right)^N \frac{|M_{ij}(\tilde{x}_T^2)|^2}{\sqrt{1-\tilde{x}_T^2}}\; C^{(ij\to\gamma k)}(\alpha_s(\mu),\tilde{x}_T^2) \\ &\times \int \frac{d^2\mathbf{Q}_T}{(2\pi)^2}\, \Theta\left(\bar{\mu}-Q_T\right) \left(\frac{S}{4{\mathbf{p}'_T}^2}\right)^{N+1} \\ &\times \int d^2\mathbf{b}\, \mathrm{e}^{i\mathbf{b}\cdot\mathbf{Q}_T}\, \exp\left[E_{ij\to\gamma k}\left(N,b,\frac{4p_T^2}{\tilde{x}_T^2},\mu_F\right)\right] \quad (2.5)\end{aligned}$$

Let us explain each of the terms on the right hand side of eqn. (2.5). The top line displays the moments of standard parton distribution functions, as well as the sum over initial state parton flavours. The next line contains the Mellin transform over the partonic scaling variable $\tilde{x}_T^2$ in the recoiling frame, the Born amplitudes, and the N- and b-independent hard virtual corrections summarized in $C^{(ij\to\gamma k)}$. The second to last line contains the integral over the recoil momentum of the soft partons, as well as a kinematic factor linking recoil and threshold effects. The last line contains the Sudakov exponentials from initial and final state partons, as well as soft wide-angle radiation in combined Mellin-impact parameter space.

As indicated in the last line of eqn. (2.5), large threshold and recoil logarithms, expressed through $\ln N$ and $\ln b$, can be resummed into an exponential form. The perturbative exponential moment dependence at next-to-leading logarithmic (NLL) accuracy is given by

$$\begin{aligned}&E^{\mathrm{PT}}_{ij\to\gamma k}(N,b,Q,\mu,\mu_F) = \\ &\quad E^{\mathrm{PT}}_i(N,b,Q,\mu,\mu_F) + E^{\mathrm{PT}}_j(N,b,Q,\mu,\mu_F) + F_k(N,Q,\mu) + G_{ijk}(N,\mu)\,. \quad (2.6)\end{aligned}$$

Let us discuss each of these terms in turn. The initial state perturbative exponent reads, in integral form

$$\begin{aligned} E_i^{\rm PT}(N,b,Q,\mu,\mu_F) = &- \int_{Q^2/\chi^2}^{Q^2} \frac{dk_T^2}{k_T^2} \left\{ A_i\left(\alpha_s(k_T)\right) \, \ln\left(\frac{Q}{\bar{N}k_T}\right)\right\} \\ &- 2\ln\bar{N} \int_{\mu_F^2}^{Q^2} \frac{dk_T^2}{k_T^2} A_i\left(\alpha_s(k_T)\right) \end{aligned} \tag{2.7}$$

where μ, μ_F are the renormalization and factorization scale, respectively. The function $\chi(N,b)$ defines the N- and b-dependent scale of soft gluons to be included in the resummation, and is chosen as [30]

$$\chi(N,b) = \bar{b} + \frac{\bar{N}}{1+\frac{\eta\bar{b}}{\bar{N}}} \,, \tag{2.8}$$

where η is a suitably chosen constant and

$$\bar{N} = Ne^{\gamma_E}, \quad \bar{b} = bQe^{\gamma_E}/2 \,, \tag{2.9}$$

with γ_E the Euler constant. An older form used in [26]

$$\chi(N,b) = \bar{b} + \bar{N} \tag{2.10}$$

generates spurious subleading logarithms in Q_T [30]. We postpone elaborating on the integral in eqn. (2.7) to the next section. The final state jet exponent reads to NLL accuracy

$$F_k(N,Q,\mu) \equiv \frac{1}{\alpha_s(\mu)} f_k^{(0)}(\lambda) + f_k^{(1)}(\lambda,Q,\mu) \,, \tag{2.11}$$

where

$$\lambda = b_0 \alpha_s(\mu^2) \ln\bar{N} \,. \tag{2.12}$$

The exponent associated with wide angle soft radiation is

$$G_{abc}(N) \equiv g_{abc}^{(1)}(\lambda) \,. \tag{2.13}$$

The functions $f_k^{(0,1)}$ and $g_{ijk}^{(1)}(\lambda)$ as well as the functions $C^{(ij\to\gamma k)}$ [22, 23] are listed in Appendix A.

A nonperturbative term must be added to the perturbative exponent in eqn. (2.6) in order to regularize the limit in which Q_T is very small. As in Refs. [26, 27] we take

$$E_{ij}^{\rm NP} = -\tfrac{1}{2} g_{\rm NP} b^2 \qquad ij = q\bar{q},\, qg \,. \tag{2.14}$$

The threshold-resummed result can now be derived by simply neglecting $\mathbf{Q_T}$ in the factor $(S/[4|\mathbf{p}_T - \mathbf{Q}_T/2|^2])^{N+1}$ in eqn. (2.5). Then the $\mathbf{Q_T}$ integral sets $\mathbf{b}$ to zero everywhere, yielding the threshold-resummed result.

2.2 Including leading $\ln N/N$ terms

The leading terms in eqn. (2.2) originate from both initial and final state radiation, and to resum them we will use two different methods upon which we elaborate in this section. There are moreover two classes of functions in momentum space at order α_s^j that generate the leading $\ln^{2j-1} N/N$ terms upon Mellin transformation. In terms of the variable z, $0 < z < 1$ which in the present case can represent either $\hat{x}_T^2$ or $\tilde{x}_T^2$, one of the two classes is formed by the singular plus distributions $[\ln^{2j-1}(1-z)/(1-z)]_+$, the other by the singular but integrable $\ln^{2j-1}(1-z)$. The $\ln N/N$ contributions from the former can be computed using the methods of [31] and can be found e.g. in Ref. [12]. The $\ln N/N$ contributions from the latter can be generated at any order in perturbation theory by a simple replacement in the resummed expression (see below in Eqs. (2.25)), expanding the resulting expression to the desired order, and keeping the leading term in eqn. (2.2). Roughly speaking, the replacement is equivalent to exchanging at order j one soft-collinear gluon (corresponding to one factor $\alpha_s \ln^2 N$) for a hard-collinear one (corresponding to a factor $\alpha_s \ln N/N$)

$$\alpha_s^k \ln^{2k} N \to \alpha_s^k \frac{\ln^{2k-1} N}{N} \,. \tag{2.15}$$

This replacement is in fact easily included in the existing threshold resummation formulae. A preliminary study for prompt photon production was carried out in Ref. [32]. We employ this replacement method in fact for the final state related $\alpha_s^k \ln^{2k-1} N/N$ terms. It was pointed out in Refs. [30, 33] that the initial state related $\alpha_s^k \ln^{2k-1} N/N$ terms could be generated in the context of joint resummation by extending evolution of parton densities to a soft scale. We will use this method as well, for the first time for a one-particle inclusive observable. We now discuss the initial and final state $\ln N/N$ contributions in turn.

2.2.1 Initial state

Our procedure for the initial state follows Refs. [30, 33], where the joint resummation for electroweak or Higgs boson production at mass Q and transverse momentum Q_T was given. We recall the key points here. The integral form of the initial state NLL exponent (2.7) can be written as

$$\begin{aligned} E_i^{\rm PT}(N, b, Q, \mu, \mu_F) = &- \int_{Q^2/\chi^2}^{Q^2} \frac{dk_T^2}{k_T^2} \left\{ A_i\left(\alpha_s(k_T)\right) \ln\left(\frac{Q}{k_T}\right) + B_i\left(\alpha_s(k_T)\right) \right\} \\ &+ \int_{\mu_F^2}^{Q^2/\chi^2} \frac{dk_T^2}{k_T^2} \left\{ -\ln \bar{N} A_i\left(\alpha_s(k_T)\right) - B_i\left(\alpha_s(k_T)\right) \right\} . \end{aligned} \tag{2.16}$$

The first term in this expression leads to

$$E_i^{\rm PT}(N,b,Q,\mu) = \frac{1}{\alpha_s(\mu)} h_i^{(0)}(\beta) + h_i^{(1)}(\beta,Q,\mu)\ , \tag{2.17}$$

where

$$\beta = b_0\,\alpha_s(\mu)\ln(\chi)\ . \tag{2.18}$$

We recall that the χ depends on N and b through eqn. (2.8). The functions $h_i^{(0,1)}$ are listed in Appendix A .

The second term represents flavour-conserving evolution to NLL accuracy (the integrand consists of the $\ln N$ and constant terms for the anomalous dimension matrix $\gamma_{i/j}(N)$ for $j=i$) from the hard scale μ_F to the soft scale Q/χ. One now performs the replacement [30, 33]

$$-A_i(\alpha_s)\ln\left(\bar{N}\right) - B_i(\alpha_s) \ \longrightarrow\ \gamma_{i/i}(N)(\alpha_s)\ , \tag{2.19}$$

that includes the leading, flavour-diagonal $\ln N/N$ effects generated by the k_T integral (the $1/N$ part of $\gamma_{i/i}$ combines with the $\ln N$ terms). In fact, one may go further and include the off-diagonal contributions via the replacement

$$\delta_{ig}\,\exp\left[\frac{-A_g^{(1)}\ln\bar{N} - B_g^{(1)}}{2\pi b_0}\,s(\beta)\right]\ f_{g/H}(N,\mu_F)\ \longrightarrow\ \mathcal{E}_{ik}\left(N,Q/\chi,\mu_F\right)\ f_{k/H}(N,\mu_F)\,. \tag{2.20}$$

where $s(\beta) = \ln(1-2\beta)$ plus NLL corrections. As a result, we can replace in eqn. (2.5) the combination

$$f_{i/A}(\mu_F,N) f_{j/B}(\mu_F,N)\exp\left[E_i^{\rm PT}(N,b,Q,\mu,\mu_F) + E_j^{\rm PT}(N,b,Q,\mu,\mu_F)\right] \tag{2.21}$$

by

$$\mathcal{C}_{i/A}(Q,b,N)\,\mathcal{C}_{j/B}(Q,b,N)\ \exp\left[E_i^{\rm PT}(N,b,\mu,Q) + E_j^{\rm PT}(N,b,\mu,Q)\right] \tag{2.22}$$

where

$$\mathcal{C}_{i/H}(Q,b,N) = \sum_k \mathcal{E}_{ik}\left(N,Q/\chi,\mu_F\right)\ f_{k/H}(N,\mu_F)\ . \tag{2.23}$$

The matrix $\mathcal{E}$ implements evolution from scale μ_F to scale Q/χ, and is normalized to be the unit matrix if these two scales are equal. Note that the dependence on μ_F cancels among the factors in eqn. (2.23).

2.2.2 Final state

Leading $\ln N/N$ effects arising from final state radiation can be derived from the jet functions [1, 34] that enter threshold or joint resummed expressions for observables having final state partons at lowest order. The integral form of the final state exponent F_k in eqn. (2.6) reads

$$\int_0^1 dz \frac{z^{N-1}-1}{1-z} \left\{ \int_{(1-z)^2Q^2}^{(1-z)Q^2} \frac{dq^2}{q^2} A_k(\alpha_s(q^2)) + B_k(\alpha_s((1-z)Q^2)) \right\} . \tag{2.24}$$

To include leading $\ln N/N$ dependence in $F_k(N,Q,\mu)$ we make the replacement [12, 20, 32]

$$\frac{z^{N-1}-1}{1-z} A_i^{(1)} \to \left[\frac{z^{N-1}-1}{1-z} - p_i z^{N-1} \right] A_q^{(1)} + \mathcal{O}(\frac{1}{N^2}) , \tag{2.25}$$

where $p_q = 1, p_g = 2$. The extra terms can be cast in a more convenient form. Using

$$z^{N-1} = \frac{z^{N-1} - 1 - (z^N - 1)}{1-z} \tag{2.26}$$

and the replacement (accurate to NLL)

$$z^{N-1} - 1 \to -\theta \left(1 - z - \frac{1}{\bar{N}} \right) \tag{2.27}$$

one finds

$$F_k(N,Q,\mu) = \frac{1}{\alpha_s(\mu)} f_k^{(0)}(\lambda) + f_k^{(1)}(\lambda,Q,\mu) + f_k'(\lambda,\alpha_s) + O(\alpha_s(\alpha_s \ln N)^n) , \tag{2.28}$$

where the extra terms $f\prime_k$ that include the leading $\ln N/N$ terms due to final state radiation read

$$f_q' = \frac{A_q^{(1)}}{2\pi b_0} \exp\left(-\frac{\lambda}{\alpha_s b_0} \right) \left[\ln(1-2\lambda) - \ln(1-\lambda) \right] , \tag{2.29}$$

$$f_g' = \frac{3A_g^{(1)}}{2\pi b_0} \exp\left(-\frac{\lambda}{\alpha_s b_0} \right) \left[\ln(1-2\lambda) - \ln(1-\lambda) \right] . \tag{2.30}$$

There is no leading $\ln N/N$ contribution arising from wide angle soft radiation.

As a result, we finally arrive at the following equation for the joint resummed prompt photon hadroproduction p_T spectrum in which leading soft-collinear effects

are included:

$$\frac{p_T^3 d\sigma_{AB\to\gamma}^{(\mathrm{resum})}}{dp_T} = \frac{p_T^4}{8\pi S^2}\sum_{ij}\int_{\mathcal{C}}\frac{dN}{2\pi i}\int d^2\mathbf{b}\,\mathrm{e}^{i\mathbf{b}\cdot\mathbf{Q}_T}\int\frac{d^2\mathbf{Q}_T}{(2\pi)^2}\,\theta\left(\bar{\mu}-|\mathbf{Q}_T|\right)$$
$$\times\int_0^1 d\tilde{x}_T^2\,\left(\tilde{x}_T^2\right)^N\frac{|M_{ij}(\tilde{x}_T^2)|^2}{\sqrt{1-\tilde{x}_T^2}}\,C^{(ij\to\gamma k)}(\alpha_s(\mu),\tilde{x}_T^2)\,\left(\frac{S}{4|\mathbf{p}_T-\mathbf{Q}_T/2|^2}\right)^{N+1}$$
$$\times\mathcal{C}_{i/A}(Q,b,N)\,\mathcal{C}_{j/B}(Q,b,N)\,\exp\left[E_i^{\mathrm{PT}}(N,b,\mu,Q)+E_j^{\mathrm{PT}}(N,b,\mu,Q)\right]$$
$$\times\exp\left[\frac{1}{\alpha_s(\mu)}f_k^{(0)}(\lambda)+f_k^{(1)}(\lambda,Q,\mu)+f_k'(\lambda,\alpha_s)+g_{ijk}^{(1)}(\lambda)\right]. \qquad (2.31)$$

As before, the corresponding threshold result may be obtained by neglecting $-\mathbf{Q}_T/2$ in the last factor on the second line.

2.3 Results

Here we study numerically the inclusion of the $\ln N/N$ terms for the case of prompt photon production for two kinematic conditions: those of $p\bar{p}$ collisions at the Tevatron at $\sqrt{S}=1.96$ TeV [35, 36], and those of the pN collisions in the E706 [37] fixed target experiment with $E_{\mathrm{beam}}=530$ GeV. Our main aim is to assess the effect of such terms in relevant kinematic conditions, rather than provide optimized and realistic theoretical calculations for comparison with data (see Ref. [38] for recent study). For instance, we do not include contributions from fragmentation processes, which have recently been addressed in Ref. [39] and shown to be significant. Our assessments mainly consist of comparing the same calculation with and without $\ln N/N$ terms.

Our default choices for various input parameters are as follows. We use the GRV parton density set [40], corresponding to $\alpha_s(M_Z)=0.114$, with the evolution code of Ref. [41], changing flavour number at $\mu=m_c$ (1.4 GeV) and m_b (4.5 GeV). We choose the factorization and renormalization scale equal to p_T, and the non-perturbative parameter g_{NP} in eqn. (2.14) equal to $1\,\mathrm{GeV}^2$. For the parameter χ we use the expression in eqn. (2.8), following [30], with $\eta=1/4$ [1]. For our joint-resummed results, we chose for Tevatron (E706) kinematics the cut-off $\bar{\mu}$ in eqn. (2.5) equal to 15 (5) GeV. Regarding logarithmic accuracy, and unless otherwise stated we refer to LL when using only $h_a^{(0)}$ in eqn. (2.17), $f_k^{(0)}$ in eqn. (2.28), and $\bar{C}^{(ij\to\gamma k)}=1$ for the processes in (2.4); we refer to NLL when also including $h_a^{(1)}$ and $f_k^{(1)}$ and the virtual corrections in (A.10). For the evolution from scale μ_F to Q/χ in eqn. (2.20) we use the full NLO anomalous dimension in all cases.

[1] Choosing $\eta=1$ does not substantially modify results, but choosing the form in eqn. (2.10), which generates spurious subleading recoil logs [30], does lead to significant changes at larger p_T.

Starting with Tevatron kinematics we compare in Figs. 2.1-2.3 results at LL and NLL accuracy, with and without the leading $\ln N/N$ contribution for joint resummation. For clarity we have here included the constant corrections in (A.10)

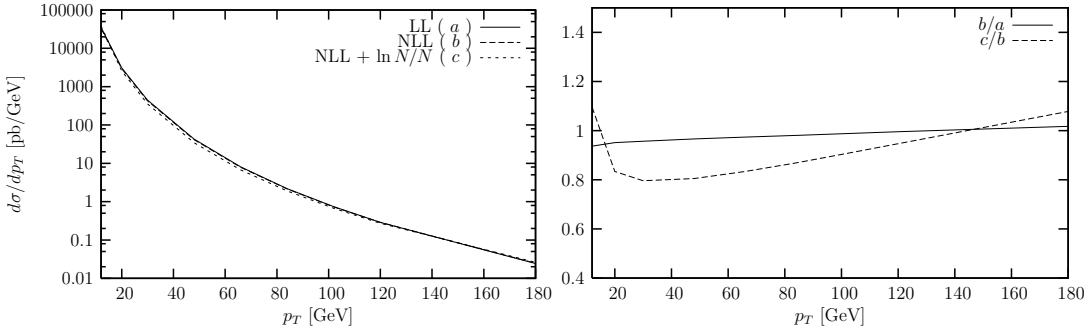

Figure 2.1: $\ln N/N$ contributions for Tevatron kinematics. Left pane: LL without $\ln N/N$ (a, solid), NLL without $\ln N/N$ (b, dashed), NLL with $\ln N/N$ (c, short-dashed). Right pane: ratio of NLL to LL (solid), ratio of NLL with $\ln N/N$ to NLL without (dashed).

also for the LL case. Fig. 2.1 shows that the effect of the leading $\ln N/N$ is appreciable when compared to the effect of passing from LL to NLL, the latter difference being almost negligible. Inclusion of $\ln N/N$ effects leads to noticeable suppression for most of the p_T range, and to enhancement at very small and very large p_T. To better understand the origin of these $\ln N/N$ suppressed contributions, we examine in Figs. 2.2 and 2.3 for each channel in (2.4) the contributions from the initial and final state. We plot these contributions for the LL cross sections

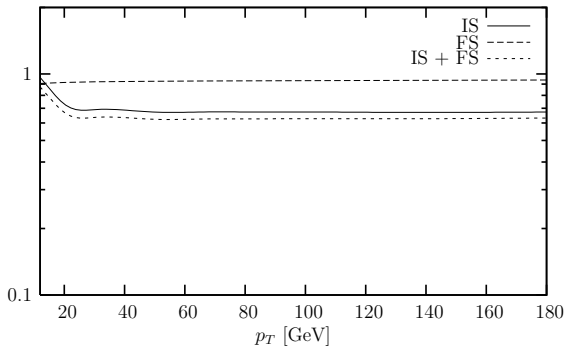

Figure 2.2: $\ln N/N$ effects for $q\bar{q}$ channel at LL, Tevatron kinematics. Ratio to LL without $\ln N/N$ of initial state (solid) and final state (dashed) effects, and both (short-dashed).

only to facilitate interpretation. To help understand the results, we can expand

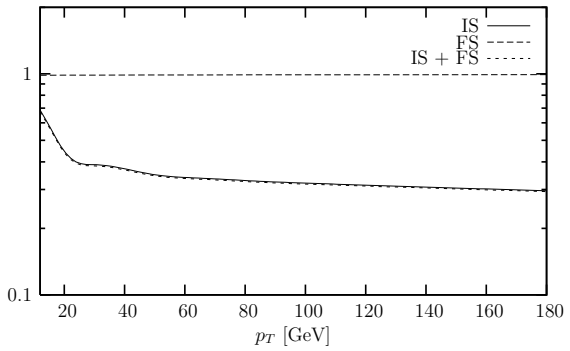

Figure 2.3: $\ln N/N$ effects for qg channel at LL, Tevatron kinematics. Labels as in Fig. 2.2.

the perturbative exponent in eqn. (2.6) to lowest order in α_s, keeping only the $\ln^2 N$ and $\ln N/N$ terms

$$\mathrm{q\bar{q}}: \quad : \frac{\alpha_s}{\pi} \ln^2 N \left(2A_q^{(1)} - \tfrac{1}{2}A_g^{(1)}\right) + \frac{\alpha_s}{\pi}\frac{\ln N}{N}\left(2A_q^{(1)} - \tfrac{3}{2}A_g^{(1)}\right) \tag{2.32}$$

$$\mathrm{qg}: \quad : \frac{\alpha_s}{\pi} \ln^2 N \left(A_q^{(1)} + A_g^{(1)} - \tfrac{1}{2}A_q^{(1)}\right) + \frac{\alpha_s}{\pi}\frac{\ln N}{N}\left(A_q^{(1)} + 3A_g^{(1)} - \tfrac{1}{2}A_q^{(1)}\right) \tag{2.33}$$

The expressions suggest that the initial state $\ln N/N$ terms enhance the cross section for the $q\bar{q}$ and in particular the qg channels, while the final state $\ln N/N$ terms suppress it, again by an amount that depends on the channel. The net result turns out to be suppression in the former channel and enhancement in the latter. These qualitative aspects are indeed borne out if we use the same method to compute initial state $\ln N/N$ effects as we did for the final state in section 2.2.2 [2]. In the present case however, the net $\ln N/N$ effect in both channels is suppression, indicating that the non-diagonal terms in the evolution matrix give a sizeable negative contribution. Note that for Tevatron kinematics, when combining channels, the qg channel dominates at low p_T, because the required momentum fractions are not too large. At large p_T, where parton momentum fractions are larger, the valence-quark dominated $q\bar{q}$ channel takes over.

Turning to E706 kinematics we perform the same studies as we did for the Tevatron. The results are shown in Figs. 2.4-2.6. We observe an overall enhancement due to the $\ln N/N$ effects, somewhat smaller than the change from LL to NLL. Both effects are more pronounced than for the Tevatron. This is due both to a larger value of α_s as well as being closer to threshold in this fixed target kinematical regime. Examining the effects per channel in Figs. 2.5 and 2.6, we

[2] The net result in the $q\bar{q}$ is actually still enhancement, because the contribution of the $f'_{q,g}$ functions in (2.29), (2.30) is very small.

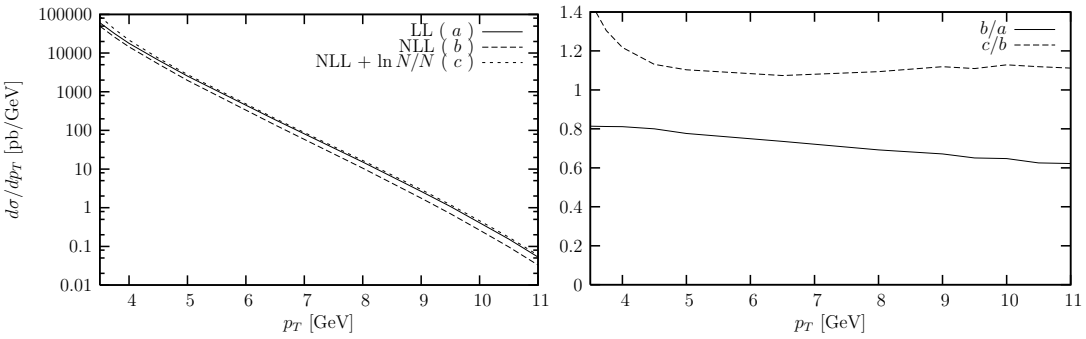

Figure 2.4: $\ln N/N$ contributions for E706 kinematics. Labels as in Fig. 2.1.

now see a noticeable enhancement from the initial state $\ln N/N$ effects in the $q\bar{q}$ channel, but still suppression in the qg channel. Clearly the non-diagonal terms in the evolution matrix play a significant role for the E706 case as well.

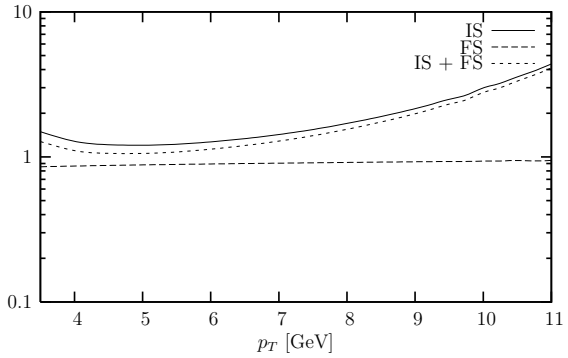

Figure 2.5: $\ln N/N$ effects for $q\bar{q}$ channel at LL, E706 kinematics. Labels as in Fig. 2.2.

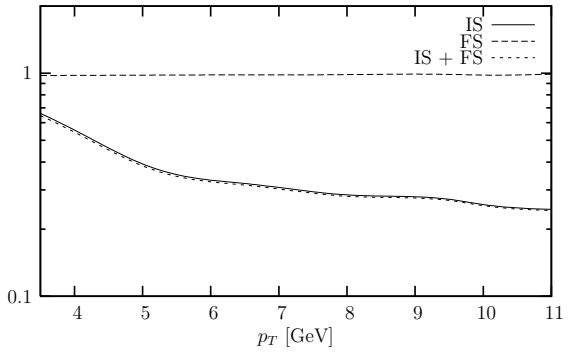

Figure 2.6: $\ln N/N$ effects for qg channel at LL, E706 kinematics. Labels as in Fig. 2.2.

Next, we examine the differences between threshold and joint resummation.

In Fig. 2.7 we compare resummed results directly by showing the ratios with respect to the joint-resummed p_T distribution without $\ln N/N$ terms. We see for Tevatron kinematics that the threshold resummed dominates the joint resummed at large p_T, while at low p_T the converse is true. For the E706 case the threshold resummed results are entirely below the joint-resummed ones. The threshold

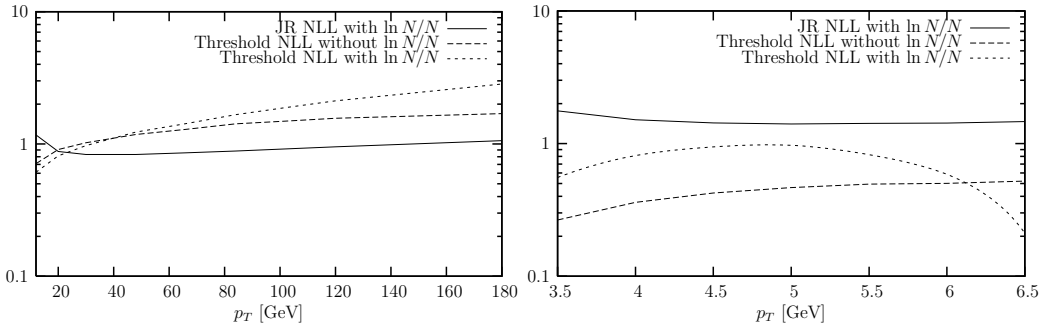

Figure 2.7: Comparison of joint resummation and threshold resummation effects, ratios to NLL without $\ln N/N$ for Tevatron (left pane) and E706 (right pane).

resummed curves are shown separately in Fig. 2.8, which is analogous to the rightmost panels in Figs. 2.1 and 2.4. For Tevatron kinematics the inclusion of $\ln N/N$

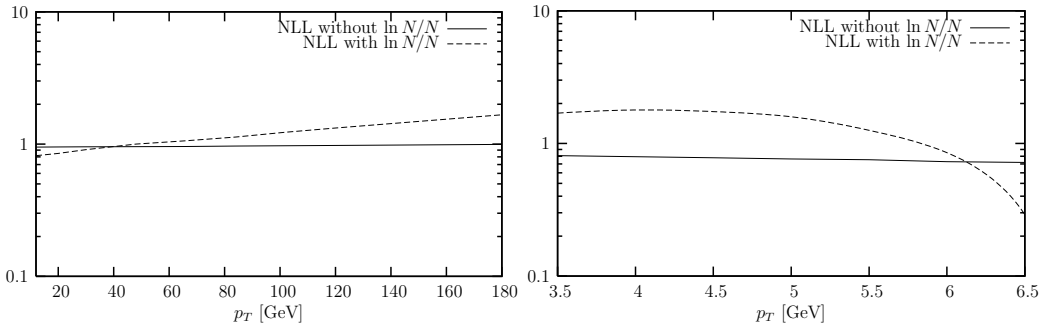

Figure 2.8: $\ln N/N$ effects in threshold resummation, for Tevatron (left pane) and E706 (right pane). Labels as in Fig. 2.1 right pane.

terms in threshold resummation leads, as for joint resummation, from suppression at small p_T to enhancement at larger p_T, but more noticeably. For E706 kinematics, different from the joint resummation case, the enhancement at small p_T turns to suppression just below $p_T = 6$ GeV. The cross section even becomes negative beyond 6.5 GeV, which is due to the fact that the nearness of the threshold drives the scale Q/χ in eqn. (2.20) effectively below the starting scale of the PDF evolution.

2.4 Conclusions

We have examined the effects of including terms of the form

$$\alpha_s^i \sum_j^{2i-1} d_{ij} \frac{\ln^j N}{N} \,. \tag{2.34}$$

in joint-resummed and threshold-resummed prompt photon p_T distributions at both collider and fixed target kinematics, at leading accuracy ($j = i$). The complete structure of subleading terms of the form (2.34) is still unknown. Note that we have not considered the fragmentation component of the prompt photon production cross section in our analysis [3].

To the extent that terms of the form (2.34) arise from initial state radiation effects, we used the method of Refs. [30, 33] to include them, now in a single-particle inclusive cross section. Those arising from final state emission we included by extending the jet function to leading $\ln N/N$ accuracy. Numerically we found the combined $\ln N/N$ terms to be comparable to NLL corrections, and dependent on kinematics either enhancing or suppressing. The final state $\ln N/N$ contributions were particularly small, while in the initial state the effects of non-leading $1/N$ effects are appreciable, depending again on channel and kinematics. The flavour non-diagonal terms in the evolution matrix were found to be numerically significant, and the main source of discrepancy with expectations based on simple approximations. We conclude that, because the effects, though small, are non-negligible, understanding the structure of $\ln N/N$ terms better is a worthwhile pursuit.

[3] To do so would require inclusion of more partonic subprocesses, each containing a sum over colour structures for the wide-angle soft radiation component, as well as photon fragmentation functions [39]. Presumably, soft-collinear effects for the fragmentation component of prompt photon production could be included in a way analogous to what we did in this chapter for the initial state: via adjustment of the resummed part, and evolution of the fragmentation functions.

References

[1] George Sterman. Summation of large corrections to short distance hadronic cross-sections. *Nucl. Phys.*, B281:310, 1987.

[2] S. Catani and L. Trentadue. Resummation of the qcd perturbative series for hard processes. *Nucl. Phys.*, B327:323, 1989.

[3] Yuri L. Dokshitzer, Dmitri Diakonov, and S. I. Troian. On the transverse momentum distribution of massive lepton pairs. *Phys. Lett.*, B79:269–272, 1978.

[4] G. Parisi and R. Petronzio. Small transverse momentum distributions in hard processes. *Nucl. Phys.*, B154:427, 1979.

[5] Guido Altarelli, R. K. Ellis, M. Greco, and G. Martinelli. Vector boson production at colliders: A theoretical reappraisal. *Nucl. Phys.*, B246:12, 1984.

[6] John C. Collins and Davison E. Soper. Back to back jets in qcd. *Nucl. Phys.*, B193:381, 1981.

[7] John C. Collins and Davison E. Soper. Back-to-back jets: Fourier transform from b to k- transverse. *Nucl. Phys.*, B197:446, 1982.

[8] J. C. Collins, Davison E. Soper, and George Sterman. Transverse momentum distribution in drell-yan pair and w and z boson production. *Nucl. Phys.*, B250:199, 1985.

[9] G. Parisi. Summing large perturbative corrections in qcd. *Phys. Lett.*, B90:295, 1980.

[10] Lorenzo Magnea and George Sterman. Analytic continuation of the sudakov form-factor in qcd. *Phys. Rev.*, D42:4222–4227, 1990.

[11] Tim Oliver Eynck, Eric Laenen, and Lorenzo Magnea. Exponentiation of the drell-yan cross section near partonic threshold in the dis and ms-bar schemes. *JHEP*, 06:057, 2003.

[12] Michael Kramer, Eric Laenen, and Michael Spira. Soft gluon radiation in higgs boson production at the lhc. *Nucl. Phys.*, B511:523, 1998.

[13] Robert V. Harlander and William B. Kilgore. Next-to-next-to-leading order higgs production at hadron colliders. *Phys. Rev. Lett.*, 88:201801, 2002.

[14] Robert V. Harlander and William B. Kilgore. Soft and virtual corrections to p p –> h + x at nnlo. *Phys. Rev.*, D64:013015, 2001.

[15] Charalampos Anastasiou and Kirill Melnikov. Higgs boson production at hadron colliders in nnlo qcd. *Nucl. Phys.*, B646:220–256, 2002.

[16] Charalampos Anastasiou, Kirill Melnikov, and Frank Petriello. Higgs boson production at hadron colliders: Differential cross sections through next-to-next-to-leading order. *Phys. Rev. Lett.*, 93:262002, 2004.

[17] V. Ravindran, J. Smith, and W. L. van Neerven. Nnlo corrections to the total cross section for higgs boson production in hadron hadron collisions. *Nucl. Phys.*, B665:325–366, 2003.

[18] V. Ravindran, J. Smith, and W. L. van Neerven. Differential cross sections for higgs production. *Mod. Phys. Lett.*, A18:1721–1734, 2003.

[19] Stefano Catani, Daniel de Florian, and Massimiliano Grazzini. Higgs production in hadron collisions: Soft and virtual qcd corrections at nnlo. *JHEP*, 0105:025, 2001.

[20] Stefano Catani, Daniel de Florian, Massimiliano Grazzini, and Paolo Nason. Soft-gluon resummation for higgs boson production at hadron colliders. *JHEP*, 0307:028, 2003.

[21] Eric Laenen, Gianluca Oderda, and George Sterman. Resummation of threshold corrections for single particle inclusive cross-sections. *Phys. Lett.*, B438:173–183, 1998.

[22] Stefano Catani, Michelangelo L. Mangano, and Paolo Nason. Sudakov resummation for prompt photon production in hadron collisions. *JHEP*, 9807:024, 1998.

[23] Stefano Catani, Michelangelo L. Mangano, Paolo Nason, Carlo Oleari, and Werner Vogelsang. Sudakov resummation effects in prompt photon hadroproduction. *JHEP*, 9903:025, 1999.

[24] Nikolaos Kidonakis and J. F. Owens. Soft-gluon resummation and nnlo corrections for direct photon production. *Phys. Rev.*, D61:094004, 2000.

[25] Paolo Bolzoni, Stefano Forte, and Giovanni Ridolfi. Renormalization group approach to sudakov resummation in prompt photon production. *Nucl. Phys.*, B731:85–108, 2005.

[26] Eric Laenen, George Sterman, and Werner Vogelsang. Higher-order qcd corrections in prompt photon production. *Phys. Rev. Lett.*, 84:4296, 2000.

[27] Eric Laenen, George Sterman, and Werner Vogelsang. Recoil and threshold corrections in short-distance cross sections. *Phys. Rev.*, D63:114018, 2001.

[28] George Sterman and Werner Vogelsang. Recoil and power corrections in high-x(t) direct-photon production. *Phys. Rev.*, D71:014013, 2005.

[29] Hsiang nan Li. Unification of the k(t) and threshold resummations. *Phys. Lett.*, B454:328, 1999.

[30] Anna Kulesza, George Sterman, and Werner Vogelsang. Joint resummation in electroweak boson production. *Phys. Rev.*, D66:014011, 2002.

[31] Stefano Catani, Michelangelo L. Mangano, Paolo Nason, and Luca Trentadue. The resummation of soft gluons in hadronic collisions. *Nucl. Phys.*, B478:273–310, 1996.

[32] P. Mathews et al. Working group report: Quantum chromodynamics. *Pramana*, 63:1367–1379, 2004. Proceedings of the Eighth Workshop on High Energy Physics Phenomenology, Mumbai, India, Jan. 2004.

[33] Anna Kulesza, George Sterman, and Werner Vogelsang. Joint resummation for higgs production. *Phys. Rev.*, D69:014012, 2004.

[34] Nikolaos Kidonakis, Gianluca Oderda, and George Sterman. Threshold resummation for dijet cross-sections. *Nucl. Phys.*, B525:299, 1998.

[35] V. M. Abazov et al. Measurement of the isolated photon cross section in $p\bar{p}$ collisions at $\sqrt{s} = 1.96$-tev. *Phys. Lett.*, B639:151–158, 2006.

[36] D. Acosta et al. Direct photon cross section with conversions at cdf. *Phys. Rev.*, D70:074008, 2004.

[37] L. Apanasevich et al. Measurement of direct photon production at tevatron fixed target energies. *Phys. Rev.*, D70:092009, 2004.

[38] Patrick Aurenche, Michel Fontannaz, Jean-Philippe Guillet, Eric Pilon, and Monique Werlen. A new critical study of photon production in hadronic collisions. *Phys. Rev.*, D73:094007, 2006.

[39] Daniel de Florian and Werner Vogelsang. Threshold resummation for the prompt-photon cross section revisited. *Phys. Rev.*, D72:014014, 2005.

[40] M. Gluck, E. Reya, and A. Vogt. Dynamical parton distributions revisited. *Eur. Phys. J.*, C5:461, 1998.

[41] A. Vogt. Efficient evolution of unpolarized and polarized parton distributions with qcd-pegasus. *Comput. Phys. Commun.*, 170:65–92, 2005.

Chapter 3

Monte Carlo Techniques

The term Monte Carlo methods covers a collection of algorithms used for simulating systems in nature. In contrast to other tools used for simulation, Monte Carlo methods are nondeterministic in the sense that they are based on stochastics[1]. Monte Carlo integration techniques have proven to be very efficient in computing multi-dimensional integrals numerically and such techniques are used in all chapters in this thesis. Another aspect of MC methods is the simulation of radiative corrections. As mentioned earlier it is very difficult, in practice, to take higher order effects into account in perturbation theory exactly and to arbitrary order. It is, however, possible to account for higher order effects to some degree through Monte Carlo showering, i.e. ordered emissions that have a stochastic nature.

In this chapter we begin by introducing the concepts of Monte Carlo integration. Subsequently we look at event generation and finally we consider an example that illustrates the merging of a toy NLO cross section with a Monte Carlo parton shower.

3.1 Integration

A straightforward approach to solving integrals numerically is considering averaged sums. Let $f(x)$ be a function which we want to integrate over the interval $[a : b]$. Then an estimate of the integral can be obtained by[2]

$$\int_a^b f(x)dx \sim \sum_{i=1}^{N} f(x_i)\Delta x = (b-a)\frac{1}{N}\sum_{i=1}^{N} f(x_i) \tag{3.1}$$

[1] By a stochastic process we understand that a given outcome is independent from the preceeding outcomes

[2] In our discussion we are not taking the accuracy of the integral approximations into account.

where we have assumed that the step size is the same in all dimensions. Here, in this simple example, Δx is constant. If we are dealing with a multi-dimensional integral the expression would become

$$\int_{a_1}^{b_1} \cdots \int_{a_m}^{b_m} dx_1 \cdots dx_m f(x_1, \ldots, x_m) \sim \frac{(b_1 - a_1) \cdots (b_m - a_m)}{N^m} \sum_{k_1=0}^{N} \cdots \sum_{k_m=0}^{N} f(x_{1_{k_1}}, \ldots, x_{m_{k_m}}) \tag{3.2}$$

It is apparent that the estimate becomes better as N is increased. The method is, however, slow in general and it works best if the function in question varies little over the whole interval.
In principle this formula does the job for most functions. However, if the function is multi-dimensional and is varying considerably over the integration volume there are more efficient ways of carrying out the integration.
One way of improving the integration efficiency is to consider adaptive integration combined with importance sampling. Adaptive integration is the first step in refining the above outlined integration. Imagine that the function being integrated is varying a little in some part of the integration volume, but varying quite a lot in other parts. Then, over the volume where it is rather flat the step-size Δx does not have to be as small as in the part of the volume where f varies a lot. This suggests to introduce a variable step-size $\Delta x \to \Delta x_i$. Hence with the same *amount* of steps one can achieve a better estimate than in eqn. (3.1). Of course there are some technicalities hidden in finding the optimal division of the integration volume - a topic we shall return to shortly.
Importance sampling deals with obtaining information about a function f, possibly from another function g which is (somewhat) similar to f and better known. We shall here show how this works in practice. Let us again assume we want to calculate the integral

$$I = \int_a^b f(x)dx \tag{3.3}$$

Then one can proceed in the following steps:

1. Try to guess/find a function $g(x)$ which is similar to f.
2. Rewrite the integrand: $f(x)dx = \frac{f(x)}{g(x)}g(x)dx$
3. Change variable: $dy = g(x)dx$.
4. Set $h(y) = f(x)/g(x)$. Thus we get $f(x)dx = \frac{f(x)}{g(x)}g(x)dx = h(y)dy$

Hence if g is a good approximation of f, h will be quite close to 1 over the whole interval of integration and hence the averaged sum using a uniform distribution of numbers $x_i \in [a : b]$, applied to h will give a good numerical evaluation of the integral.

A rather sophisticated and widely used algorithm was developed in the 70's called the *Vegas algorithm*, which makes use of adaptive integration and includes importance sampling in an automatized way [1], using an iterative approach.
Prior to the first iteration the integration area is initially divided into a uniform (possibly multi-dimensional) grid. Subsequently an algorithm, which measures the rate of change of the integrated function when going from one grid point to the next, is applied. Grid points where the rate of change is large are assigned a larger weight while grid points where the rate of change is rather limited (which amounts to the function being rather flat) a smaller weight. In the next iteration a new grid is made based on the information sampled in the previous iteration. The new grid is dense where the weights were large and diluted where they were low.
In each interation a new grid is created based on the actual behaviour of the function in question. This method assumes that the grid will start to converge to some stable grid after a certain amounts of iterations.
After a suitable amount of iterations shaping the grid, the grid is fixed, and the integration can begin. It is again done in a series of iterations, like the optimization of the grid. In each iteration the accuracy of the integral is improved. One may also create a histogram of the integrand.
There are other algorithms similar to VEGAS, for instance BASES [2] which is used in the MC@NLO framework.
We now proceed to discuss some other examples of Monte Carlo integration as well as the concept of event generation.

3.2 (Un)weighting: Integration and Event Generation

There are basically two approaches in numerical integration which in turn are equivalent. The first deals with so-called *weighted* events, where with "event" we mean one of the N random numbers in eqn. (3.1) or N sets of them in the case of a multi-dimensional integration (eqn. (3.2)). The events are generated randomly according to a *uniform* distribution but subsequently every event is assigned a weight proportional to some probability distribution. In a sense this is precisely how the just-described VEGAS algorithm works. Thus an algorithm describing weighted integration of a function f over the interval $[a : b]$ could look like the

following:

1. select a random number x', where $x' \in [a : b]$
2. evaluate $y = f(x')$
3. bin (x', y) accordingly in a histogram
4. finally normalize to the bin width
5. add up the area of all the bins. This could be a selection in the final iteration of a VEGAS algorithm in which case the VEGAS weight must be included in y.

As a more involved example we consider the weighted integration of a scattering amplitude squared. In general a cross section can be expressed as

$$\sigma = \int \prod_i \frac{d^3\mathbf{p}_i}{2E_i} |\mathcal{M}|^2 \tag{3.4}$$

Performing a variable transformation one gets

$$\sigma = \int_0^1 \prod_i dx_i \underbrace{\mathcal{J}|\mathcal{M}'(\vec{x})|^2}_{\text{weight } w(\vec{x})} \tag{3.5}$$

where $\mathcal{J}$ is the Jacobian mapping the $\vec{p}_i$ to $\vec{x} = (x_1, \ldots, x_n)$, where $0 \leq x_i \leq 1$ for all i. Thus the algorithm for generating weighted events, where events now correspond to a scattering according to the process represented by $\mathcal{M}$ with incoming and outgoing momenta determined by the random numbers, can be summarized in a couple of steps:

1. Pick $\{x_i\}$ according to a uniform distribution.
2. Determine the mapping $\{x_i\} \mapsto \{p_j(x_i)\}$.
3. Find e.g. the transverse momentum p_T of the desired particle.
4. Enter an entry in the corresponding histogram with weight $(\mathcal{J}|\mathcal{M}'|^2)(\{x_i\})$

A different approach is given by *unweighting*. Events are generated according to a distribution and recorded (binned) with a constant weight. The so-called *hit-and-miss* integration method is perhaps the simplest example of unweighted integration.
Let f be a (positive) function that is to be integrated on the interval $[a : b]$. Hit-and-miss works in the following way

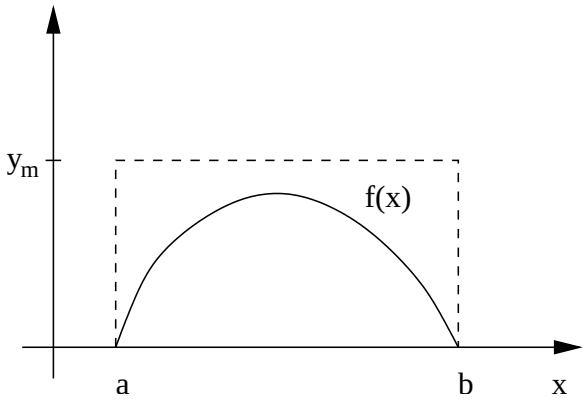

Figure 3.1: A sketch of the hit-and-miss method as described in the text.

1. First we determine the maximum value of f, $f_{max} = \max(f(x)|a \leq x \leq b)$ and subsequently choose a number $y_m \geq f_{max}$.
2. Pick a random number x' so that $x' \in [a : b]$.
3. Pick another random number $r \in [0 : 1]$
4. Compare: if $f(x')/y_m < r$ then accept.
   - else if $f(x')/y_m > 1'$ reject and return to 1.
5. Obtain the integral via $I = (b-a)y_m \frac{\text{accepted events}}{\text{total number of events}}$.

The situation is shown in fig. 3.1.

Unweighting mimics nature most directly, since nature does not assign weights to events; rather there are intrinsic probabilities for events to occur. Thus in our attempt to describe nature we model probability distributions according to which events are generated, and subsequently bin them with unit weight.

3.3 The Veto Algorithm

In our attempt to describe nature we need a mean to simulate the emission of cascades of partons, emitted from incoming and outgoing particles. Ideally we wish to do this in a way that uses unweighting. In the following we shall focus on such methods and this will be followed by a discussion of Monte Carlo showering.

Although we have cascade-type emissions from an incoming or outgoing parton in mind we start our discussion in general terms.
Let $\mathcal{P}(t)$ be a differential probability of an event occuring at t. Here t can be time,

energy (scale), momentum, etc. Thus $\mathcal{P}(t)dt$ returns the probability that an event occurs within t and $t + dt$. This, in turn, means that (since dt is added to t) the probability that nothing has happened at t must be less than or equal to $\mathcal{P}(t)dt$. If $\mathcal{N}(t)$ denotes the probability that nothing has happened by t then we must have the relation:

$$\mathcal{P}(t)dt = -d\mathcal{N} \tag{3.6}$$

This relation can also be obtained by posing the question: How does $\mathcal{N}$ change when $t \to t + dt$? We get the relation:

$$\mathcal{N}(t + dt) = \mathcal{N}(t) - f(t)dtd\mathcal{N}(t) \tag{3.7}$$

which is to be interpreted in the following way: at $t + dt$ the probability that nothing has happened is equal to the probability that nothing happened at t i.e. $\mathcal{N}(t)$ minus the probability that something happens at t, given that nothing happened before. Thus:

$$\mathcal{P}(t) = -\frac{\partial \mathcal{N}}{\partial t} = f(t)\mathcal{N}(t) \tag{3.8}$$

This differential equation is easily solved

$$\mathcal{P}(t) = f(t) \exp\left(- \int_{t_0}^{t} f(t')dt' \right) \tag{3.9}$$

This immediately gives the solution for $\mathcal{N}$

$$\mathcal{N}(0) - \mathcal{N}(t) = 1 - \exp\left(- \int_{0}^{t} f(t')dt' \right) \equiv 1 - \mathcal{R} \tag{3.10}$$

If there exists an F such that $F(t) - F(0) = \int_0^t f(t')dt'$ then we have

$$F(0) - F(t) = \ln \mathcal{R} \tag{3.11}$$

Since $\mathcal{N}$ is a probability eqn. (3.11) only makes sense if $\mathcal{R} \in [0 : 1]$. This has the following implication: if we wish to select t randomly according to some distribution we first select $\mathcal{R}$ randomly and uniformly from $[0 : 1]$. Then we find t by isolating it in eqn. (3.11):

$$t = F^{-1}(F(0) - \ln \mathcal{R}) \tag{3.12}$$

This method is called inverse transform sampling and works well when the function (distribution) f and its primitive F are well known. This is, of course, not always the case.

A Generalized Veto Algorithm

It would therefore be convenient to have a similar method but generalized to the case where F is not fully known or does not have a primitive function associated. If it is possible to find a function g with a known primitive G that approximates f and can function as a bound, i.e. has the properties $f(x) \leq g(x)\ \forall x \geq 0$ we can construct the following algorithm:

1. set $i = 0$ and $t_0 = 0$
2. $i = i + 1$ and select $t_i = G^{-1}\big((G(t_{i-1}) - \ln \mathcal{R})\big)$. Thus t_i is chosen according to g *but* with the requirement that $t_i \geq t_{i-1}$.
3. Select a new random number, $\mathcal{R}'$:
   - if $f(t_i)/g(t_i) \leq \mathcal{R}'$ reject t_i and return to 1.
   - if $f(t_i)/g(t_i) \leq \mathcal{R}'$ accept t_i

This method has a big advantage when f has peaks[3]. It is then possible to increase integration efficiency by choosing g (or a set of g_i's) in a clever way.
We now specify the discussion to Monte Carlo parton showers which are an example of the usage of the Veto algorithm.

3.4 MC Showering

In this section we describe MC emissions by first using the language of probability theory and subsequently motivating the main formula using physical arguments.

Let us consider the emission of photons with energy z_i, and a probability of emission given by $Q(z_i)/z_i$, i.e.

$$\mathcal{P}(\text{Any emission}) = \sum_{n=0}^{\infty} \frac{a^n}{n!} \prod_i \int \frac{dz_i}{z_i} Q(z_i) \exp\left(- a \int_0^1 \frac{dz}{z} Q(z) \right) = 1 \qquad (3.13)$$

The factor $1/n!$ is a symmetry factor. We shall now consider this formula in detail. We denote

$$\Delta(x_1, x_2) = \exp\left(- a \int_{x_1}^{x_2} \frac{Q(z)dz}{z} \right) \qquad (3.14)$$

the probability that *no* photon is emitted within the interval of energies given by $[x_1 : x_2]$. The reader may recognize this as a Sudakov factor. We shall return to

[3] By peaks we mean where the gradient of f is (numerically) large.

this issue in a short while. The exponential factor in eqn. (3.13) thus yields the probability that no emission takes place at *any* scale. This is multiplied by the probabilities of one emission, two emissions etc., and all these contributions are finally summed.
The function $Q(z)$ is required to have the following properties

$$0 \leq Q(z) \leq 1 \ , \ \lim_{z\to 0} Q(z) = 1 \ , \ \lim_{z\to 1} Q(z) = 0$$

Furthermore a is the "coupling" and thus if $a \to 0$ there should be no emission, while $a \to \infty$ there should be many emissions ($\Delta \to 0$ i.e. it becomes improbable that no emission takes place).
Eqn. (3.13) does not incorporate bounds on emissions, which are always present in realistic cases. Let us therefore analyse emission probabilities in the presence of energy cut-offs.
In a simulation of a scattering event the objective typically is to generate a number of events, say, N. In each of these events the system undergoes a cascade of emissions which will be simulated by a Monte Carlo code. Let x_M be the maximum energy an emitted photon can have, and x_0 be the lower boundary of the energy of a photon after a branching - i.e. x_0 is a cut-off scale. This means that there can be *no* emission if $z < x_0$. Therefore we must have:

$$\begin{aligned}
&\mathcal{P}(\text{no emission with } z > x_0) = \\
&\Big[\sum_n \frac{1}{n!} \overbrace{\int_0^{x_0} a\frac{Q(z_1)dz_1}{z_1}\int_0^{z_1} a\frac{Q(z_2)dz_2}{z_2}\cdots\int_0^{z_n} a\frac{Q(z_{n-1})dz_{n-1}}{z_{n-1}}}^{\left(a\int_0^{x_0}\frac{Q(z_i)dz_i}{z_i}\right)^n}\Big] \\
&\qquad \times \exp\left\{-a\int_0^{x_M}\frac{Q(z)dz}{z}\right\} \\
&\qquad \equiv \mathcal{P}(\text{ANY emission } 0 \leq z \leq x_0) \times \mathcal{P}(\text{NO emission } 0 \leq z \leq x_M)
\end{aligned} \tag{3.15}$$

Here x_M is an upper cut-off. We see that the first factor in eqn. (3.15) becomes

$$\sum_n \frac{a^n}{n!}\left(\int_0^{x_0}\frac{Q(z)dz}{z}\right)^n = \exp\left\{-a\int_0^{x_0}\frac{Q(z)}{z}dz\right\} \tag{3.16}$$

i.e. the sum of the possible emissions exponentiates nicely. From eqns. (3.15) and (3.16) we thus derive

$$\mathcal{P}(\text{no emission with } x_0 < z < x_M) = \exp\left\{-a\int_{x_0}^{x_M}\frac{Q(z)dz}{z}\right\} \tag{3.17}$$

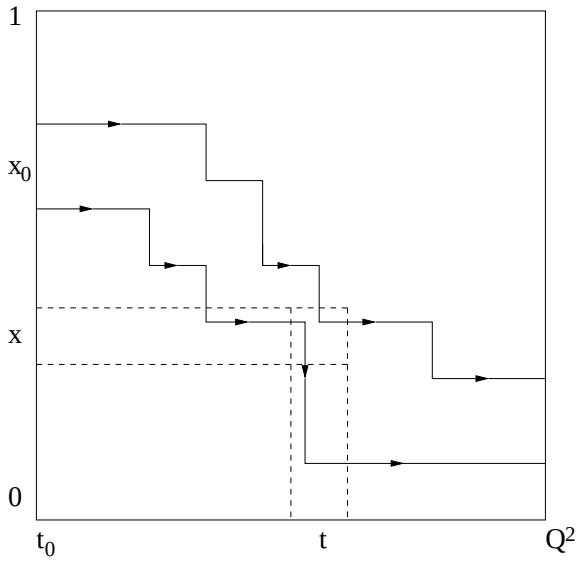

Figure 3.2: Figure showing parton branching following different paths in (t, x)-space [3].

As we shall now see this equation has well understood physical reasons as well.
Here we consider the initial-state case. Before a parton eventually participates in a (hard) scattering it typically goes through cascade of emissions [3]. This is pictured in the following way: a parton starts out at a low virtual mass-squared, $-t_0$ and carrying a momentum fraction of the mother particle (a hadron), x_0. Every subsequent branching, and hence emission, changes the values of $-t$ and x. Thus the branching can be described by a set of parameters $\{(-t_0, x_0), (-t_1, x_1), \ldots, (-t_n, x_n)\}$.
At the end the parton participates in the hard scattering at a scale, Q^2.
The branching of a parton into two other partons is described by a splitting function, $P_{ab}(z)$. Here a is the incoming parton, and b is one of the outgoing. Knowing a and b one can determine the third parton, c.
The question is now how the parton distributions change when an evolution $(t, x) \rightarrow (t + \delta t, x + \delta x)$ takes place due to an emission? Looking at fig. 3.2 we see that the change can be measured by calculating (number of arriving paths - number of leaving paths)$/\delta x$ in the volume element $(\delta t, \delta x)$. The total number of arriving paths is given by the integral of the probability of branching times the density of partons over all higher momentum fractions

$$\begin{aligned} \delta f_{in}(x,t) =& \frac{\delta t}{t} \int_x^1 dx' dz \frac{\alpha_s}{2\pi} \hat{P}(z) f(x',t) \delta(x - zx') \\ =& \frac{\delta t}{t} \int_0^1 \frac{dz}{z} \frac{\alpha_s}{2\pi} \hat{P}(z) f(\frac{x}{z}, t) \end{aligned} \tag{3.18}$$

The reader should note that the integrand vanishes for $z < x$, i.e. $x' > 1$ which is the reason why the latter integral ranges from 0 to 1.
Secondly, the total number of paths leaving the volume element is given by a similar integral but now we integrate over all *lower* momentum fractions:

$$\begin{aligned}\delta f_{out}(x,t) =& \frac{\delta t}{t} f(x,t) \int_0^x dx' dz \frac{\alpha_s}{2\pi} \hat{P}(z) \delta(x' - zx) \\ =& \frac{\delta t}{t} f(x,t) \int_0^1 dz \frac{\alpha_s}{2\pi} \hat{P}(z)\end{aligned} \tag{3.19}$$

Thus combining we get:

$$\begin{aligned}\delta f(x,t) =& \delta f_{in} - \delta f_{out} \\ =& \frac{\delta t}{t} \int_0^1 dz \frac{\alpha_s}{2\pi} \hat{P}(z) \left[\frac{1}{z} f(\frac{x}{z}, t) - f(x,t) \right]\end{aligned} \tag{3.20}$$

This equation can be rewritten by defining $P(z) \equiv \hat{P}(z)_+$, where $\hat{P}(z)_+$ is the plus distribution (see eqn. (1.4)). Thus we get:

$$\begin{aligned}\delta f(x,t) =& \frac{\delta t}{t} \int_0^1 dz \frac{\alpha_s}{2\pi} \hat{P}(z) \left[\frac{1}{z} f(\frac{x}{z}, t) - f(x,t) \right] \\ & \Rightarrow \\ t \frac{\partial}{\partial t} f(x,t) =& \int_x^1 \frac{dz}{z} \frac{\alpha_s}{2\pi} P(z) f(\frac{x}{z}, t)\end{aligned} \tag{3.21}$$

which is nothing but the DGLAP equation [4, 5, 6].
This leads us to introduce the function

$$\Delta(t) \equiv \exp \left[- \int_{t_0}^t \frac{dt'}{t'} \int dz \frac{\alpha_S}{2\pi} \hat{P}(z) \right] \tag{3.22}$$

which we recognize as the *Sudakov* form factor. This factor describes the probability of evolution from t_0 to t without having a branching. Furthermore we see that it is a function of the type shown in eqn. (3.13). If we substitute the expression in eqn. (3.22) into eqn. (3.20)

$$t \frac{\partial}{\partial t} f(x,t) = \int \frac{dz}{z} \frac{\alpha_s}{2\pi} P(z) f(\frac{x}{z}, t) + \frac{f(x,t)}{\Delta(t)} t \frac{\partial}{\partial t} \Delta(t) \tag{3.23}$$

which, after rewriting, becomes the differential equation:

$$t \frac{\partial}{\partial t} \left(\frac{f}{\Delta} \right) = \frac{1}{\Delta} \int \frac{dz}{z} \frac{\alpha_s}{2\pi} P(z) f(\frac{x}{z}, t) \tag{3.24}$$

Solving for f we obtain:

$$f(x,t) = \Delta(t) f(x,t_0) + \int_{t_0}^{t} \frac{dt'}{t'} \frac{\Delta(t)}{\Delta(t')} \int \frac{dz}{z} \frac{\alpha_s}{2\pi} \hat{P}(z) f(x/z, t') \tag{3.25}$$

The equation is to be interpreted as follows [3]: the first term on the RHS describes the paths in fig. 3.2 that do not branch between t_0 and t. Here we notice that, in accordance with the derived results (eqns. (3.13)-(3.17)), the Sudakov form factor is the probability of having no emissions between t_0 and t. The second term gives the contribution coming from all paths that have their last branching at scale t'. In particular the factor $\Delta(t)/\Delta(t')$ is the probability of evolving from t' to t without emission.

3.5 MC Showers and NLO precission

In the preceding section we have discussed the mechanisms of Monte Carlo showering. In most of the well-known MC programs, such as PYTHIA [7] and HERWIG [8], showering is merged with LO cross sections in an attempt to take into account soft and collinear emissions. From a technical point of view it has been known for a long time now how to interface the showers with a LO cross section. When merging the MC showers with a higher order cross section the situation becomes less transparent. A NLO cross section, for instance, already includes *one* extra real emission. This means that when merging with a MC shower one runs into the risk of double counting, i.e. that one of the emissions of the shower will be identical to the real emission, accounted for by the NLO calculation, already. A second issue that makes the treatment of NLO cross sections more difficult is that of virtual corrections. Virtual contributions can negative, which allows for generation of negative weights. In the case of MC@NLO, to be discussed in the following chapters, these are simply kept track of, and so far have not played a large role. It is even possible to define a merging scheme to remove them altogether [9].
Here we shall schematically indicate, using a toy model, how the double-counting problem is solved in the case of MC@NLO.

3.5.1 Toy Example

In this section we shall consider a toy example (which follows the outline in [10]). This example will illustrate what is needed when interfacing a (toy) NLO cross section with a MC shower.

We imagine a process in which additional photons can be emitted with energy

x. Let us assume that we have a "NLO" cross section that can be written as

$$\frac{d\sigma_{\text{total}}}{dx} = \left(\frac{d\sigma}{dx}\right)_B + \left(\frac{d\sigma}{dx}\right)_V + \left(\frac{d\sigma}{dx}\right)_R \tag{3.26}$$

where

$$\begin{aligned}\left(\frac{d\sigma}{dx}\right)_B &= B\delta(x),\\ \left(\frac{d\sigma}{dx}\right)_V &= a\left(\frac{B}{2\epsilon} + V\right)\delta(x)\\ \left(\frac{d\sigma}{dx}\right)_R &= a\frac{R(x)}{x}\end{aligned} \tag{3.27}$$

The subscripts here indicate B for Born level, V for virtual and R for real emission. The function describing the real emissions must reduce to the Born cross section in the very soft limit, i.e. we must have

$$\lim_{x\to 0} R(x) = B \tag{3.28}$$

In our example we choose R to be:

$$R(x) = B + x(1 + \frac{x}{2} + 20x^2) \tag{3.29}$$

To determine the distribution of an observable in MC@NLO$\mathcal{O}$ the following integral has to be calculated [10]:

$$\left(\frac{d\sigma}{d\mathcal{O}}\right) = \int_0^1 dx \Bigg[\underbrace{I_{MC}(\mathcal{O}, x_M(x))\frac{\alpha(R(x) - \overbrace{BQ(x)}^{\text{parton shower @ } \mathcal{O}(\alpha)})}{x}}_{\text{Real emission + MC shower}} + \underbrace{I_{MC}(\mathcal{O}, 1)\left(B + \alpha V - \frac{\alpha B(Q(x)-1)}{x}\right)}_{\text{(LO \& virtual) + MC shower}} \Bigg] \tag{3.30}$$

The terms B, V and R are the Born, Virtual and Real parts, respectively. The function I_{MC} is the interface between the parton shower and the respective parts of the NLO cross section. It depends, of course on the observable ($\mathcal{O} = p_T, y, \ldots$), and on the starting energy. In the first term the starting energy, $x_M(x)$, accounts for the fact thath a NLO emission with energy x has already occured. In the second term the maximum energy is still available. We see that in both of the main terms there is a subtraction taking place. This avoids an overlap between a

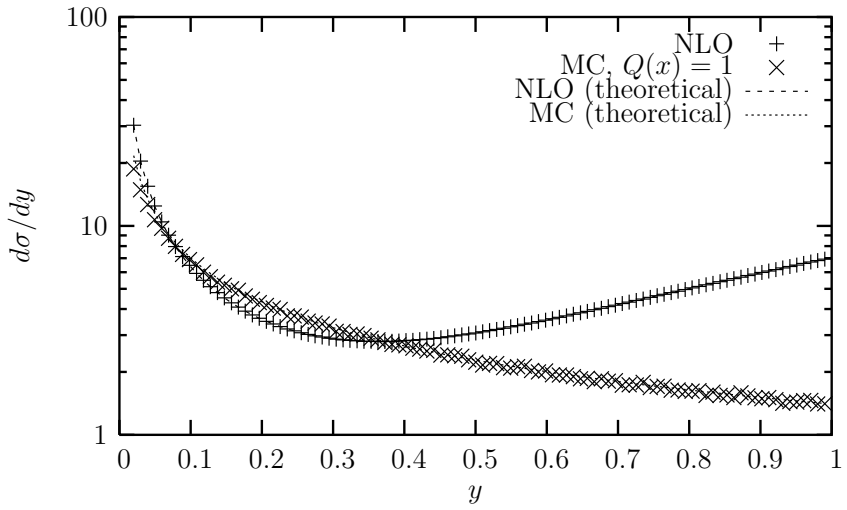

Figure 3.3: NLO and MC results.

real emission and the same emission from the parton shower.
To illustrate we now consider an inclusive variable defined to be:

$$y = \max(x_1, \ldots, x_n) \tag{3.31}$$

where n is the number of emissions in one given event and the x_i are the energies of the emissions. Let us describe the (differential) cross section in terms of a NLO and a MC part i.e.:

$$\begin{aligned} \left(\frac{d\sigma}{dy}\right)_{\text{NLO}} &= a\frac{R(y)}{y} \\ \left(\frac{d\sigma}{dy}\right)_{\text{MC}} &= aB\frac{Q(y)}{y}\Delta(y,1) \end{aligned} \tag{3.32}$$

Numerically this is then treated in the following way:

- The NLO part is integrated by usage of unweighted integration (hit and miss)
- The MC term is integrated by running the Monte Carlo algorithm outlined in section 3.4.

The result is shown in fig. 3.3 We observe the different nature of the NLO result and the MC result and hence also the potential problem of matching and merging the two contributions into one cross section.

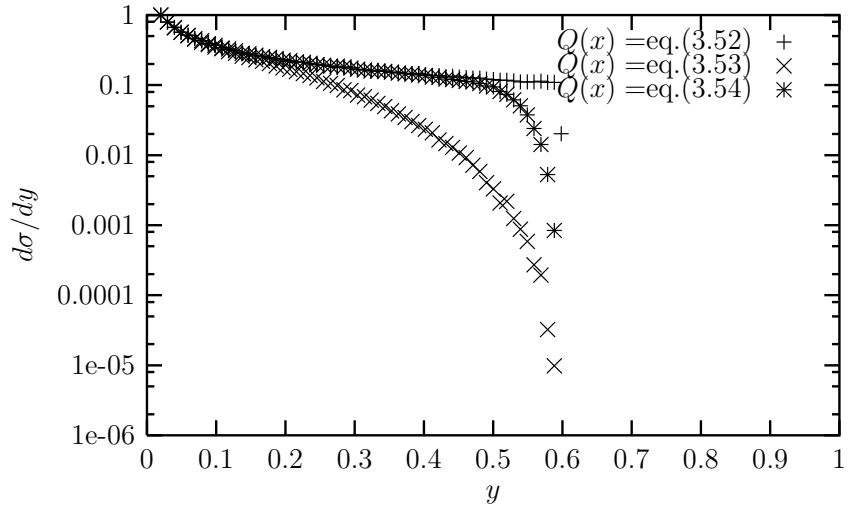

Figure 3.4: MC results with the three choices of Q, mentioned in the text.

We proceed with studying the merger of the MC part with the NLO. A dead zone is imposed on the MC part, here chosen to be $x_{dead} = 0.6$. This means that emissions with energies above x_{dead} are prohibited and this is done in order to (empirically) match the MC shower with the NLO. The dead zone can be incorporated by chosing suitable forms of the Q function.
Here we choose three different functions, all implementing the dead zone:

$$\begin{aligned} &1. \quad Q(x) = \Theta(x_{dead} - x) \\ &2. \quad Q(x) = \Theta(x_{dead} - x) G(x/x_{dead}), \text{with } \alpha = 1, \beta = 1, c = 1 \\ &3. \quad Q(x) = \Theta(x_{dead} - x) G(x/x_{dead}), \text{with } \alpha = 2, \beta = 1, c = 4 \end{aligned} \tag{3.33}$$

where the smoothing function G is given by:

$$G(x) = \frac{c^2(1-x)^{2\beta}}{x^{2\alpha} + c^2(1-x)^{2\beta}} \tag{3.34}$$

In fig. 3.4 the three different choices are shown and it is apparent that the difference between the three choices is rather large. Next we we examine the effect of the matching with the NLO part. This is shown in fig. 3.5. The difference between the three curves is hardly noticable. From the shape and comparing with fig. 3.3 we see that the NLO part dominates for larger values of y while the low to mid range it is mainly the MC showers that determine the shape.
Indeed the MC@NLO prescription in eqn. (3.30) merges the two descriptions well. This example illustrates the essential features of the MC@NLO approach. Details for realistic cases can be found in refs. [10, 11, 12].

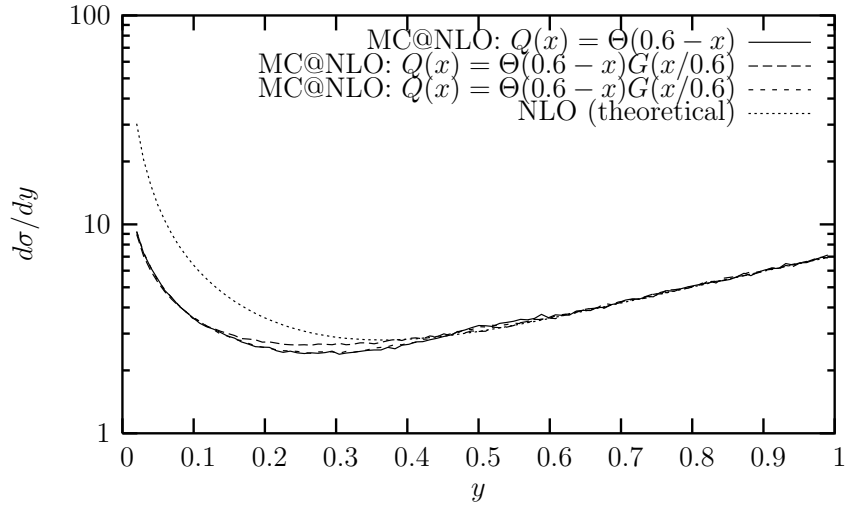

Figure 3.5: MC results with the three choices of Q, mentioned in the text.

References

[1] G. Peter Lepage. Vegas: An adaptive multidimensional integration program. CLNS-80/447.

[2] Setsuya Kawabata. A new version of the multidimensional integration and event generation package bases/spring. *Comp. Phys. Commun.*, 88:309–326, 1995.

[3] R. Keith Ellis, W. James Stirling, and B. R. Webber. Qcd and collider physics. *Camb. Monogr. Part. Phys. Nucl. Phys. Cosmol.*, 8:1–435, 1996.

[4] V. N. Gribov and L. N. Lipatov. Deep inelastic e p scattering in perturbation theory. *Yad. Fiz.*, 15:781–807, 1972.

[5] G. Altarelli and G. Parisi. Asymptotic freedom in parton language. *Nucl. Phys.*, B126:298, 1977.

[6] Yu. L. Dokshitzer. Calculation of the structure functions for deep inelastic scattering and e+ e- annihilation by perturbation theory in quantum chromodynamics. (in russian). *Sov. Phys. JETP*, 46:641–653, 1977.

[7] Torbjorn Sjostrand. High-energy physics event generation with pythia 5.7 and jetset 7.4. *Comput. Phys. Commun.*, 82:74–90, 1994.

[8] G. Corcella et al. Herwig 6: An event generator for hadron emission reactions with interfering gluons (including supersymmetric processes). *JHEP*, 01:010, 2001.

[9] Stefano Frixione, Paolo Nason, and Giovanni Ridolfi. The powheg-hvq manual version 1.0, 2007.

[10] Stefano Frixione and Bryan R. Webber. Matching nlo qcd computations and parton shower simulations. *JHEP*, 06:029, 2002.

[11] Stefano Frixione, Paolo Nason, and Bryan R. Webber. Matching nlo qcd and parton showers in heavy flavour production. *JHEP*, 08:007, 2003.

[12] Stefano Frixione, Eric Laenen, Patrick Motylinski, and Bryan R. Webber. Single-top production in mc@nlo. *JHEP*, 03:092, 2006.

Chapter 4

Single-top production in MC@NLO

Heavy flavour production at hadron colliders has been the subject of extensive theoretical and experimental studies for more than twenty years. The discovery of the top quark has offered an excellent opportunity to test QCD predictions much more reliably than in the case of bottom or charm, thanks to the smaller value of α_s and the relatively minor impact of long-distance effects, the top having no time to hadronize before decay. At present, all comparisons between theory and data concern $t\bar{t}$ pair production; a crucial role in the satisfactory agreement between predictions and experimental results is played by the next-to-leading order (NLO) QCD corrections [1, 2, 3, 4], which enlarge the leading-order cross section by about 30% at the Tevatron. A companion process to pair production is that in which a single top quark is present in the final state. In such a case, a weak-interaction Wtb vertex is involved, and thus the single-t cross section is smaller than the one for $t\bar{t}$ (in spite of being favoured by phase space volume), which so far has prevented observation of such a production mechanism by Tevatron experiments. In terms of Standard Model physics, single-t production is a direct probe of the weak interactions of the top, which in fact constitutes the main interest of single-t signals. Amongst other things, this may lead to measurements that have not been performed so far, namely of the CKM matrix element V_{tb}, and of the b parton density. Single-t production is in addition an important background for many searches for new physics, and can in general be seen as an effective way to study new physics phenomena in the heavy sector.

For single-t searches, or counting experiments in which single-t is a background, it is crucial to have a reliable estimate of the number of events expected, i.e. of the total rate. In this respect, NLO results are mandatory, also in view of the fact that they allow a sensible assessment of the size of unknown contributions of higher orders. Calculations of fully-differential NLO single-t cross sections have been performed in refs. [5, 6, 7, 8] and, including NLO top quark decay, in refs. [9, 10, 11, 12, 13]. On the other hand, in order to optimize acceptance cuts in an

experimental analysis, or to perform full detector simulations, one needs realistic hadron-level events, which are obtained with Monte Carlo event generators that incorporate the simulation of parton showers and hadronization models.

The complementary benefits of fixed-order computations and parton shower simulations have been discussed at length in the literature, as well as the advantages of combining them into a framework which would retain the strong points of each of them. The MC@NLO approach [14, 15] (we shall refer to these papers as to **I** and **II** respectively hereafter) provides a way of achieving this, by allowing one to match cross sections computed at NLO in QCD with an event generator. No modifications to the latter are necessary, and therefore *existing* parton shower Monte Carlos can be used for this purpose.

Although the MC@NLO formalism has been defined in full generality in **I**, explicit implementation details have been given there only for processes with no final-state QCD emissions at the level of hard reactions. Such a case has been considered later in **II**, with the implementation of $t\bar{t}$ and of $b\bar{b}$ production. In the context of MC@NLO, a *process-independent* calculation is required for each type of soft and/or collinear singularity which appears in the NLO real matrix elements. A quick inspection of the processes implemented so far (see ref. [16]) should convince the reader that the *only* singularity structure untreated is the final-state collinear one. We shall deal with this singularity in this chapter. It must be clear that, as for all of the other singularities which have been studied previously, our formulation will not depend on the fact that the specific single-t production process is considered here: in the derivation of the analytical formulae the nature of the hard reaction is irrelevant (which is further evidenced by the fact that the inclusion of single-t production in MC@NLO relies significantly on results obtained in **I** and **II**). What we achieve here is therefore, besides the addition of an important process to the MC@NLO framework, the capability of including other processes in MC@NLO without the need of performing further analytical computations, notably those having final-state (massless) partons at lowest order.

This chapter is organized as follows: in sect. 4.1 we discuss single-t production in the context of fixed-order computations and Monte Carlo simulations. Sect. 4.1.1 reviews the status of the matrix elements used in the present computation. We limit ourselves here to implementing the s- and t-channel production mechanisms, and neglect spin correlations in production. In sect. 4.1.1 we show that some changes can be made in the subtraction formalism [17, 18] upon which MC@NLO is based, which leave its analytical expression unaffected, but improve its numerical stability. We then proceed to sect. 4.1.2, where we write down the approximate single-t production cross sections generated by HERWIG, which enter the definition of the MC subtraction terms needed for the matching with NLO results. Implementation details of MC@NLO, concerning in particular the

simultaneous presence of initial- and final-state collinear singularities, are given in sect. 4.2. We present results for single-t production at the Tevatron in sect. 4.3; phenomenological studies, including results for the LHC, will be the subject of the next chapters. Finally, conclusions and future prospects are reported in sect. 4.4. Some technical details are collected in the Appendices.

4.1 Single-top cross sections

Each process in MC@NLO is based on two main building blocks: a fully-exclusive NLO computation; and the knowledge of the so-called MC subtraction terms, which are closely related to the first non-trivial order in the formal α_s expansion of the HERWIG Monte Carlo result. We shall treat these two issues in turn.

4.1.1 NLO computation

Fully-exclusive observable predictions do not strictly exist in QCD: the theory has finite resolution power, in the sense defined by the KLN theorem. However, we can conventionally talk of fully-exclusive computations, as those in which the cancellation of the infrared singularities is *formally* achieved analytically in an observable-independent manner, and the four-momenta of all of the final-state partons are available for defining the observables – this does not violate the KLN theorem, since the formal cancellation mentioned above actually occurs only in the case of infrared-safe observables. Fully-exclusive computations are crucial for the matching of NLO cross sections with Monte Carlos, since the latter need to know the four-momenta of all the particles involved in the hard process in order to compute the initial conditions and the various branching probabilities for the parton showers. Modern computations of this kind are based on universal subtraction or slicing formalisms; we shall discuss the one used within MC@NLO in sect. 4.1.1. Before doing that, we give some details specific to the matrix elements for single-t production.

Matrix elements

The lowest-order parton level processes are customarily divided into three classes that will also serve to categorize the NLO contributions. They are shown in fig. 4.1. In the first diagram the single top quark is produced in the annihilation process

$$u + \bar{d} \to t + \bar{b}\,, \tag{4.1}$$

via a time-like W boson, and is therefore called the s-channel process. In the second diagram, the initial bottom quark is converted into a top quark via the

exchange of a W-boson

$$b + u \to t + d\,, \tag{4.2}$$

and is therefore called the t-channel process. The final two graphs represent the Wt process in which the top quark is produced in association with a real W

$$b + g \to W + t\,. \tag{4.3}$$

The cross section for this process occurring at the Tevatron is very small and we neglect it here. For the LHC this process becomes non-negligible however. Note that in reactions (4.1) and (4.2) we have only listed the CKM-dominant combinations of quark flavours, but all CKM-allowed combinations are included in this chapter. Consistently, the b quark is always assumed to be massless.

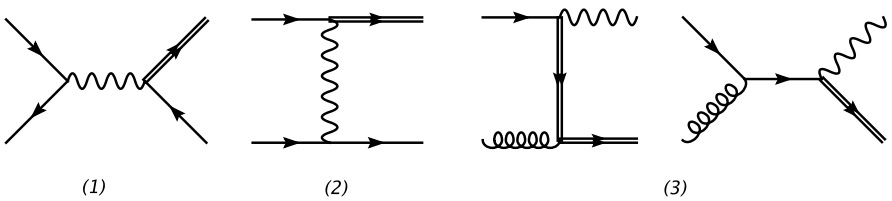

Figure 4.1: Leading order diagrams for single-t production in the (1) s-channel, (2) t-channel and (3) Wt-mode. The t-quark line is doubled.

In NLO one must include virtual and real corrections to the s- and t-channel processes. The virtual corrections consist of vertex corrections to diagrams *(1)* and *(2)* in fig. 4.1, together with the self-energy corrections to the t-quark line[1]. We shall not discuss these corrections in detail, nor give their explicit expressions, as these are already given in the literature. To prepare a remark on single-antitop production further below, we recall here that the vertex correction in the first diagram of fig. 4.2 is proportional to the lowest order vertex $\gamma^\mu(1-\gamma_5)$ because only light quark lines are attached to it. If the top quark line is attached as in the second diagram of fig. 4.2, a second form factor appears at NLO, proportional to the difference $(p_t^\mu - p_b^\mu)/m_t$. A similar situation occurs in the t-channel.

Concerning the real-emission corrections, we categorize these processes by the

[1]Box graphs vanish since they involve a single colour matrix on a fermion line, i.e. a null trace.

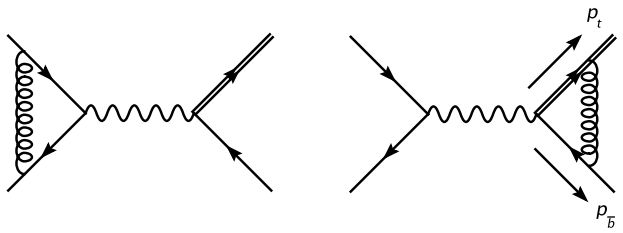

Figure 4.2: Virtual vertex corrections to s-channel single-t production.

dominant CKM contributions, as follows

$$u\bar{d} \longrightarrow t\bar{b}g\,, \tag{4.4}$$
$$ub \longrightarrow tdg\,, \tag{4.5}$$
$$b\bar{d} \longrightarrow t\bar{u}g\,, \tag{4.6}$$
$$ug \longrightarrow t\bar{b}d\,, \tag{4.7}$$
$$\bar{d}g \longrightarrow t\bar{b}\bar{u}\,, \tag{4.8}$$
$$bg \longrightarrow td\bar{u}\,. \tag{4.9}$$

A rather detailed discussion of these processes, and how they are assigned to s- and t-channel, can be found in the next section.

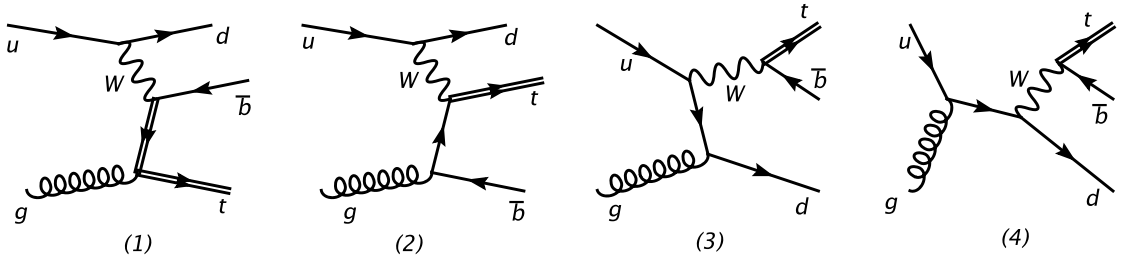

Figure 4.3: Diagrams contributing to $ug \to t\bar{b}d$.

The calculation of the single-$\bar{t}$ cross section is perfectly similar to that for the single-t described above, after charge conjugation. It may be perhaps less apparent that the second vertex form factor, mentioned above, proportional to $(p_{\bar{t}} - p_b)/m_t$ remains unchanged, since the quark propagators change the sign of the mass term. However the charge flow of the conjugated amplitude is also reversed, resulting in an unchanged expression.

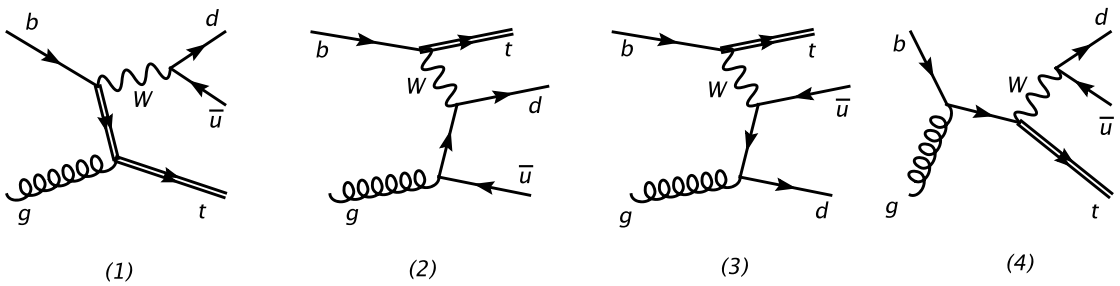

Figure 4.4: Diagrams contributing to $bg \to td\bar{u}$.

Subtraction procedure

In order to implement a process in MC@NLO, its NLO cross section must be computed according to the subtraction formalism presented in refs. [17, 18] (denoted as FKS henceforth). The basic idea in FKS is that of partitioning the phase space of the final-state partons involved in real-emission contributions, in such a way that the resulting regions do not overlap, cover the whole phase space, and each of them contains at most one collinear and one soft singularity. In each of these regions it is natural to select the one parton (called the FKS parton here) with which the singularities are associated. Denoting by $\mathcal{M}^{(r)}$ the generic real matrix elements, this amounts to writing[2]

$$1 = \sum_i \mathcal{S}_i^{(0)} + \sum_{ij} \mathcal{S}_{ij}^{(1)} , \tag{4.10}$$

$$\mathcal{M}^{(r)} = \sum_i \mathcal{S}_i^{(0)} \mathcal{M}^{(r)} + \sum_{ij} \mathcal{S}_{ij}^{(1)} \mathcal{M}^{(r)} . \tag{4.11}$$

The FKS parton is labelled with i in eqs. (4.10) and (4.11). The first term on the r.h.s. of eqn. (4.11) gives a divergent contribution (i.e., a contribution which has to be subtracted) only in the infrared regions in which parton i is soft and/or collinear to one of the initial-state partons. Analogously, the only infrared regions in which the second term on the r.h.s. of eqn. (4.11) is divergent are those in which parton i is soft and/or collinear to final-state parton j. More precisely, denoting by p_α and k_α the four-momenta of the initial- and final-state particles respectively,

[2]The notation of refs. [17, 18] has been slightly changed here in order to simplify the discussion. Functions $\mathcal{S}$ present in this chapter play the same role as functions Θ in ref. [18].

we have

$$\lim_{k_i^0 \to 0} \left(\mathcal{S}_i^{(0)} + \sum_j \mathcal{S}_{ij}^{(1)} \right) = 1 \,, \tag{4.12}$$

$$\lim_{\vec{k}_i \| \vec{p}_1} \mathcal{S}_i^{(0)} = 1 \,, \tag{4.13}$$

$$\lim_{\vec{k}_i \| \vec{p}_2} \mathcal{S}_i^{(0)} = 1 \,, \tag{4.14}$$

$$\lim_{\vec{k}_i \| \vec{k}_j} \mathcal{S}_{ij}^{(1)} = 1 \,, \tag{4.15}$$

while all the other infrared limits not explicitly listed above are zero[3]. Eqs. (4.12)–(4.15) are the *only* properties of the $\mathcal{S}$ functions used in the analytical computations of refs. [17, 18]; their actual functional forms away from the infrared limits are only relevant to numerical integrations. It should be stressed that all partons in the final state may induce a divergence of the real matrix elements; to take this fact into account, the role of FKS parton is given to each parton in turn, which is formally expressed in eqn. (4.11) by the sum over i that appears on the r.h.s. there.

After the phase space of the final-state partons is effectively partitioned through eqn. (4.11) into different infrared-singular regions, FKS chooses a different phase-space *parametrization* in each of these regions. It must be clear that the phase space is always the same, i.e. that relevant to the n particles involved in real-emission processes; the only difference between the various regions is in the choice of the integration variables which are left after getting rid of the δ functions that appear in the phase-space definition. The integration variables are chosen to perform the necessary analytical integrations in an easy way, and to facilitate importance sampling in numerical integrations. The key variables in the phase-space parametrization associated with $\mathcal{S}_i^{(0)}$ are the energy of parton i (directly related to soft singularities), and the angle between parton i and one of the initial-state partons (directly related to initial-state collinear singularities). For $\mathcal{S}_{ij}^{(1)}$, the energy of parton i and the angle between parton i and parton j (related to a final-state collinear singularity) are chosen instead. Obviously, the indices i and j are dummy here (phase spaces are flavour blind), and therefore there are only two independent functional forms for phase spaces in FKS, which loosely speaking are relevant to initial- and to final-state emissions. More details, and specific functional forms, are given in appendix C.

After the partition of the phase space, achieved by means of $\mathcal{S}_i^{(0)}$ and $\mathcal{S}_{ij}^{(1)}$, it is the matrix elements that determine whether a singularity actually occurs in a given

[3]The superscripts (0) and (1) are legacy notation from ref. [17], where these S-functions are related to jet-finding algorithms, and the superscripts indicate the algorithm step at which a merging takes place.

region of such a partition. As a general rule, one should choose the simplest possible forms for the $\mathcal{S}$ functions that still allow subtraction of all singularities. Although this is by no means mandatory (a region without singularities will simply give a finite contribution to the cross section), it is beneficial for well-behaved numerical computations. Since single-t matrix elements have a singularity structure much simpler than that of the matrix elements considered in refs. [17, 18], the $\mathcal{S}$ functions will also be simpler here. We also want to use the present process as a test case, and will define the $\mathcal{S}$'s as smooth functions of invariants, at variance with the original formulation of refs. [17, 18], in which they have been expressed as products of Θ functions.

We start by denoting the four-momenta entering an NLO tree-level single-t production process as follows

$$\alpha(p_1) + \beta(p_2) \longrightarrow t(k_1) + \gamma(k_2) + \delta(k_3)\,, \tag{4.16}$$

where α and β are the incoming partons from the left ($p_1^3 > 0$) and from the right ($p_2^3 < 0$) respectively; γ and δ denote light final-state partons. We shall use the following shorthand notation

$$(\alpha, \beta; t, \gamma, \delta) \tag{4.17}$$

for the momentum assignment of eqn. (4.16).

We first consider process (4.4); the treatment of processes (4.5) and (4.6) is identical[4]. We assign momenta as follows:

$$(u, \bar{d}; t, \bar{b}, g)\,. \tag{4.18}$$

By inspection of the relevant Feynman diagrams, we immediately conclude that the only singularities are associated with the gluon: the final-state light quark cannot give rise to a collinear divergence, being in all cases connected to a W boson. Therefore, for such processes the gluon will always be the FKS parton and, according to the discussion given at the beginning of this section, we can choose the $\mathcal{S}$ functions in such a way that the only non-zero ones are $\mathcal{S}_3^{(0)}$ and $\mathcal{S}_{32}^{(1)}$. In particular, with the following forms

$$\mathcal{S}_3^{(0)} = \frac{(k_3\cdot k_1)^a (k_3\cdot k_2)^a}{(k_3\cdot k_1)^a (k_3\cdot k_2)^a + (k_3\cdot p_1)^a (k_3\cdot p_2)^a}\,, \tag{4.19}$$

$$\mathcal{S}_{32}^{(1)} = \frac{(k_3\cdot p_1)^a (k_3\cdot p_2)^a}{(k_3\cdot k_1)^a (k_3\cdot k_2)^a + (k_3\cdot p_1)^a (k_3\cdot p_2)^a}\,, \tag{4.20}$$

equations (4.10)–(4.15) are fulfilled ($i \equiv 3$, the gluon being the FKS parton). In eqs. (4.19) and (4.20) a is an *arbitrary* positive real number; the physical results

[4] It is immediate to see that the procedure adopted here to disentangle the singularities of $(\alpha, \beta; t, \gamma, \delta)$ works identically for $(\beta, \alpha; t, \gamma, \delta)$.

will not depend on a, and their stability against the variation of a will constitute a check of the correctness of our implementation. It is clear that the numerators of eqs. (4.19) and (4.20) will act as damping factors for final- and initial-state collinear singularities respectively; the larger a, the stronger the damping. Formally, in the $a \to \infty$ limit we could recover the Θ-based implementation of the $\mathcal{S}$ functions of refs. [17, 18]. More pragmatically, we shall use the freedom in the choice of a to improve, if necessary, the numerical stability of the result, and will study its impact on the number of negative-weight events in MC@NLO, see section 4.3.

We now turn to the case of process (4.7); the corresponding Feynman diagrams are shown in fig. 4.3. There are only initial-state collinear singularities in this case, due to the splittings $g \to b\bar{b}$ (graph 2) and $g \to d\bar{d}$ (graph 3). On the other hand, these two diagrams do not interfere: the former contributes to the t-channel cross section, the latter to the s-channel one. Since s- and t-channel contributions are integrated separately, we are in the same situation as process (4.4) (i.e., only one parton can give singularities), except for the fact that no final-state singularities are present in this case. Therefore, we can set $\mathcal{S}^{(1)} = 0$ here, which implies $\mathcal{S}^{(0)} = 1$. It also implies that we are in the same situation as that treated in **I** (which also applies to many other processes implemented in MC@NLO). This situation now naturally appears as a particular case of a more general implementation in which singularities are disentangled by means of $\mathcal{S}$ functions.

Since process (4.8) is completely analogous to process (4.7), we finally deal with process (4.9), whose Feynman diagrams are shown in fig. 4.4. Of those, graphs 1 and 4 contribute to the Wt mode, which has not been considered here and are therefore dropped, while graphs 2 and 3 contribute to the t-channel. Graph 2 (graph 3) is singular when the $\bar{u}$ (d) is emitted collinearly to the initial-state gluon; since the two diagrams do interfere, we disentangle the singularities by means of the $\mathcal{S}$ functions. We assign the momenta according to

$$(b, g; t, d, \bar{u})\,, \tag{4.21}$$

and we define

$$\mathcal{S}_2^{(0)} = \frac{(k_3\cdot p_1)^a (k_3\cdot p_2)^a}{(k_2\cdot p_1)^a (k_2\cdot p_2)^a + (k_3\cdot p_1)^a (k_3\cdot p_2)^a}\,, \tag{4.22}$$

$$\mathcal{S}_3^{(0)} = \frac{(k_2\cdot p_1)^a (k_2\cdot p_2)^a}{(k_2\cdot p_1)^a (k_2\cdot p_2)^a + (k_3\cdot p_1)^a (k_3\cdot p_2)^a}\,, \tag{4.23}$$

which again fulfill equations (4.10)–(4.15). Although the same arbitrary parameter a as in eqs. (4.19) and (4.20) has been used here, this is in fact not necessary; we could introduce another free parameter, independent of a.

We conclude this section by stressing that the functional dependences of the $\mathcal{S}$ functions given above are correlated with the momentum assignments chosen for

the corresponding subprocesses. For example, eqs. (4.22) and (4.23) imply that the FKS parton will have four-momentum k_2 and k_3 respectively. Clearly, the subtraction formalism is independent of the particular labeling adopted for each process. Therefore, through a relabeling we can always assign four-momentum k_3 to the FKS parton. Such relabeling is a purely formal trick to render manifest the local matching between NLO matrix elements and MC subtraction terms.

As far as processes (4.4)–(4.6) are concerned, we pointed out before that only the gluon can play the role of FKS parton. Thus, the momentum assignment in eqn. (4.18) and the analogous ones

$$(u, b; t, d, g) \tag{4.24}$$
$$(b, \bar{d}; t, \bar{u}, g) \tag{4.25}$$

are what we want; as a consequence, the $\mathcal{S}$ functions have still the forms given in eqs. (4.19) and (4.20). For the process in eqn. (4.7), see fig. 4.3, we noted that in the cases of s- and t-channel contributions the singularities arise from the splittings $g \to d\bar{d}$ and $g \to b\bar{b}$ respectively. Therefore, we assign momenta as follows

$$(u, g; t, \bar{b}, d) \qquad s-\text{channel}, \tag{4.26}$$
$$(u, g; t, d, \bar{b}) \qquad t-\text{channel}, \tag{4.27}$$

and analogously for process (4.8)

$$(\bar{d}, g; t, \bar{b}, \bar{u}) \qquad s-\text{channel}, \tag{4.28}$$
$$(\bar{d}, g; t, \bar{u}, \bar{b}) \qquad t-\text{channel}. \tag{4.29}$$

Finally, owing to the fact that $\mathcal{S}_2^{(0)} \leftrightarrow \mathcal{S}_3^{(0)}$ when $k_2 \leftrightarrow k_3$, we write

$$\begin{aligned} \mathcal{M}^{(r)}(b, g; t, d, \bar{u}) &= \mathcal{S}_3^{(0)} \mathcal{M}^{(r)}(b, g; t, d, \bar{u}) + \mathcal{S}_2^{(0)} \mathcal{M}^{(r)}(b, g; t, d, \bar{u}) \\ &= \mathcal{S}_3^{(0)} \Big[\mathcal{M}^{(r)}(b, g; t, d, \bar{u}) + \mathcal{M}^{(r)}(b, g; t, \bar{u}, d) \Big]. \end{aligned} \tag{4.30}$$

In other words, we shall assign the momenta in process (4.9) in two different ways

$$(b, g; t, d, \bar{u}) \,, \tag{4.31}$$
$$(b, g; t, \bar{u}, d) \,, \tag{4.32}$$

and for each of them we multiply the corresponding matrix element times $\mathcal{S}_3^{(0)}$ given in eqn. (4.22); as shown in eqn. (4.30), this is fully equivalent to eqs. (4.21)–(4.23).

As a final remark, we note that when keeping the same ordered notation (4.17) after charge conjugation the treatment of real emission corrections to anti-top production is perfectly analogous, and the inclusion of single-$\bar{t}$ requires no extra work.

4.1.2 MC cross sections expanded to NLO

As discussed in **I** and **II**, in order to construct the MC subtraction terms one needs the cross section obtained by keeping the first non-trivial order in the α_s expansion of the parton shower Monte Carlo that will be matched with the NLO computation. The explicit results presented here are relevant to HERWIG. The most general form of the MC cross sections is given in eqn. (**II**.5.1), which we rewrite as follows

$$d\sigma\Big|_{\rm MC} = \sum_{\mu}\sum_{L}\sum_{l} d\sigma_{\mu}^{(L,l)}\Big|_{\rm MC}\,, \tag{4.33}$$

where the index μ generically indicates a collection of labels which unambiguously identify the $2\to 3$ partonic subprocess. The index L assumes the values $+$, $-$, f_1, and f_2 (the latter two were denoted by Q and $\bar{Q}$ in **II**). The index l, which differs per colour structure, assumes the values q_iq_j, where q_i and q_j are the four-momenta of the colour partners relevant to the emission considered; in this way, the shower scale is

$$E_0^2 = |l| \equiv |q_i\cdot q_j|. \tag{4.34}$$

In **II** we had $l = s,t,u$ (and $E_0^2 = |l|/2$), but in the case of unequal masses this is not a convenient notation. Equations (**II**.5.2)–(**II**.5.5) are also unchanged apart from notation

$$d\sigma_{\mu}^{(+,l)}\Big|_{\rm MC} = \frac{1}{z_+^{(l)}} f_a^{(H_1)}(\bar{x}_{1i}/z_+^{(l)}) f_b^{(H_2)}(\bar{x}_{2i})\, d\hat{\sigma}_{\mu}^{(+,l)}\Big|_{\rm MC} d\bar{x}_{1i}\, d\bar{x}_{2i}\,, \tag{4.35}$$

$$d\sigma_{\mu}^{(-,l)}\Big|_{\rm MC} = \frac{1}{z_-^{(l)}} f_a^{(H_1)}(\bar{x}_{1i}) f_b^{(H_2)}(\bar{x}_{2i}/z_-^{(l)})\, d\hat{\sigma}_{\mu}^{(-,l)}\Big|_{\rm MC} d\bar{x}_{1i}\, d\bar{x}_{2i}\,, \tag{4.36}$$

$$d\sigma_{\mu}^{(f_1,l)}\Big|_{\rm MC} = f_a^{(H_1)}(\bar{x}_{1f}) f_b^{(H_2)}(\bar{x}_{2f})\, d\hat{\sigma}_{\mu}^{(f_1,l)}\Big|_{\rm MC} d\bar{x}_{1f}\, d\bar{x}_{2f}\,, \tag{4.37}$$

$$d\sigma_{\mu}^{(f_2,l)}\Big|_{\rm MC} = f_a^{(H_1)}(\bar{x}_{1f}) f_b^{(H_2)}(\bar{x}_{2f})\, d\hat{\sigma}_{\mu}^{(f_2,l)}\Big|_{\rm MC} d\bar{x}_{1f}\, d\bar{x}_{2f}\,, \tag{4.38}$$

where the flavours a and b of the incoming partons depend on the value of μ. The short-distance cross sections that appear on the r.h.s. of eqs. (4.35)–(4.38) can be read from eqn. (**II**.5.6) and eqn. (**II**.5.8)

$$d\hat{\sigma}_{\mu}^{(\pm,l)}\Big|_{\rm MC} = \frac{\alpha_s}{2\pi}\frac{d\xi_{\pm}^{(l)}}{\xi_{\pm}^{(l)}} dz_{\pm}^{(l)} P^{(0)}_{a'b'}(z_{\pm}^{(l)})\, d\bar{\sigma}_{\mu'}\Theta\left((z_{\pm}^{(l)})^2 - \xi_{\pm}^{(l)}\right), \tag{4.39}$$

$$d\hat{\sigma}_{\mu}^{(f_\alpha,l)}\Big|_{\rm MC} = \frac{\alpha_s}{2\pi}\frac{d\xi_{f_\alpha}^{(l)}}{\xi_{f_\alpha}^{(l)}} dz_{f_\alpha}^{(l)} P^{(0)}_{a'b'}(z_{f_\alpha}^{(l)})\, d\bar{\sigma}_{\mu'}\Theta\left(1-\xi_{f_\alpha}^{(l)}\right)\Theta\left(z_{f_\alpha}^{(l)} - \frac{m_\alpha}{E_0\sqrt{\xi_{f_\alpha}^{(l)}}}\right), \tag{4.40}$$

where the Θ's account for HERWIG dead regions (see sect. 4.3 of **II**), and the flavours a', b', and the values of μ' can be determined by considering the possible collinear splittings of the corresponding NLO tree-level processes.

	$(u,d;t,b)$	$(d,u;t,b)$
$(u,d;t,b,g)$	$\pm(\mathbf{p}_1\cdot\mathbf{p}_2);\, f_{1,2}(\mathbf{k}_1\cdot\mathbf{k}_2)$	
$(d,u;t,b,g)$		$\pm(\mathbf{p}_1\cdot\mathbf{p}_2);\, f_{1,2}(\mathbf{k}_1\cdot\mathbf{k}_2)$
$(u,g;t,b,d)$	$-(\mathbf{p}_1\cdot\mathbf{p}_2)$	
$(\bar{d},g;t,\bar{b},\bar{u})$		$-(\mathbf{p}_1\cdot\mathbf{p}_2)$
$(g,u;t,b,d)$		$+(\mathbf{p}_1\cdot\mathbf{p}_2)$
$(g,d;t,b,\bar{u})$	$+(\mathbf{p}_1\cdot\mathbf{p}_2)$	

Table 4.1: Short-distance contributions to MC subtraction terms, for the s-channel. The two columns correspond to the two possible s-channel Born cross sections, distinguished by the direction of the incoming partons. For a given process, the entries show the emitting legs, and in round brackets the value of the shower scale E_0 (up to a sign), according to the possible colour flows.

	$(b,u;t,d)$	$(b,d;t,\bar{u})$
$(b,u;t,d,g)$	$+, f_1(\mathbf{p}_1\cdot\mathbf{k}_1);\, -, f_2(\mathbf{p}_2\cdot\mathbf{k}_2)$	
$(b,\bar{d};t,\bar{u},g)$		$+, f_1(\mathbf{p}_1\cdot\mathbf{k}_1);\, -, f_2(\mathbf{p}_2\cdot\mathbf{k}_2)$
$(b,g;t,d,\bar{u})$	$-(\mathbf{p}_2\cdot\mathbf{k}_2)$	
$(g,u;t,d,b)$	$+(\mathbf{p}_1\cdot\mathbf{k}_1)$	
$(b,g;t,\bar{u},d)$		$-(\mathbf{p}_2\cdot\mathbf{k}_2)$
$(g,d;t,\bar{u},b)$		$+(\mathbf{p}_1\cdot\mathbf{k}_1)$

Table 4.2: As in table 4.1, for the t-channel, with bu- and $b\bar{d}$-initiated Born processes.

As in **II**, we use unbarred and barred symbols to denote quantities relevant to $2\to3$ and $2\to2$ processes respectively. The momentum assignments for the former are given in eqn. (4.16), while for the latter we use

$$\alpha'(\mathbf{p}_1)+\beta'(\mathbf{p}_2)\;\longrightarrow\; t(\mathbf{k}_1)+\gamma'(\mathbf{k}_2)\,, \tag{4.41}$$

which we shorten in a way similar to eqn. (4.17)

$$(\alpha',\beta';t,\gamma')\,. \tag{4.42}$$

In MC cross sections expanded to NLO, $2\to2$ momenta (entering $d\bar{\sigma}$ on the r.h.s. of eqs. (4.39) and (4.40)) are obtained by means of a suitable projection of the corresponding $2\to3$ momenta. The exact form of the projection is specific to the parton shower MC matched to the NLO computation, and for HERWIG can be worked out as was done in **II**. Here, we need to extend the formulae given in **II**, in

	$(u,b;t,d)$	$(d,b;t,\bar{u})$
$(u,b;t,d,g)$	$+, f_2(\mathbf{p}_1\cdot\mathbf{k}_2);\ -, f_1(\mathbf{p}_2\cdot\mathbf{k}_1)$	
$(d,b;t,\bar{u},g)$		$+, f_2(\mathbf{p}_1\cdot\mathbf{k}_2);\ -, f_1(\mathbf{p}_2\cdot\mathbf{k}_1)$
$(u,g;t,d,b)$	$-(\mathbf{p}_2\cdot\mathbf{k}_1)$	
$(g,b;t,d,\bar{u})$	$+(\mathbf{p}_1\cdot\mathbf{k}_2)$	
$(d,g;t,\bar{u},b)$		$-(\mathbf{p}_2\cdot\mathbf{k}_1)$
$(g,b;t,\bar{u},d)$		$+(\mathbf{p}_1\cdot\mathbf{k}_2)$

Table 4.3: As in table 4.1, for the t-channel, with ub- and $\bar{d}b$-initiated Born processes.

order to treat the case of final-state partons with unequal masses; explicit results are given in appendix B.

As far as flavour combinations are concerned, it is simpler to read eqs. (4.39) and (4.40) from right to left, since this follows the logic which forms the basis of a parton shower. The MC starts with a Born-level ($2\to 2$ for single-t production) process, and then lets each leg branch in all kinematically- and flavour-allowed configurations possible. This implies that several $2\to 3$ processes may be generated starting from a given $2\to 2$ process. We list all such processes explicitly in tables 4.1–4.3; the non-void entries give non-zero contributions to eqn. (4.33). Thus, the index μ that classifies the $2\to 3$ partonic processes can simply be chosen so as to count all of the quantities that appear in the first columns of the tables. Parton legs where the branchings occur are denoted by $+$, $-$, f_1, and f_2 (f_1 always coincides with the top quark); given the parton that branches, and the hard subprocess, a colour connection is established which fixes the shower scale E_0 unambiguously. The shower scales to be used in eqs. (4.39) and (4.40) are equal to the absolute values of the dot products listed in tables 4.1–4.3. We finally point out that the momentum assignments for the $2\to 3$ processes in the tables above are the same as those adopted (after relabeling) in the context of the pure NLO computation. This puts the NLO and MC cross sections on the same footing from a notational viewpoint, which will be convenient for the formal manipulations to be carried out in the next section.

4.2 MC@NLO

The definition of the MC@NLO formalism is given in eqn. (**I**.4.22) or eqn. (**II**.2.1):

$$\begin{aligned}\mathcal{F}_{\text{MC@NLO}} = \sum_{\mu} \int dx_1 dx_2 d\phi_3 \Bigg\{ & \mathcal{F}^{(3)}_{\text{MC}} \left(\left. \frac{d\overline{\Sigma}^{(f)}_{\mu}}{d\phi_3} \right|_{\text{ev}} - \left. \frac{d\overline{\Sigma}_{\mu}}{d\phi_3} \right|_{\text{MC}} \right) \\ & + \mathcal{F}^{(2)}_{\text{MC}} \Bigg[- \left. \frac{d\overline{\Sigma}^{(f)}_{\mu}}{d\phi_3} \right|_{\text{ct}} + \left. \frac{d\overline{\Sigma}_{\mu}}{d\phi_3} \right|_{\text{MC}} + \frac{1}{\mathcal{I}_2} \left(\frac{d\overline{\Sigma}^{(b)}_{\mu}}{d\phi_2} + \frac{d\overline{\Sigma}^{(sv)}_{\mu}}{d\phi_2} \right) \\ & + \frac{1}{\mathcal{I}_{\tilde{2}}} \left(\left. \frac{d\overline{\Sigma}^{(c+)}_{\mu}}{d\phi_2 dx} \right|_{\text{ev}} + \left. \frac{d\overline{\Sigma}^{(c-)}_{\mu}}{d\phi_2 dx} \right|_{\text{ev}} \right) - \frac{1}{\mathcal{I}_{\tilde{2}}} \left(\left. \frac{d\overline{\Sigma}^{(c+)}_{\mu}}{d\phi_2 dx} \right|_{\text{ct}} + \left. \frac{d\overline{\Sigma}^{(c-)}_{\mu}}{d\phi_2 dx} \right|_{\text{ct}} \right) \Bigg] \Bigg\}. \end{aligned} \tag{4.43}$$

There is a minor difference of notation with respect to eqn. (**II**.2.1): the indices for the sum over all partonic processes are denoted here by μ, consistently with what was done in sect. 4.1.2. We refer the reader to **I** and **II** for all details relevant to the formalism. Single-t production is the first process implemented in MC@NLO in which *both* $\mathcal{S}^{(0)}_i$ and $\mathcal{S}^{(1)}_{ij}$ are non-zero for certain i and j. This has direct implications for eqn. (4.43), which we now discuss.

As shown in sect. 4.1.2, for a given choice of the index μ which classifies the partonic processes the radiation pattern in the MC cross section is determined by the values of the indices L and l. On the other hand, the possible radiation patterns at the NLO level are determined by the $\mathcal{S}^{(0)}_i$ and $\mathcal{S}^{(1)}_{ij}$ functions. Inspection of sect. 4.1.1 and of tables 4.1–4.3 shows that, for a given μ, there are *at most* one $\mathcal{S}^{(0)}$ and one $\mathcal{S}^{(1)}$ functions which are non-vanishing. Formally, this corresponds to defining two single-valued functions $i(\mu)$ and $j(\mu)$ such that $\mathcal{S}^{(0)}_{i(\mu)}$ and $\mathcal{S}^{(1)}_{i(\mu)j(\mu)}$ may be different from zero. This allows us to define the following quantities

$$\mathcal{S}^{(\text{IN})}_{\mu} = \mathcal{S}^{(0)}_{i(\mu)} \,, \qquad \mathcal{S}^{(\text{OUT})}_{\mu} = \mathcal{S}^{(1)}_{i(\mu)j(\mu)} \,, \tag{4.44}$$

where the labels IN and OUT are to remind us that $\mathcal{S}^{(0)}_i$ and $\mathcal{S}^{(1)}_{ij}$ select kinematics configurations relevant to initial- and final-state collinear emissions respectively. Note that one of the functions in eqn. (4.44) may be still be vanishing (which is the case for $\mathcal{S}^{(1)}$ in processes (4.31) and (4.32)), but there cannot be other non-vanishing $\mathcal{S}$ functions. In any case, from eqs. (4.44) and (4.10) we obtain

$$\mathcal{S}^{(\text{IN})}_{\mu} + \mathcal{S}^{(\text{OUT})}_{\mu} = 1 \qquad \forall\, \mu \,. \tag{4.45}$$

Note that, since we have exploited relabeling invariance to assign the four-momentum k_3 always to the FKS parton, we have $i(\mu) \equiv 3$. Furthermore, since the other massless final-state parton has four-momentum k_2, we also have $j(\mu) \equiv 2$. However,

eqn. (4.44) holds independently of relabeling invariance. Furthermore, it is clear that an analogous equation must hold for any kind of hard reaction, and not only for single-t production, as a direct consequence of the definition of the FKS partition.

The term $\overline{\Sigma}^{(f)}$ is proportional to the real-emission matrix elements (see eqn. (**I**.4.12) and eqn. (**I**.4.13)); thus, according to eqn. (4.11), in eqn. (4.43) we understand

$$\frac{d\overline{\Sigma}^{(f)}_{\mu}}{d\phi_3} = \mathcal{S}^{(\mathrm{IN})}_{\mu}\frac{d\overline{\Sigma}^{(f)}_{\mu}}{d\phi_3} + \mathcal{S}^{(\mathrm{OUT})}_{\mu}\frac{d\overline{\Sigma}^{(f)}_{\mu}}{d\phi_3} \tag{4.46}$$

$$= \mathcal{S}^{(\mathrm{IN})}_{\mu}\frac{d\overline{\Sigma}^{(f)}_{\mu}}{d\phi_3^{(\mathrm{IN})}} + \mathcal{S}^{(\mathrm{OUT})}_{\mu}\frac{d\overline{\Sigma}^{(f)}_{\mu}}{d\phi_3^{(\mathrm{OUT})}}\,, \tag{4.47}$$

where we have introduced two different *parametrizations* ($d\phi_3^{(\mathrm{IN})}$ and $d\phi_3^{(\mathrm{OUT})}$) of the three-body phase space $d\phi_3$, analogously to what is done in FKS in the context of pure NLO computations (see sect. 4.1.1). Their explicit forms, which are irrelevant in what follows, will be given in app. C.

In eqn. (4.43) each point (x_1, x_2, ϕ_3) corresponds to a $2 \to 3$ kinematic configuration (called $\mathbb{H}$). In previous MC@NLO implementations, a definite $2 \to 2$ configuration (called $\mathbb{S}$) was chosen given (x_1, x_2, ϕ_3), according to a mapping $\mathcal{P}_{\mathbb{H}\to\mathbb{S}}$ whose form is dictated by HERWIG. The definition of such an unique mapping requires elaborate manipulations of the MC subtraction terms since, as shown in eqn. (**II**.B.32) and eqn. (**II**.B.33), initial- and final-state emissions would naturally lead to the definitions of two different mappings $\mathcal{P}^{(\mathrm{IN})}_{\mathbb{H}\to\mathbb{S}}$ and $\mathcal{P}^{(\mathrm{OUT})}_{\mathbb{H}\to\mathbb{S}}$. Following the same arguments as in app. B of **II**, we could implement single-t production using an unique $\mathcal{P}_{\mathbb{H}\to\mathbb{S}}$; as discussed there, however, this may degrade the numerical accuracy in the integration step and the unweighting efficiency. Furthermore, the two mappings $\mathcal{P}^{(\mathrm{IN})}_{\mathbb{H}\to\mathbb{S}}$ and $\mathcal{P}^{(\mathrm{OUT})}_{\mathbb{H}\to\mathbb{S}}$ are a perfect match to the FKS phase-space partition, which enters eqn. (4.43) through eqn. (4.47); the mapping $\mathcal{P}^{(\mathrm{IN})}_{\mathbb{H}\to\mathbb{S}}$ ($\mathcal{P}^{(\mathrm{OUT})}_{\mathbb{H}\to\mathbb{S}}$) can be naturally expressed in terms of the variables of $d\phi_3^{(\mathrm{IN})}$ ($d\phi_3^{(\mathrm{OUT})}$). In practice,

we replace eqn. (**I**.4.23) and eqn. (**I**.4.24) with the following pairs of equations

$$I_{\mathbb{H}}^{(\mathrm{IN})} = \sum_{\mu} \int dx_1 dx_2 d\phi_3^{(\mathrm{IN})} \left(\mathcal{S}_{\mu}^{(\mathrm{IN})} \frac{d\overline{\Sigma}_{\mu}^{(f)}}{d\phi_3^{(\mathrm{IN})}} \right|_{\mathrm{ev}} - \left. \frac{d\overline{\Sigma}_{\mu}^{(L=\pm)}}{d\phi_3^{(\mathrm{IN})}} \right|_{\mathrm{MC}} \Bigg), \tag{4.48}$$

$$\begin{aligned} I_{\mathbb{S}}^{(\mathrm{IN})} = \sum_{\mu} \int dx_1 dx_2 d\phi_3^{(\mathrm{IN})} \Bigg[& - \mathcal{S}_{\mu}^{(\mathrm{IN})} \frac{d\overline{\Sigma}_{\mu}^{(f)}}{d\phi_3^{(\mathrm{IN})}} \Bigg|_{\mathrm{ct}} + \left. \frac{d\overline{\Sigma}_{\mu}^{(L=\pm)}}{d\phi_3^{(\mathrm{IN})}} \right|_{\mathrm{MC}} \\ & + \frac{\mathcal{S}_{\mu}^{(\mathrm{IN})}}{\mathcal{I}_2} \left(\frac{d\overline{\Sigma}_{\mu}^{(b)}}{d\phi_2^{(\mathrm{IN})}} + \frac{d\overline{\Sigma}_{\mu}^{(sv)}}{d\phi_2^{(\mathrm{IN})}} \right) + \frac{1}{\mathcal{I}_{\tilde{2}}} \left(\left. \frac{d\overline{\Sigma}_{\mu}^{(c+)}}{d\phi_2^{(\mathrm{IN})} dx} \right|_{\mathrm{ev}} + \left. \frac{d\overline{\Sigma}_{\mu}^{(c-)}}{d\phi_2^{(\mathrm{IN})} dx} \right|_{\mathrm{ev}} \right) \\ & - \frac{1}{\mathcal{I}_{\tilde{2}}} \left(\left. \frac{d\overline{\Sigma}_{\mu}^{(c+)}}{d\phi_2^{(\mathrm{IN})} dx} \right|_{\mathrm{ct}} + \left. \frac{d\overline{\Sigma}_{\mu}^{(c-)}}{d\phi_2^{(\mathrm{IN})} dx} \right|_{\mathrm{ct}} \right) \Bigg], \end{aligned} \tag{4.49}$$

and

$$I_{\mathbb{H}}^{(\mathrm{OUT})} = \sum_{\mu} \int dx_1 dx_2 d\phi_3^{(\mathrm{OUT})} \left(\mathcal{S}_{\mu}^{(\mathrm{OUT})} \frac{d\overline{\Sigma}_{\mu}^{(f)}}{d\phi_3^{(\mathrm{OUT})}} \right|_{\mathrm{ev}} - \left. \frac{d\overline{\Sigma}_{\mu}^{(L=f_{1,2})}}{d\phi_3^{(\mathrm{OUT})}} \right|_{\mathrm{MC}} \Bigg), \tag{4.50}$$

$$\begin{aligned} I_{\mathbb{S}}^{(\mathrm{OUT})} = \sum_{\mu} \int dx_1 dx_2 d\phi_3^{(\mathrm{OUT})} \Bigg[& - \mathcal{S}_{\mu}^{(\mathrm{OUT})} \frac{d\overline{\Sigma}_{\mu}^{(f)}}{d\phi_3^{(\mathrm{OUT})}} \Bigg|_{\mathrm{ct}} + \left. \frac{d\overline{\Sigma}_{\mu}^{(L=f_{1,2})}}{d\phi_3^{(\mathrm{OUT})}} \right|_{\mathrm{MC}} \\ & + \frac{\mathcal{S}_{\mu}^{(\mathrm{OUT})}}{\mathcal{I}_2} \left(\frac{d\overline{\Sigma}_{\mu}^{(b)}}{d\phi_2^{(\mathrm{OUT})}} + \frac{d\overline{\Sigma}_{\mu}^{(sv)}}{d\phi_2^{(\mathrm{OUT})}} \right) \Bigg], \end{aligned} \tag{4.51}$$

in such a way that the total rate is now

$$\sigma_{tot} = I_{\mathbb{S}}^{(\mathrm{IN})} + I_{\mathbb{H}}^{(\mathrm{IN})} + I_{\mathbb{S}}^{(\mathrm{OUT})} + I_{\mathbb{H}}^{(\mathrm{OUT})}, \tag{4.52}$$

which replaces eqn. (**I**.4.25). It should be clear that eqs. (4.48)–(4.51) are a direct consequence of the definition of MC@NLO: in fact, eqn. (4.43) is recovered by inserting $\mathcal{F}_{\mathrm{MC}}^{(3)}$ on the r.h.s. of eqs. (4.48) and (4.50), and $\mathcal{F}_{\mathrm{MC}}^{(2)}$ on the r.h.s. of eqs. (4.49) and (4.51). We note that the Born ($\overline{\Sigma}^{(b)}$) and the soft-virtual ($\overline{\Sigma}^{(sv)}$) contributions have been manipulated similarly to what was done for the real-emission contribution in eqn. (4.47); although strictly speaking this is not necessary, since these terms are finite and therefore not involved in any subtraction, it helps to improve the numerical evaluations of the integrals $I_{\mathbb{S}}^{(\mathrm{IN})}$ and $I_{\mathbb{S}}^{(\mathrm{OUT})}$. On the other hand, the remainders of the initial-state collinear subtraction ($\overline{\Sigma}^{(c\pm)}$) only appear in $I_{\mathbb{S}}^{(\mathrm{IN})}$, since $I_{\mathbb{S}}^{(\mathrm{OUT})}$ is associated with final-state emissions. We have also introduced two two-body phase-space parametrizations $d\phi_2^{(\mathrm{IN})}$ and $d\phi_2^{(\mathrm{OUT})}$, which are

analogous to their three-body counterparts. Finally, we have introduced the notation

$$\overline{\Sigma}_\mu\Big|_{\rm MC} = \overline{\Sigma}_\mu^{(L=\pm)}\Big|_{\rm MC} + \overline{\Sigma}_\mu^{(L=f_{1,2})}\Big|_{\rm MC}\,, \tag{4.53}$$

which is the analogue of eqn. (4.47) for MC subtraction terms. The first and second terms on the r.h.s. of eqn. (4.53) receive contributions from eqn. (4.39) and (4.40) respectively (i.e. from initial-state and final-state branchings). Taking into account the properties of the MC subtraction terms (see app. C), this implies that eqs. (4.48)–(4.51) are finite; in fact, final-state singularities of real-emission matrix elements and their corresponding counterterms are removed in eqs. (4.48) and (4.49) by $\mathcal{S}^{(\rm IN)}$, while initial-state singularities are removed in eqs. (4.50) and (4.51) by $\mathcal{S}^{(\rm OUT)}$. Thus, the same procedure as in sect. 4.5 of **I** can be used in order to generate the hard events that are given to the parton shower as initial conditions.

As a concluding remark, we point out that the reason why the subtraction formalism of refs. [17, 18] appears to be particularly well suited for MC@NLO implementations can be read from eqs. (4.48)–(4.51). The partition of the phase space into collinear-like singular regions gives the FKS parton the same role as the softest parton emitted by an MC in the first branching after the generation of the hard process. Since as explained in **I** and **II** the first branching is the only one that matters for matching the MC with an NLO computation, the FKS parton and the softest parton emerging from the first branching in the shower are naturally paired in the definition of MC@NLO. Apart from guaranteeing the local cancellation of IR singularities, such pairing also allows a good control on the numerical stability of the result. It is also important to recall that, in each of the IR singular regions defined by the FKS partition, there are no unnecessary NLO subtractions: the only counterterm contributing to the result is that relevant to the real matrix element singularity present in that given region. This fact is very beneficial in reducing the number of negative-weight events.

4.3 Results

In this section we present sample results for single-t production at the Tevatron with $\sqrt{S} = 1.96$ TeV. We limit ourselves here to comparing MC@NLO predictions with those obtained with HERWIG and with an NLO code we have written according to the subtraction method of refs. [17, 18], as discussed in sect. 4.1.1. As a preliminary step, we have checked that our NLO results (with $\mu_{\rm R} = \mu_{\rm F} = m_t$) for the total rate and various t and $\bar{t}$ distributions are in excellent agreement with those of MCFM [9]. All of the predictions given in this section have been obtained by using the MRST2002 default PDF set [19], and by setting $m_t = 178$ GeV, which

result in total rates equal to 1.045 pb and 0.406 pb for t- and s-channel respectively. We have rescaled HERWIG results to the NLO cross section, since we are only interested in the comparison of shapes in the case of standard MC's. Also, we have only considered here HERWIG results for the t-channel contribution. All the MC@NLO and HERWIG results (but not, of course, the NLO ones) include the hadronization of the partons in the final state; furthermore, we forced the W emerging from the top decay to decay into a pair of leptons. In order to reduce as much as possible the statistical errors, we have generated $5 \cdot 10^5$ events for each MC@NLO and HERWIG run[5]. Finally, we stress that all of the fixed-order predictions presented here will be denoted as having NLO accuracy, even in the case of observables which, in the sense of perturbation theory, are effectively of leading order (see e.g. $p_{\rm T}^{(tj)}$ below); this is consistent with the terminology one *needs* to adopt in the context of MC@NLO (sect. 2.3 of **I**).

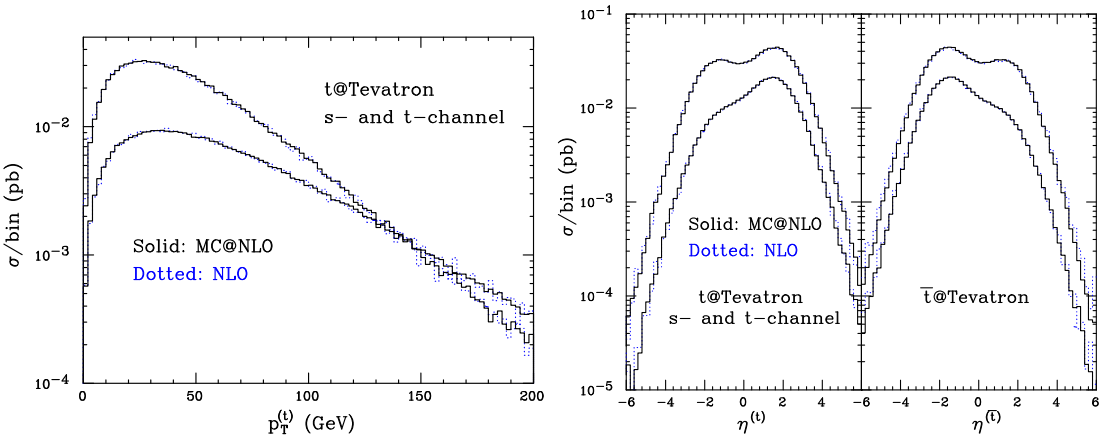

Figure 4.5: Comparison of MC@NLO (solid) and NLO (dotted) results. Left pane: top $p_{\rm T}$, for t-channel (higher peak) and s-channel (lower peak) contributions. We have checked that $p_{\rm T}^{(t)} = p_{\rm T}^{(\bar{t})}$. Right pane: top (left) and antitop (right) η, for t-channel (higher curves) and s-channel (lower curves) contributions.

We start by considering the transverse momentum and pseudorapidity of the top and antitop (see fig. 4.5). We expect the impact of the momentum reshuffling that takes place during the hadronization phase in MC@NLO to be negligible on such observables. We also expect these observables, being sufficiently inclusive, to be reliably predicted by pure-NLO computations. As we see from the figure, the good agreement between MC@NLO and NLO confirms our expectations, and

[5]Clearly, we are not suggesting to collect an integrated luminosity of $\mathcal{O}(1)$ ab^{-1} at the Tevatron. Here, we simply aim to expose the features of the two MC simulations with some precision.

suggests that NNLO effects should be small. We have found that the HERWIG results are extremely close to the MC@NLO ones, and for this reason are not shown on the plots. As for all other processes previously studied, we have observed a much-improved behaviour from the numerical point of view when going from NLO to MC@NLO predictions, which is due to the fact that in MC@NLO all cancellations between large numbers occur at the level of short-distance cross sections, rather than in histograms as in the case of NLO computations. It is reassuring to see that this property holds true also for single-t production, which is the most involved process treated so far because of the simultaneous presence of initial- and final-state collinear singularities.

We now discuss the properties of a few jet observables. For the sake of clarity, we limit ourselves in this discussion to considering t-channel top events. We reconstruct the jets by means of the $k_{\rm T}$-clustering algorithm [20], with $d_{cut} = 100$ GeV^2. We include in the clustering procedure all final-state stable hadrons[6] and photons. After the jets are reconstructed, we throw away the one that contains the b-flavoured hadron whose parent parton is the b quark emerging from top decay, and order the remaining ones in transverse energy, i.e. the hardest jet is the one with the largest $E_{\rm T}$.

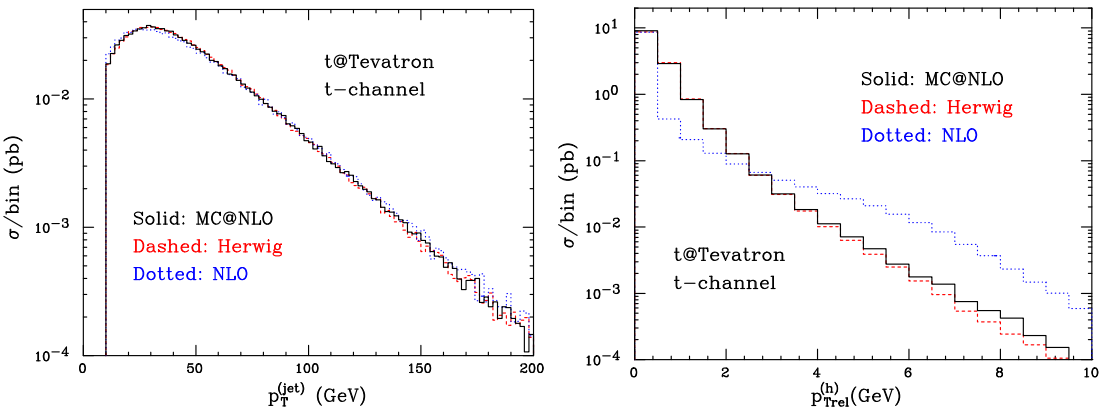

Figure 4.6: MC@NLO (solid), HERWIG (dashed), and NLO (dotted) results, for the $p_{\rm T}$ of the hardest jet (left pane), and the $p_{\rm T}$ relative to the axis of the hardest jet of those hadrons or partons in that jet (right pane).

We recall that we do not let the top decay in our pure-NLO computation. Also, we expect that some of the partons resulting from the radiation by the b quark emerging from the top decay in MC@NLO and HERWIG will hadronize into

[6]For the sake of simplicity, we force π^0's and all lowest-lying b-flavoured states to be stable in HERWIG.

hadrons that are not clustered into the b-jet which we throw away. Furthermore, some extra radiation will occur from the top line due to showering, which is not included in the NLO computation. Finally, those jets obtained with MC@NLO and HERWIG are at the hadron level, while those obtained with the NLO computation are at the parton level.

In spite of these differences, there is a good agreement between MC@NLO, HERWIG, and NLO for the $p_{\rm T}$ of the hardest jet, shown in the left pane of fig. 4.6. This observable is sufficiently inclusive for this to happen, and the small differences between MC@NLO and NLO at small $p_{\rm T}$ are mainly due to the hadronization phase. On the other hand, the internal structure of the jet is very different in MC@NLO and HERWIG from that resulting from the NLO computation. In the right pane of fig. 4.6 we present the transverse momentum, relative to the axis of the jet, of all of the hadrons or partons clustered into the jet itself. At the NLO, the jet often coincides with a single parton, hence the sharp peak at $p_{\rm Trel}^{(h)} = 0$. Such a peak is much less pronounced in the case of the MC's, since in those cases the jet almost never coincides with a single hadron. On the other hand, at large $p_{\rm Trel}^{(h)}$ the MC results are smaller than the NLO one: this must be so, since in the final states obtained with MC simulations it is likely that a large-$p_{\rm Trel}^{(h)}$ hadron will be clustered into another jet. This is much less probable at the NLO, simply because the number of jets there is limited to two. It is also interesting to observe that, although very small, the effect of the hard emissions due to the NLO real matrix elements is visible in the tail of the $p_{\rm Trel}^{(h)}$ distribution, the MC@NLO result being slightly harder than the HERWIG one.

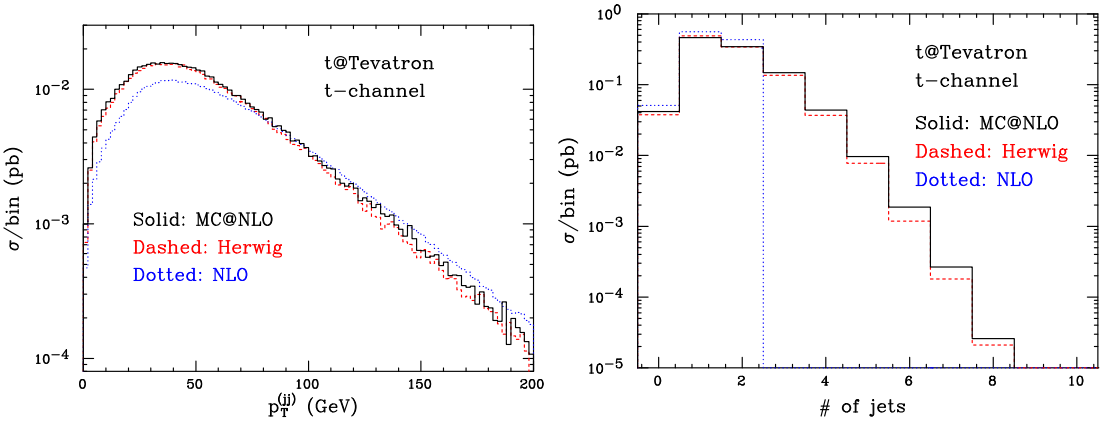

Figure 4.7: As in fig. 4.6, for the $p_{\rm T}$ of the two-hardest-jet pair (left pane), and for the number of jets (right pane).

The differences between the topologies of the final states emerging from NLO

computations and MC@NLO and HERWIG simulations are clearly visible when we consider observables less inclusive than the $p_{\rm T}$ of the hardest jet. In the left pane of fig. 4.7 we plot the $p_{\rm T}$ of the pair of the two hardest jets. As is clear from the fact that MC@NLO and HERWIG have very similar shapes, which are different from the NLO one, the real matrix elements play a minor role here compared to the multiple emissions of the shower. The effects of the real matrix elements are more clearly visible in the tail of the distribution in the number of final-state jets (right pane of fig. 4.7), with MC@NLO predicting more events with more than two jets compared to HERWIG.

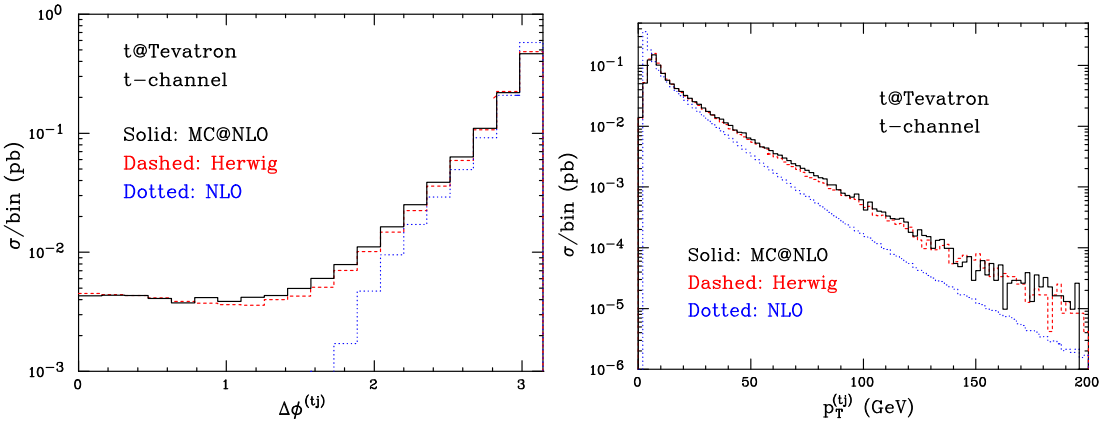

Figure 4.8: As in fig. 4.6, for the azimuthal difference between (left pane), and the $p_{\rm T}$ of (right pane) the top-hardest jet pair.

It is also interesting to observe that shower effects dominate over matrix element ones for top-hardest jet correlations, two of which we present in fig. 4.8. We stress again here that we did not make any systematic attempt to exclude from the jet clustering the partons radiated by the top and its decay products, which would allow a closer matching between MC's and NLO results for these correlations. This is very clearly shown by the left pane of fig. 4.8, which presents the difference in azimuth between the top and the hardest jet. While the NLO prediction is zero for $\Delta\phi^{(tj)} < \pi/2$ for kinematics reasons (there is nothing in this region for the top-hardest jet pair to recoil against), MC@NLO and HERWIG feature a long tail which extends down to $\Delta\phi^{(tj)} = 0$. This is in part due to the fact that the top tends to have a much larger longitudinal than transverse momentum component. Thus, it is relatively easy for a parton, radiated by the top quark shower, to change the top transverse momentum by a sizable amount. The $\Delta\phi^{(tj)} = 0$ tail is mainly populated by such low-$p_{\rm T}^{(t)}$ events. In the right pane of fig. 4.8 we present the $p_{\rm T}$ of the top-hardest jet pair. At the NLO level, only $2 \to 3$ processes can contribute

to the region $p_{\rm T}^{(tj)} \neq 0$, in the configurations in which the two final-state massless partons are not combined into a single jet; for this to happen, the two partons must be well separated. Clearly, such configurations imply the presence of a very off-shell intermediate particle, and are thus disfavoured by matrix elements: the $p_{\rm T}^{(tj)}$ distribution is steeply falling. In MC@NLO and HERWIG, $2 \to 3$ configurations result from a $2 \to 2$ hard process followed by a parton branching[7]. Since the branching is collinear in nature, the probability of getting two well-separated partons is even smaller than in NLO computations. However, the shower usually does not stop after the first branching. Furthermore, all strongly-interacting particles, including the top and the b emerging from the top decay, can radiate. This smears very effectively the final-state momenta; we have verified that, in the large-$p_{\rm T}^{(tj)}$ region, the hardest jet may retain a fraction of the parent parton momentum as small as 50%. This creates an imbalance between the top and the hardest-jet $p_{\rm T}$ which results in the much harder $p_{\rm T}^{(tj)}$ tails in MC@NLO and HERWIG relative to the NLO result. It should be stressed that such an effect is magnified by the steepness of the $p_{\rm T}^{(tj)}$ distribution. In terms of the total number of events, this is still a marginal phenomenon, which gives a negligible contribution to observables such as the inclusive $p_{\rm T}$ of the hardest jet. We conclude by observing again that the real matrix elements contributions are small but visible in the differences between MC@NLO and HERWIG in the intermediate $\Delta\phi^{(tj)}$ and large-$p_{\rm T}^{(tj)}$ regions.

The results presented so far have shown little or no difference between MC@NLO and HERWIG results as far as shapes are concerned. Although larger differences could be seen by imposing hard transverse momentum cuts, the fact remains that at the Tevatron the phase-space for hard radiation is fairly limited. There are, however, observables that are particularly sensitive to real matrix element effects, such as the transverse momentum of the b-flavoured hadrons[8], which we present in fig. 4.9. This is because in t-channel matrix elements a b quark is almost always present in the initial state (up to CKM-suppressed contributions). This results in a final-state b-flavoured hadron which, in the case of HERWIG, acquires its transverse momentum entirely through the backward evolution in the shower mechanism. Such a mechanism is also present in MC@NLO, but there are also NLO real matrix elements in which a b quark has a large $p_{\rm T}$, which is inherited by the resulting b-flavoured hadron, and which explains the difference in the large-$p_{\rm T}^{(B)}$ tail between MC@NLO and HERWIG[9].

We conclude this section by mentioning the fact that we observe no dependence

[7] In MC@NLO, there are also $2 \to 3$ hard processes, whose matrix elements are the same as those of the NLO computation.

[8] b-flavoured hadrons from top decay are not included in this plot.

[9] For technical reasons, fig. 4.9 has been obtained by imposing $\left|y^{(B)}\right| < 3$. This cut has no impact for $p_{\rm T}^{(B)} > 10$ GeV.

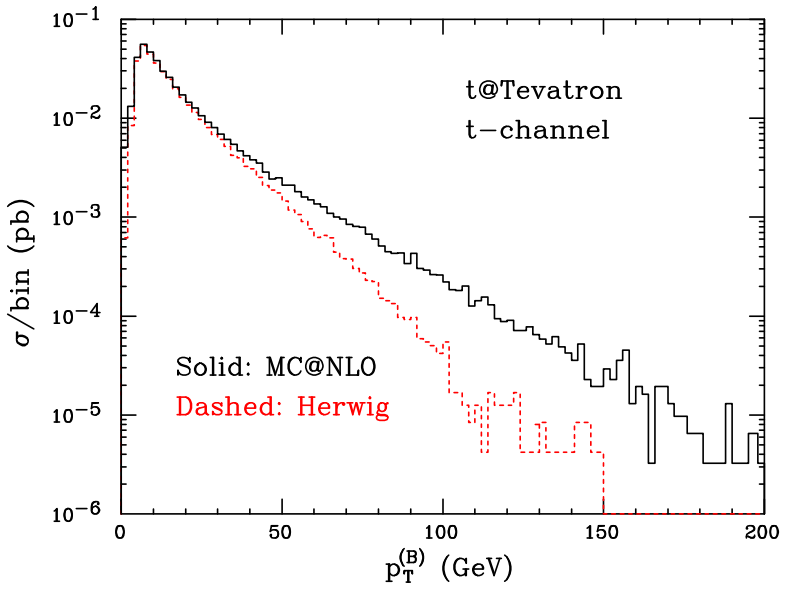

Figure 4.9: MC@NLO (solid) and HERWIG (dashed) results for the $p_{\rm T}$ of the b-flavoured hadrons (except those from top decay).

(within the statistical accuracy of the runs we performed) of the physical results upon the unphysical parameters which enter the NLO subtraction formalism, such as the subtraction parameters introduced in refs. [17, 18], or the exponent a introduced in eqs. (4.19) and (4.20). This constitutes a test of the correctness of our implementation, since NLO results based on subtraction techniques are by construction independent of these parameters. Similarly, no dependence has been found on the parameters α and β introduced in eqn. (**I**.A.86) and eqn. (**I**.A.87) which control the behaviour of the MC subtraction terms in the soft limit, if they are restricted to their natural ranges ($\alpha = \mathcal{O}(1)$, $\beta = \mathcal{O}(0.1)$). This is as expected, since variation of these parameters gives only power-suppressed effects. On the other hand, all of the above parameters do affect the number of negative-weight events, and their tuning can be used to limit the presence of such events (whose fraction is equal to about 15% in the results presented here). The parameter a has only a limited impact on the number of negative weights (which change by about 1% for $1 \leq a \leq 4$), and its choice is mainly due to considerations of stability of the numerical integration, with best results for $a = 2$. In general, the accuracy of the predictions obtained with values of a larger than 2 (slowly) decreases with increasing a. Since the limit $a \to \infty$ corresponds to the Θ-based implementation of the subtraction formalism, this indirectly proves that the implementation introduced in this chapter is more convenient from the numerical point of view.

4.4 Conclusions

In this chapter we have considered single-top hadroproduction in the context of the MC@NLO approach. This case is, apart from its phenomenological relevance, also interesting from the technical point of view, since it features both initial- and final-state collinear singularities, and thus has a radiation pattern different from that of all of the processes so far included in MC@NLO.

We have shown that this is not a difficulty of principle, since the MC@NLO formalism is unchanged with respect to its definition given in ref. [14], but it entails a more involved procedure in the generation of the hard events that are given to the parton shower as initial conditions. Because this procedure is not specific to single-top hadroproduction, and since we have now treated all possible radiation patterns in MC@NLO, we are now in a position to include any new process, such as jet production, without the need of performing further analytical computations.

As in previous cases, our computation is based on the universal subtraction formalism of refs. [17, 18]. We have used single-top hadroproduction as a test case, to explore an implementation of the subtraction different from that of the original papers. The partition of the phase space is now achieved by means of smooth functions of invariants, rather than with Θ functions as was done previously. This does not entail any change in the analytical formulae, but helps to improve the behaviour of the numerical computations. There is also a conceptual difference, namely that the infrared singularities are now disentangled by means of damping factors, rather than by non-overlapping regions defined by the phase-space partition. This in turn may lead to the possibility of implementing alternative subtraction schemes, although new analytical computations would be required in such a case.

We have not explored in this chapter the phenomenological implications of the work presented.
The phenomenological studies, as well as the implementation of the Wt mode and spin correlations, are dealt with in the succeeding chapters.

References

[1] P. Nason, S. Dawson, and R. K. Ellis. The total cross-section for the production of heavy quarks in hadronic collisions. *Nucl. Phys.*, B303:607, 1988.

[2] W. Beenakker, H. Kuijf, W. L. van Neerven, and J. Smith. Qcd corrections to heavy quark production in p anti-p collisions. *Phys. Rev.*, D40:54–82, 1989.

[3] P. Nason, S. Dawson, and R. K. Ellis. The one particle inclusive differential cross-section for heavy quark production in hadronic collisions. *Nucl. Phys.*, B327:49–92, 1989.

[4] W. Beenakker, W. L. van Neerven, R. Meng, G. A. Schuler, and J. Smith. Qcd corrections to heavy quark production in hadron-hadron collisions. *Nucl. Phys.*, B351:507–560, 1991.

[5] B. W. Harris, E. Laenen, L. Phaf, Z. Sullivan, and S. Weinzierl. The fully differential single top quark cross section in next-to-leading order qcd. *Phys. Rev.*, D66:054024, 2002.

[6] Zack Sullivan. Understanding single-top-quark production and jets at hadron colliders. *Phys. Rev.*, D70:114012, 2004.

[7] Zack Sullivan. Angular correlations in single-top-quark and w j j production at next-to-leading order. 2005.

[8] S. Zhu. Next-to-leading order qcd corrections to b g $\rightarrow$ t w- at the cern large hadron collider. *Phys. Lett.*, B524:283–288, 2002.

[9] John Campbell, R. K. Ellis, and Francesco Tramontano. Single top production and decay at next-to-leading order. *Phys. Rev.*, D70:094012, 2004.

[10] Qing-Hong Cao and C. P. Yuan. Single top quark production and decay at next-to-leading order in hadron collision. *Phys. Rev.*, D71:054022, 2005.

[11] Qing-Hong Cao, Reinhard Schwienhorst, and C. P. Yuan. Next-to-leading order corrections to single top quark production and decay at tevatron. i: s-channel process. *Phys. Rev.*, D71:054023, 2005.

[12] Qing-Hong Cao, Reinhard Schwienhorst, Jorge A. Benitez, Raymond Brock, and C. P. Yuan. Next-to-leading order corrections to single top quark production and decay at the tevatron. ii: t-channel process. 2005.

[13] John Campbell and Francesco Tramontano. Next-to-leading order corrections to w t production and decay. *Nucl. Phys.*, B726:109–130, 2005.

[14] Stefano Frixione and Bryan R. Webber. Matching nlo qcd computations and parton shower simulations. *JHEP*, 06:029, 2002.

[15] Stefano Frixione, Paolo Nason, and Bryan R. Webber. Matching nlo qcd and parton showers in heavy flavour production. *JHEP*, 08:007, 2003.

[16] Stefano Frixione and Bryan R. Webber. The mc@nlo 3.1 event generator. 2005.

[17] S. Frixione, Z. Kunszt, and A. Signer. Three-jet cross sections to next-to-leading order. *Nucl. Phys.*, B467:399–442, 1996.

[18] S. Frixione. A general approach to jet cross sections in qcd. *Nucl. Phys.*, B507:295–314, 1997.

[19] A. D. Martin, R. G. Roberts, W. J. Stirling, and R. S. Thorne. Uncertainties of predictions from parton distributions. i: Experimental errors. ((t)). *Eur. Phys. J.*, C28:455–473, 2003.

[20] S. Catani, Yu. L. Dokshitzer, M. H. Seymour, and B. R. Webber. Longitudinally invariant k(t) clustering algorithms for hadron-hadron collisions. *Nucl. Phys.*, B406:187–224, 1993.

Chapter 5

Angular correlations in Monte Carlo simulations

Accurate predictions for the spectra of the leptons emerging from decays of vector bosons or top quarks are important for a variety of studies at hadron colliders, such as acceptance computations, tests of QCD, and searches for new physics. Theoretical computations should be based on all Feynman diagrams in which the corresponding leptons are external legs. In general, not all such diagrams are *resonant* diagrams, i.e. those in which the leptons directly emerge from a vector boson propagator (which, in the case of top decays, in turn is directly connected to the top quark via a Wtb vertex). Usually, however, predictions based on computations that retain only the resonant diagrams are excellent approximations to those based on the fuller set of diagrams, owing to the rather narrow widths of the vector bosons and top quarks; the more so in the presence of final-state cuts which are designed to enhance on-shell contributions.

A further approximation can be made, which we call the *decay chain* approximation: resonant diagrams are replaced by diagrams relevant to the production of on-shell vector bosons or top quarks, times the diagrams corresponding to the matrix elements for the decays. In this way, off-shell effects are lost, but they can be recovered to some accuracy by reweighting the results of the decay chain approximation by a Breit-Wigner function. There is another piece of information that is lost in the decay chain approximation, and cannot be recovered, namely that on *production angular correlations* (more precisely, angular correlations due to production spin correlations). Let us denote by P the decaying particle (a vector boson or a top in our case), and by d_1, ..., d_n its decay products, and consider the hard process

$$a + b \longrightarrow P(\longrightarrow d_1 + \cdots + d_n) + X\,, \tag{5.1}$$

with X a set of final-state particles which may also contain other decaying vector

bosons or top quarks. The process of eqn. (5.1) is said to have decay angular correlations if the matrix elements of the corresponding resonant Feynman diagrams have a non-trivial dependence[1] on $(d_i \cdot d_j)$. Clearly, decay correlations are always present if the particle P has spin different from zero. The process of eqn. (5.1) has production angular correlations if its matrix elements have a non-trivial dependence on $(d_i \cdot a)$, $(d_i \cdot b)$, or $(d_i \cdot X)$. It is therefore clear that the decay chain approximation can account for the decay correlations, but not for the production correlations.

The decay chain approximation has obvious advantages, leading to much simpler computations (especially at higher orders) owing to the reduced multiplicity of the final state. Still, it is not acceptable if the spectra of the decay products must be predicted with some accuracy. The aim in this chapter is to introduce an approach to the computations of lepton spectra as given by resonant diagrams, which uses the decay chain approximation but also correctly accounts for production angular correlations. The method is primarily intended to be applied to parton shower Monte Carlos, including those that implement NLO QCD corrections such as MC@NLO [1, 2] or POWHEG [3]. The idea stems from the following observation: the matrix elements computed with the resonant diagrams are bounded from above by the matrix elements obtained by eliminating the decay products and putting the parent particles (vector bosons and/or top quarks) on-shell, times a process-independent constant. One can therefore use the latter matrix elements (which we call *undecayed* matrix elements) to perform computing-intensive tasks for which production correlations are not an issue. When the four-momenta of the parent particles are available, the resonant diagrams (we refer to the corresponding matrix elements as *leptonic* ones) are used in the context of a simple hit-and-miss procedure to generate the leptonic four-momenta.

In order to apply a hit-and-miss procedure, we need upper bounds on the decay matrix elements that are universal with respect to the production process. These are derived in the following section, first for vector boson, then for top quark decay, and finally for final states containing several vector bosons and/or top quarks. The practical application of these results is discussed in section 5.2. The inclusion of angular correlations in NLO computations is hampered by the presence of virtual corrections and the necessity for subtraction terms, which mean that one has to deal with expressions that are not simply matrix elements squared, and therefore are not necessarily positive-definite. This implies that the scheme we propose here is such that angular correlations are not accurate to NLO in the whole phase space, but are correct to NLO for hard real emissions and to LO in soft and collinear regions. Obviously, one can implement angular correlations exactly to NLO accuracy by using lepton matrix elements in all the steps of the

[1] We denote here a particle and its four-momentum by the same symbol.

computation. In this thesis, however, we are solely interested in the decay chain approximation. Illustrative results of our approach, obtained with MC@NLO, are presented in section 5.3, followed by our conclusions in section 5.4. An appendix presents an alternative derivation of the upper bound for vector boson decay, which may clarify some of the assumptions involved.

5.1 Upper bounds for the leptonic matrix elements

In this section, we derive the universal factors that, when multiplied by the undecayed matrix elements, give an upper bound for the leptonic matrix elements. After introducing some notation, we shall treat the cases of the vector bosons and of the top quarks in turn.

5.1.1 Notations

We shall always denote by

$$V \longrightarrow l\bar{l} \tag{5.2}$$

the decay of the vector boson $V \equiv W$ or Z into a lepton-antilepton pair, which means that in the case of W decay $\bar{l}$ is not the antiparticle of l. In our conventions, the $Vl\bar{l}$ vertex is

$$-iF_V\gamma^\mu\left(V_{Vl} - A_{Vl}\gamma_5\right), \tag{5.3}$$

where

$$F_Z = \frac{g_{\mathrm{w}}}{2\cos\theta_{\mathrm{w}}}, \quad V_{Zl} = V_l, \quad A_{Zl} = A_l; \tag{5.4}$$

$$F_W = \frac{g_{\mathrm{w}}}{2\sqrt{2}}, \quad V_{Wl} = 1, \quad A_{Wl} = 1. \tag{5.5}$$

We shall consider the process

$$a(P_1) + b(P_2) \longrightarrow V_1(q_1) + \ldots + V_n(q_n) + X(x) \tag{5.6}$$

$$\longrightarrow l_1(k_1) + \bar{l}_1(k_2) + \ldots + l_n(k_{2n-1}) + \bar{l}_n(k_{2n}) + X(x), \tag{5.7}$$

where

$$q_i = k_{2i-1} + k_{2i}\,, \tag{5.8}$$

and X collectively denotes any particles not originating from a vector boson decay. It is particularly convenient to write the phase space of the final-state particles of eqn. (5.7) as follows

$$d\Phi_{2n+1^\star}(P_1 + P_2; k_1, \ldots, k_{2n}, x) = d\Phi_{n+1^\star}(P_1 + P_2; q_1, \ldots, q_n, x) \prod_{i=1}^{n} d\Phi_2(q_i; k_{2i-1}, k_{2i}) \frac{dq_i^2}{2\pi}\,. \tag{5.9}$$

As the notation $1^\star$ suggests, we treat the particles X as a single particle with mass-squared x^2 and four-momentum x, since the individual four-momenta of the particles X are irrelevant in what follows. On the r.h.s. of eqn. (5.9), the two-body phase spaces account for the decays

$$V_i(q_i) \longrightarrow l_i(k_{2i-1}) + \bar{l}_i(k_{2i}). \tag{5.10}$$

The factorization formula of eqn. (5.9) is exact: the vector bosons are off-shell, and their virtualities q_i^2 (i.e., the invariant masses of the lepton pairs) are explicitly integrated over. This decomposition has an obvious physical interpretation in the context of resonant diagrams.

In the case of processes involving top quarks, we shall deal with

$$\begin{aligned} a(P_1) + b(P_2) &\longrightarrow t_1(p_1) + \ldots + t_n(p_n) + X(x) && (5.11)\\ &\longrightarrow W_1(q_1) + b_1(r_1) + \ldots + W_n(q_n) + b_n(r_n) + X(x) && (5.12)\\ &\longrightarrow l_1(k_1) + \nu_1(k_2) + b_1(r_1) + \ldots + l_n(k_{2n-1}) + \nu_n(k_{2n}) + b_n(r_n)\\ &\quad + X(x)\,, && (5.13) \end{aligned}$$

where t can be either a top or an antitop. As in eqn. (5.9), we can also write the exact phase-space factorization

$$\begin{aligned} &d\Phi_{3n+1^\star}(P_1+P_2; k_1, \ldots, k_{2n}, r_1, \ldots, r_n, x) =\\ &\quad d\Phi_{n+1^\star}(P_1+P_2; p_1, \ldots, p_n, x) \prod_{i=1}^{n} d\Phi_3(p_i; k_{2i-1}, k_{2i}, r_i)\, \frac{dp_i^2}{2\pi}\,, \end{aligned} \tag{5.14}$$

with the three-body phase spaces on the r.h.s. accounting for the decays

$$t_i(p_i) \longrightarrow W_i(q_i) + b_i(r_i) \longrightarrow l_i(k_{2i-1}) + \nu_i(k_{2i}) + b_i(r_i). \tag{5.15}$$

5.1.2 Vector boson decay

We start by considering the production of one $l\bar{l}$ pair, and we neglect the Z/γ interference. The amplitude for the process in eqn. (5.7) with $n = 1$ is

$$A = M^\mu \frac{i}{q^2 - m_V^2 + i m_V \Gamma_V} \left(-g_{\mu\nu} + \frac{q_\mu q_\nu}{m_V^2} \right) \bar{u}(k_1)(-iF_V)\gamma^\nu \left(V_{Vl} - A_{Vl}\gamma_5\right) v(k_2)\,, \tag{5.16}$$

where m_V and Γ_V are the mass and the width of the vector boson respectively, and M^μ is the amplitude for the process

$$a(P_1) + b(P_2) \longrightarrow V(q) + X(x)\,, \tag{5.17}$$

μ being the Lorentz index associated with V; the polarization four-vector of V is not included in M^μ. From eqn. (5.16) we get (neglecting lepton masses)

$$\begin{aligned}\sum_{\text{spins}} |A|^2 &= M^\mu M^{*\rho} \frac{(-g_{\mu\nu} + q_\mu q_\nu/m_V^2)\,(-g_{\rho\sigma} + q_\rho q_\sigma/m_V^2)}{(q^2 - m_V^2)^2 + (m_V\Gamma_V)^2} \\ &\times F_V^2\,\mathrm{Tr}\left[\left(V_{Vl}^2 + A_{Vl}^2 - 2V_{Vl}A_{Vl}\gamma_5\right) \not{k}_1\gamma^\nu \not{k}_2\gamma^\sigma\right]. \end{aligned} \tag{5.18}$$

We now consider the narrow width approximation $\Gamma_V \to 0$. We have

$$\frac{1}{(q^2 - m_V^2)^2 + (m_V\Gamma_V)^2} \;\longrightarrow\; \frac{\pi}{m_V\Gamma_V}\,\delta\left(q^2 - m_V^2\right). \tag{5.19}$$

The δ function, which puts the vector boson on shell, allows us to write

$$\left(-g^{\mu\nu} + \frac{q^\mu q^\nu}{m_V^2}\right) = \sum_\lambda \varepsilon_\lambda^\mu \varepsilon_\lambda^{*\nu}, \tag{5.20}$$

where ε_λ are the polarization four-vectors of the vector boson. Using eqn. (5.20), eqn. (5.18) becomes

$$\sum_{spin} |A|^2 = \frac{\pi}{m_V\Gamma_V} \sum_{\lambda\lambda'} \tilde{M}_\lambda \rho_{\lambda\lambda'} \tilde{M}_{\lambda'}^*\,\delta\left(q^2 - m_V^2\right), \tag{5.21}$$

where we defined

$$\tilde{M}_\lambda = M_\mu \varepsilon_\lambda^\mu, \tag{5.22}$$

which is the amplitude for the process of eqn. (5.17) for a given vector boson polarization λ. We also define

$$\rho_{\lambda\lambda'} = F_V^2\,\mathrm{Tr}\left[\left(V_{Vl}^2 + A_{Vl}^2 - 2V_{Vl}A_{Vl}\gamma_5\right) \not{k}_1 \not{\varepsilon}_\lambda^* \not{k}_2 \not{\varepsilon}_{\lambda'}\right] \tag{5.23}$$

which is, apart from the normalization, the decay density matrix[2] of the vector boson. This quantity can be explicitly computed; here, we only present it in the form of a diagonal matrix

$$\rho_{\lambda\lambda'} = \left(U\rho^D U^*\right)_{\lambda\lambda'}, \tag{5.24}$$

where

$$\rho^D = 2m_V^2 F_V^2\,\mathrm{diag}\left(0, (V_{Vl} - A_{Vl})^2, (V_{Vl} + A_{Vl})^2\right). \tag{5.25}$$

The cross section for the production of a lepton pair in the narrow width approximation is therefore

$$\begin{aligned} d\sigma_{l\bar{l}} &= \frac{1}{2s}\frac{\pi}{m_V\Gamma_V} \sum_{\lambda\lambda'} \left(\tilde{M}U\right)_\lambda \rho_{\lambda\lambda'}^D \left(\tilde{M}U\right)_{\lambda'}^* \delta\left(q^2 - m_V^2\right) \\ &\times \frac{dq^2}{2\pi}\,d\Phi_{1+1^*}(P_1 + P_2; q, x)\,d\Phi_2(q; k_1, k_2). \end{aligned} \tag{5.26}$$

[2]The density matrix is usually defined as the transpose of that in eqn. (5.23). See e.g. ref. [4].

Owing to the hermiticity properties of the density matrices, and to the explicit form of eqn. (5.25), eqn. (5.26) is a positive-definite quadratic form in the space of the spin indices of the vector boson. Thus

$$d\sigma_{l\bar{l}} \leq \frac{1}{2s}\frac{\pi}{m_V\Gamma_V}\max_{\lambda}\left(\rho^D_{\lambda\lambda}\right)|\tilde{M}|^2\frac{1}{2\pi}\,d\Phi_{1+1^\star}\,d\Phi_2\,, \tag{5.27}$$

where

$$|\tilde{M}|^2 = \sum_\lambda \tilde{M}_\lambda\tilde{M}^*_\lambda = \sum_\lambda\left(\tilde{M}U\right)_\lambda\left(\tilde{M}U\right)^*_\lambda = M^\mu M^{*\nu}\left(-g_{\mu\nu}+\frac{q_\mu q_\nu}{m_V^2}\right)\,, \tag{5.28}$$

with $q^2 = m_V^2$. Eqn. (5.27) cannot be used as an upper bound for the matrix element of the process (5.7), since the measures on the two sides are different. Using eqn. (5.19), we can however easily reinstate the q^2 integration by inserting

$$1 = \int dq^2\,\frac{m_V\Gamma_V}{\pi}\,\frac{1}{(q^2-m_V^2)^2+(m_V\Gamma_V)^2} \tag{5.29}$$

on the r.h.s. of eqn. (5.27). Furthermore, from eqn. (5.25) we obtain:

$$\max_{\lambda}\left(\rho^D_{\lambda\lambda}\right) = 2m_V^2F_V^2\left(V_{Vl}+A_{Vl}\right)^2\,, \tag{5.30}$$

which holds since $V_{Vl}A_{Vl} > 0$ regardless of the identity of the lepton l. Therefore

$$\frac{1}{2s}\sum_{spin}|A|^2 \equiv \frac{d\sigma_{l\bar{l}}}{d\Phi_{2+1^\star}} \leq \frac{2m_V^2\,F_V^2\left(V_{Vl}+A_{Vl}\right)^2}{(q^2-m_V^2)^2+(m_V\Gamma_V)^2}\,\frac{|\tilde{M}|^2}{2s}\,, \tag{5.31}$$

which strictly speaking holds only when $q^2 = m_V^2$, since all results in this section are formally derived in the limit $\Gamma_V \to 0$. More details on this, and the reason for keeping a formal dependence on q^2 in eqn. (5.31), will be given in appendix D. Eqn. (5.31) is the main result of this section. It states that, in the narrow width approximation, the lepton-pair cross section has an upper bound, which is a universal factor times the cross section for the production of the parent vector boson

$$\frac{d\sigma_V}{d\Phi_{1+1^\star}} = \frac{1}{2s}\,|\tilde{M}|^2\,. \tag{5.32}$$

5.1.3 Top decay

Here, we consider the decay of a top quark

$$t(p) \;\longrightarrow\; W^+(q)+b(r) \;\longrightarrow\; l^+(k_1)+\nu(k_2)+b(r); \tag{5.33}$$

the treatment of the decay of an antitop is fully analogous. Other top quarks may be present in the final state, but their decays are of no interest for the moment, and will be ignored. The amplitude for the process in eqn. (5.13) is

$$\begin{aligned} A &= \bar{u}(r)V_{tb}\frac{g_{\rm W}}{2\sqrt{2}}\gamma^\mu(1-\gamma_5)\frac{\not{p}+m_t}{p^2-m_t^2+im_t\Gamma_t}M \\ &\times \frac{-g_{\mu\nu}+q_\mu q_\nu/m_W^2}{q^2-m_W^2+im_W\Gamma_W}\bar{u}(k_2)\frac{g_{\rm W}}{2\sqrt{2}}\gamma^\nu(1-\gamma_5)v(k_1)\,, \end{aligned} \tag{5.34}$$

where M is the amplitude for the process

$$a(P_1)+b(P_2)\;\longrightarrow\;t(p)+X(x)\,, \tag{5.35}$$

except for a spinor $\bar{u}(p)$, which is not included. Therefore, $M=\Gamma u(K)$, with Γ a combination of γ matrices, and K the four-momentum of a fermion entering the hard scattering. By squaring eqn. (5.34) we get

$$\begin{aligned} |A|^2 &= \frac{g_{\rm W}^4\,|V_{tb}|^2}{64}\frac{1}{(p^2-m_t^2)^2+(m_t\Gamma_t)^2}\frac{1}{(q^2-m_W^2)^2+(m_W\Gamma_W)^2} \\ &\times \bar{u}(r)\gamma^\mu(1-\gamma_5)\,(\not{p}+m_t)\,MM^*\gamma^0\,(\not{p}+m_t)\,(1+\gamma_5)\gamma^\rho u(r) \\ &\times \bar{u}(k_2)\gamma_\mu(1-\gamma_5)v(k_1)\bar{v}(k_1)(1+\gamma_5)\gamma_\rho u(k_2)\,. \end{aligned} \tag{5.36}$$

Following what was done in eqn. (5.18), we now consider eqn. (5.36) in the narrow width approximation $\Gamma_t\to 0$, i.e. we make the replacement

$$\frac{1}{(p^2-m_t^2)^2+(m_t\Gamma_t)^2}\;\longrightarrow\;\frac{\pi}{m_t\Gamma_t}\,\delta\left(p^2-m_t^2\right)\,. \tag{5.37}$$

Thanks to the on-shell condition introduced in this way, we can use the analogue of eqn. (5.20)

$$\not{p}+m_t=\sum_\lambda u_\lambda(p)\bar{u}_\lambda(p), \tag{5.38}$$

which in turn suggests introducing the quantity

$$\tilde{M}_\lambda=\bar{u}_\lambda(p)M\quad\Longrightarrow\quad\tilde{M}^*_\lambda=M^*\gamma^0u_\lambda(p), \tag{5.39}$$

which is the analogue of eqn. (5.22), and is the amplitude for the process of eqn. (5.35) for a given top polarization λ. Upon summing over the spins of the final-state leptons and b quark, eqn. (5.36) can be cast in the same form as eqn. (5.21):

$$\sum_{spin}|A|^2=\frac{\pi}{m_t\Gamma_t}\sum_{\lambda\lambda'}\tilde{M}_\lambda\rho_{\lambda\lambda'}\tilde{M}^*_{\lambda'}\,\delta\left(p^2-m_t^2\right), \tag{5.40}$$

with

$$\begin{aligned}\rho_{\lambda\lambda'} &= \frac{g_{\rm W}^4\,|V_{tb}|^2}{16}\frac{1}{(q^2-m_W^2)^2+(m_W\Gamma_W)^2}\;{\rm Tr}[(1-\gamma_5)\not{k}_2\gamma_\mu\not{k}_1\gamma_\rho] \\ &\times\;\bar{u}_{\lambda'}(p)(1+\gamma_5)\gamma^\rho\not{r}\gamma^\mu u_\lambda(p)\,. \end{aligned} \tag{5.41}$$

This is the decay density matrix for the top quark, the analogue of eqn. (5.23). We can now proceed exactly as was done in sect. 5.1.2, and therefore we must compute the decay density matrix, diagonalize it, and find the largest of the matrix elements so obtained. An explicit computation leads to

$$\rho^D = \frac{4g_{\rm W}^4\,|V_{tb}|^2}{(q^2-m_W^2)^2+(m_W\Gamma_W)^2}\,(r\cdot k_2)(p\cdot k_1)\,{\rm diag}(0,1)\,. \tag{5.42}$$

Using eqn. (5.42) and reinstating the integral in dp^2 using the analogue of eqn. (5.29), we finally arrive at

$$\frac{1}{2s}\sum_{spin}|A|^2 \equiv \frac{d\sigma_{l\nu b}}{d\Phi_{3+1^\star}} \le \frac{4g_{\rm W}^4\,|V_{tb}|^2\,(r\cdot k_2)(p\cdot k_1)}{\Big((q^2-m_W^2)^2+(m_W\Gamma_W)^2\Big)\Big((p^2-m_t^2)^2+(m_t\Gamma_t)^2\Big)}\,\frac{|\tilde{M}|^2}{2s}\,, \tag{5.43}$$

which strictly speaking holds only when $p^2 = m_t^2$. Eqn. (5.43) is the analogue of eqn. (5.31), and expresses the upper bound on the matrix elements for the production of $l\nu b$ in terms of the matrix elements for the production of a top quark

$$\frac{d\sigma_t}{d\Phi_{1+1^\star}} = \frac{1}{2s}\,|\tilde{M}|^2\,. \tag{5.44}$$

In contrast to eqn. (5.31), the bound of eqn. (5.43) is not a constant over the phase space of the particles emerging from top decay, because of its dependence on $(r\cdot k_2)$ and $(p\cdot k_1)$. This helps to increase the efficiency of event generation in the context of an unweighting procedure, but in order to avoid any biases the phase-space must be sampled in such a way as to reproduce exactly the q^2-, $(r\cdot k_2)$-, and $(p\cdot k_1)$-dependences of the bound. An alternative approach is that of finding a constant larger than or equal to the bound, which can be done by finding the maximum of the combination of dot products

$$D = (r\cdot k_2)(p\cdot k_1)\,. \tag{5.45}$$

Using the top rest frame to perform the relevant computations, it is a matter of simple algebra to obtain

$$D \le D_{\rm max}(q^2) = \begin{cases} m_t^4/16 & q^2 \le \frac{m_t^2}{2}\,, \\ q^2(m_t^2-q^2)/4 & \frac{m_t^2}{2} < q^2 \le m_t^2\,. \end{cases} \tag{5.46}$$

Note that $m_t^4/16 \geq q^2(m_t^2 - q^2)/4$ in the whole q^2 range, and therefore one can always set $D_{\max} = m_t^4/16$; this is seen to lead to a very marginal degradation of unweighting efficiency. We have therefore

$$\frac{d\sigma_{l\nu b}}{d\Phi_{3+1^\star}} \leq \frac{4g_{\rm W}^4 \left|V_{tb}\right|^2 D_{\max}(q^2)}{\Big((q^2 - m_W^2)^2 + (m_W\Gamma_W)^2\Big)\Big((p^2 - m_t^2)^2 + (m_t\Gamma_t)^2\Big)} \frac{d\sigma_t}{d\Phi_{1+1^\star}} . \qquad (5.47)$$

5.1.4 Multiple decays

It is easy to generalize the formulae derived in the previous sections to the cases in which one is interested in the decay products of several vector bosons and/or top quarks. Consider for example the process of eqn. (5.7). An equation identical to eqn. (5.16) holds, with the formal replacements

$$M^\mu \quad \longrightarrow \quad M^{\mu_1 \ldots \mu_n} , \qquad (5.48)$$

$$\frac{-g_{\mu\nu} + q_\mu q_\nu/m_V^2}{q^2 - m_V^2 + im_V\Gamma_V} \quad \longrightarrow \quad \prod_{i=1}^{n} \frac{-g_{\mu\nu} + q_{i\mu} q_{i\nu}/m_{V_i}^2}{q_i^2 - m_{V_i}^2 + im_{V_i}\Gamma_{V_i}} , \qquad (5.49)$$

$$F_V \bar{u}(k_1)\gamma^\nu \left(V_{Vl} - A_{Vl}\gamma_5\right) v(k_2) \quad \longrightarrow \quad \prod_{i=1}^{n} F_{V_i} \bar{u}(k_{2i-1})\gamma^\nu \left(V_{V_i l_i} - A_{V_i l_i}\gamma_5\right) v(k_{2i}) \qquad (5.50)$$

The analogue of eqn. (5.26) features the quantity

$$\sum_{\lambda_1\lambda_1'} \ldots \sum_{\lambda_n\lambda_n'} \Big(\tilde{M} U_1 \ldots U_n\Big)_{\lambda_1\ldots\lambda_n} \rho^D_{1\lambda_1\lambda_1'} \ldots \rho^D_{n\lambda_n\lambda_n'} \Big(\tilde{M} U_1 \ldots U_n\Big)^*_{\lambda_1'\ldots\lambda_n'} , \qquad (5.51)$$

which results from the simultaneous diagonalization of the spin density matrices of the n vector bosons. This allows one to use eqn. (5.30), and to proceed as in the previous section. We therefore arrive at

$$\frac{d\sigma_{l_1\bar{l}_1\ldots l_n\bar{l}_n}}{d\Phi_{2n+1^\star}} \leq \left(\prod_{i=1}^{n} \frac{2m_{V_i}^2 F_{V_i}^2 \left(V_{V_i l_i} + A_{V_i l_i}\right)^2}{(q_i^2 - m_{V_i}^2)^2 + (m_{V_i}\Gamma_{V_i})^2}\right) \frac{d\sigma_{V_1\ldots V_n}}{d\Phi_{n+1^\star}} , \qquad (5.52)$$

where $d\sigma_{V_1\ldots V_n}$ is the cross section for the process of eqn. (5.6), all the vector bosons being on-shell.

Along the same lines, eqn. (5.47) can immediately be generalized to the case of the decays of several top and antitop quarks:

$$\frac{d\sigma_{l_1\nu_1 b_1\ldots l_n\nu_n b_n}}{d\Phi_{3n+1^\star}} \leq \left(\prod_{i=1}^{n} \frac{4g_{\rm W}^4 \left|V_{tb}\right|^2 D_{\max}(q_i^2)}{\Big((q_i^2 - m_W^2)^2 + (m_W\Gamma_W)^2\Big)\Big((p_i^2 - m_t^2)^2 + (m_t\Gamma_t)^2\Big)}\right) \frac{d\sigma_{t_1\ldots t_n}}{d\Phi_{n+1^\star}} . \qquad (5.53)$$

Obviously, eqs. (5.52) and (5.53) can be combined for the simultaneous presence of vector bosons and top quarks in the final state.

5.2 Angular correlations in MC@NLO

As mentioned in the introduction, the straightforward way to predict correctly all features of lepton spectra is to include in the computation the leptonic matrix elements, for example as done in MC@NLO version 3.3 [5] for the cases of single-V or VH production, or in refs. [6, 7] for the case of top quark decay in parton-level pure NLO computations. We remind the reader that, in the context of MC@NLO, parton-level cross sections (which are obtained by suitably modifying those which enter pure-NLO computations) are first integrated over the phase space of the final-state particles. The information gathered in this integration step is then used in the event-generation step, whose aim is that of obtaining a set of kinematic configurations (the *hard events*), which are subsequently showered by the parton shower Monte Carlo. We also point out that the same integration-and-generation structure is used by POWHEG (although the cross sections integrated in the two formalisms are not the same). The integration time increases rapidly with the number of final-state particles; there is a corresponding decrease in the efficiency of the generation of hard events. This is the reason why it is interesting to find alternative ways to predict angular correlations in large-multiplicity processes. We stress that in principle, the implementation in MC@NLO (or POWHEG) of a process with correct angular correlations is identical to that of the same process without such correlations. The problem is a practical one, namely that production angular correlations require the knowledge of the lepton matrix elements, and the increased multiplicity with respect to the undecayed matrix elements entails loss of accuracy and generation efficiency.

The strategy proposed here starts with the following steps.

1. Integrate the undecayed matrix elements.

2. Generate hard events using the results of the previous step; thus, vectors bosons and/or top quarks will be present in the final state, but not their decay products.

3. For each hard event, generate (massless) lepton (and b quark, in the case of top decays) four-momenta, uniformly within the decay phase space(s) of the corresponding parent particle(s).

4. Compute the lepton matrix element using the four-momenta obtained in step 3, and the undecayed matrix element using the four-momenta obtained in

step 2. Generate a flat random number r. If the lepton matrix element, divided by its upper bound as given in eqs. (5.52) and (5.53), is smaller than r, throw the lepton four-momenta away, and return to step 3.

5. Otherwise, replace the vector bosons and top quarks by the set of their decay products. The resulting kinematic configuration is the leptonic hard event that can be showered by the Monte Carlo.

Steps 3 to 5 constitute a standard hit-and-miss procedure, which guarantees that the lepton spectra reconstructed with the four-momenta of the leptonic hard event (and subsequent shower) will be identical to those computed by a direct integration of the leptonic matrix elements.

It is clear that the integration step will be greatly simplified by this procedure: the number of phase-space variables relevant to the undecayed processes (5.6) and (5.11) is $n_U = 3(n + n_X) - 4$, whereas $n_V = 3(2n + n_X) - 4$ and $n_t = 3(3n + n_X) - 4$ for leptonic processes (5.7) and (5.13) respectively. On the other hand, one may doubt that the efficiency for producing leptonic hard events is larger than in the case of a straightforward integration of the leptonic matrix elements. In fact, the adaptive integration performed in step 1 will only give information on the n_U degrees of freedom of the undecayed processes. However, using the phase-space decompositions of eqs. (5.9) and (5.14), one associates the extra $n_V - n_U = 3n$ and $n_t - n_U = 6n$ degrees of freedom with the decay phase spaces. Since we are considering here only resonant diagrams, the leptonic matrix elements will be fairly smooth in these extra $3n$ and $6n$ degrees of freedom, if the parametrizations of the decay phase spaces are properly chosen (the obvious choice of using the rest frame of the decaying particles is also an optimal choice from this point of view). Therefore, all of the complications due to the presence of several peaks in the matrix elements are dealt with in step 2. The unweighting performed in step 4 does not require any sophisticated numerical approach (i.e., a preliminary adaptive integration is not necessary) in order to achieve a satisfactory efficiency.

For the procedure as outlined above to work, it is crucial that the leptonic matrix elements can be bounded from above by the undecayed matrix elements. In the derivations of sect. 5.1 we have assumed that the density matrix is positive definite, which is the case, *and* that the matrix elements involved can be expressed as the modulus squared of an amplitude. This is certainly the case in the context of a tree-level computation, but it is not true for all the contributions to an NLO cross section. In particular, the interference between virtual and Born amplitudes is not positive-definite in general. The modified subtraction procedure [1] introduced in the MC@NLO formalism also implies the presence of a second quantity which is possibly not positive-definite, namely the difference between the real matrix elements and the MC subtraction terms. The presence of non-positive-definite

contributions is what prevents one from including angular correlations exactly to NLO accuracy in the context of the decay chain approximation, as anticipated in the beginning of the chapter.

Before proceeding, we remind the reader that there are two classes of MC@NLO hard events, defined according to their kinematics: $\mathbb{S}$ ($\mathbb{H}$) events have the same number of initial- and final-state particles as Born (real-emission) contributions. Thus, the number of final-state particles of $\mathbb{H}$ events is equal to that of $\mathbb{S}$ events, plus one. For example, in W^+W^- production (eqn. (5.6)) we have $(n, n_X) = (2, 0)$ for $\mathbb{S}$ events, and $(n, n_X) = (2, 1)$ for $\mathbb{H}$ events. In $t\bar{t}$ and single-top production (eqn. (5.11)), we have $(n, n_X) = (2, 0)$ and $(n, n_X) = (1, 1)$ for $\mathbb{S}$ events, and $(n, n_X) = (2, 1)$ and $(n, n_X) = (1, 2)$ for $\mathbb{H}$ events respectively. POWHEG (and, for that matter, any NLO computation) also outputs $\mathbb{S}$ and $\mathbb{H}$ events.

We now extend the procedure proposed in points 1 to 5 above to the case of NLO computations matched to parton shower simulations, as follows:

- Steps 1 and 2 are unchanged.

- For each $\mathbb{S}$ event, go through steps 3 to 5, using Born-level results to compute lepton matrix elements and their upper bounds.

- For each $\mathbb{H}$ event, compute a quantity $\mathcal{G}(\mathbb{H})$ as explained below and generate a random number r'. If $r' \leq \mathcal{G}(\mathbb{H})$, go through steps 3 to 5, using real-emission results to compute lepton matrix elements and their upper bounds. If $r' > \mathcal{G}(\mathbb{H})$, define an $\mathbb{S}$-type event with the projection $\mathcal{P}_{\mathbb{H}\to\mathbb{S}}(\mathbb{H})$, and proceed as explained for $\mathbb{S}$ events above.

The definition of a map $\mathcal{P}_{\mathbb{H}\to\mathbb{S}}$ is a necessary condition for the matching between NLO results and parton shower simulations: for more details see e.g. refs. [2, 8]. This implies that such a map need not be defined specifically for the purpose of including angular correlations into MC@NLO or POWHEG. The quantity $\mathcal{G}$ is a largely arbitrary smooth and continuous function, that assumes values between 0 and 1, and tends to 0 (1) in the soft/collinear (hard-emission) regions. The role of $\mathcal{G}$ is simply to avoid computing real-emission matrix elements in the phase-space regions where they diverge. In the context of MC@NLO, functions with the same behaviour as $\mathcal{G}$ need be introduced in order to ensure local cancellation between real matrix elements and MC counterterms (see e.g. app. A.5 of ref. [1] and app. B of ref. [2]), and one obvious choice is that of setting $\mathcal{G}$ equal to one of these functions (or to a combination of them).

It should be clear that the proposal made here accounts for angular correlations to LO accuracy close to the soft and collinear regions, since there $\mathcal{G}(\mathbb{H}) \simeq 0$, and therefore $\mathbb{H}$ events are projected onto $\mathbb{S}$ events, for which we only consider the

Born matrix elements in the hit-and-miss procedure[3]. On the other hand, in the hard emission region only real corrections contribute to the cross section, and thus angular correlations are included exactly to NLO accuracy[4]. Angular correlations resulting from an MC matched to an NLO computation and implementing the method proposed here have therefore the same or a better accuracy than LO-based Monte Carlos. We also stress that angular correlations are actually fairly close to those computed exactly to NLO, for two reasons. First, NLO corrections to spin correlations are generally small. Second, although virtual corrections and subtracted terms are not positive definite, their angular correlations arising from the contributions (if any) that are proportional to the Born matrix elements can be included exactly in the computation following the method proposed here, since both sides of eqs. (5.52) and (5.53) then get multiplied by the same factor.

5.3 Results

The approach described in the previous section has been adopted to include production angular correlations in MC@NLO in the cases of W^+W^- production (since version 3.1) and of $t\bar{t}$ and single-t production (since version 3.3). In this section we present sample results for $t\bar{t}$ and single-t production, at the LHC (pp collisions at $\sqrt{S} = 14$ TeV) and at the Tevatron run II ($p\bar{p}$ collisions at $\sqrt{S} = 1.96$ TeV). All the predictions given in this section have been obtained by using the MRST2002 default PDF set [9], and by setting $m_t = 175$ GeV and $\Gamma_t = 1.7$ GeV. In the case of single-t production, we also reconstruct the accompanying jets, by means of the $k_{\rm T}$-clustering algorithm [10], with $d_{cut} = 100$ GeV^2. We include in the clustering procedure all final-state stable hadrons and photons. For the sake of simplicity, we force π^0's and all lowest-lying b-flavoured states to be stable in HERWIG. The jets are ordered in transverse momentum.

We begin by considering $t\bar{t}$ production. We have studied, at the Tevatron and at the LHC, single-inclusive $p_{\rm T}$ and rapidity spectra of the t and $\bar{t}$ decay products, and the correlations in transverse momentum, $\Delta\phi$, and invariant mass of the $b\bar{b}$, l^+l^-, bl^-, $\bar{b}l^+$, $b\bar{\nu}$, and $\bar{b}\nu$ pairs. We have found that angular correlations have an almost negligible impact. We present in fig. 5.1 the only two observables for which these correlations have a visible effect, albeit barely so for $p_{\rm T}(l^+l^-)$. On the other hand, angular correlations are an important ingredient for the correct prediction of $\Delta\phi(l^+l^-)$, as shown in the right pane of fig. 5.1. It is interesting that about 30% of the difference between the LO prediction without angular correlations (dashed histogram – HERWIG) and the NLO prediction with angular correlations

[3] We remind the reader that the full NLO undecayed matrix elements are used in steps 1 and 2.

[4] One should bear in mind that radiation from the decay products is not included here.

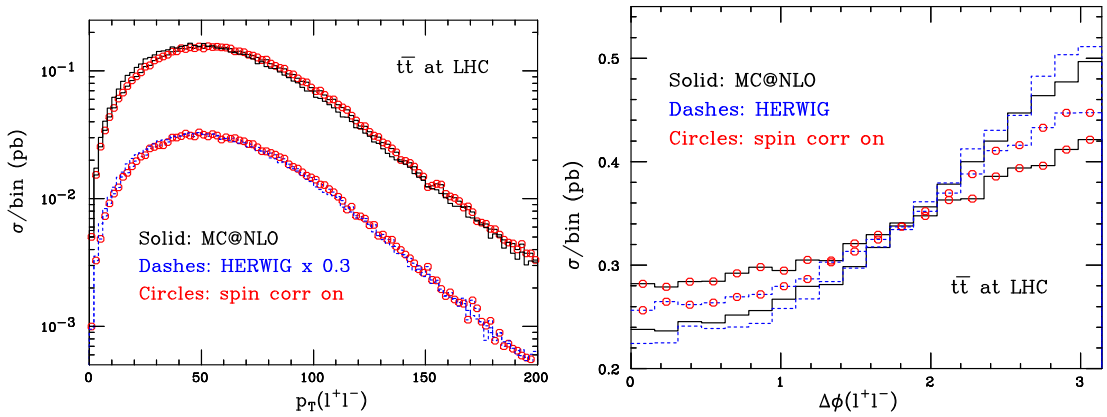

Figure 5.1: Transverse momentum of the lepton pair (left pane), and difference in azimuthal angle between the leptons (right pane), in $t\bar{t}$ production at the LHC. HERWIG results have been rescaled (by 0.3 on the left, and by the factor $K = \sigma_{\rm NLO}/\sigma_{\rm LO}$ on the right).

(solid histogram, overlayed with open circles – MC@NLO) is due to beyond-LO corrections.

It is possible to specifically design observables which would be trivial if angular correlations were neglected. Typically, such observables are angular variables constructed with the decay products of the top quarks, and measured in the rest frames of the parent particle. We have considered the distributions in $\cos\theta_1$, $\cos\theta_2$, and $\cos\phi$, as defined in ref. [11]; in particular, ϕ is the angle between the direction of flight of l^+ and the direction of flight of l^-. The directions of flight are defined in the t and $\bar{t}$ rest frames respectively (see ref. [11] for more details). Results for $\cos\phi$ are presented in fig. 5.2 for the Tevatron (left pane) and the LHC (right pane). Just as for $\Delta\phi(l^+l^-)$, beyond-LO contributions are not negligible, and they tend to deplete (at the Tevatron) or to enhance (at the LHC) the LO predictions for the $\cos\phi$ asymmetry. This behaviour is also found in the pure-NLO, parton-level study of ref. [11]. We have verified that, by neglecting angular correlations, the cross section depends trivially on θ_1, θ_2 and ϕ.

Finally, we examine distributions for single-top production at the Tevatron. Because both production and decay occur through the left-handed charged current interaction, one expects stronger production angular correlations than in top quark pair production. Indeed, angular correlation effects are clearly visible in the single-inclusive spectra of the top decay products. As in the case of $t\bar{t}$ production, it is possible to study angular correlations more directly by choosing specific observables. These observables always involve the definition of a spin basis that leads to nearly 100% correlation between the direction of the charged lepton from

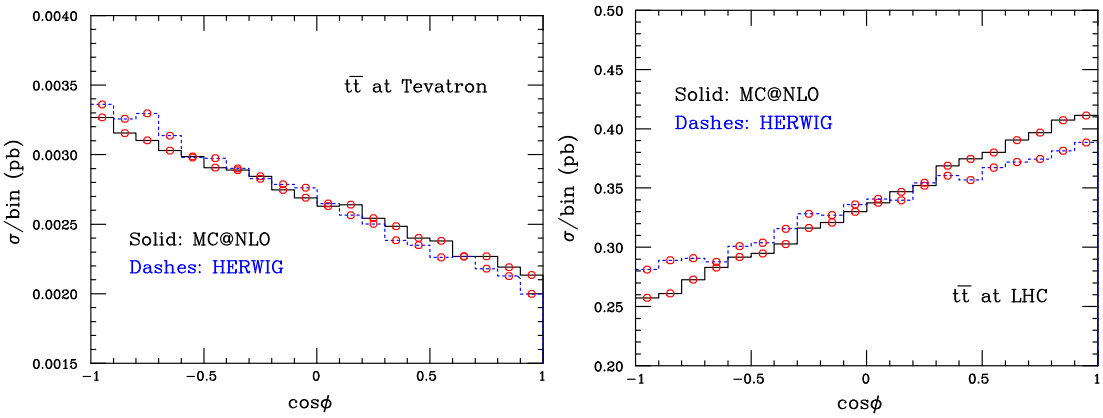

Figure 5.2: Opening angle distributions, as defined in the text, for $t\bar{t}$ production at the Tevatron (left pane) and at the LHC (right pane). HERWIG results have been rescaled by the K factor. The corresponding curves obtained by neglecting angular correlations are flat, and are not shown in the figure.

top decay and another experimentally-definable, channel-dependent direction [12]. For both s- and t-channel processes the optimal spin quantization axis lies, in the top quark rest frame, along the down-type quark attached to the vertex connected via a W-boson to the top quark producing vertex. At LO that corresponds for the s channel to the beam-direction, while for the t channel this is most often the direction of the light quark jet against which the top quark recoils.

Accordingly, we present in the left pane of fig. 5.3 the distribution in the cosine of the angle θ, defined as the angle between the direction of flight of the lepton emerging from top decay, and the axis of the hardest jet which does not contain a stable b-flavoured hadron; the angle is defined in the rest frame of the top quark. This distribution has been shown in ref. [13] at tree level, and in ref. [14] at NLO using MCFM [6]. We have applied similar cuts as those in ref. [13], namely we required the decay products of the top to have

$$p_{\mathrm{T}}(b) \geq 20 \text{ GeV}\,, \qquad |\eta(b)| \leq 2\,, \tag{5.54}$$
$$p_{\mathrm{T}}(l) \geq 10 \text{ GeV}\,, \qquad |\eta(l)| \leq 2.5\,, \tag{5.55}$$
$$p_{\mathrm{T}}(\nu) \geq 20 \text{ GeV}\,. \tag{5.56}$$

We also require the hardest light jet to have transverse momentum larger than 20 GeV, and $|\eta(j)| \leq 2.5$. In this way, we obtain $A = -0.35$, where

$$A = \frac{\sigma(-1 \leq \cos\theta < -0.1) - \sigma(-0.1 \leq \cos\theta < 0.8)}{\sigma(-1 \leq \cos\theta < -0.1) + \sigma(-0.1 \leq \cos\theta < 0.8)}\,. \tag{5.57}$$

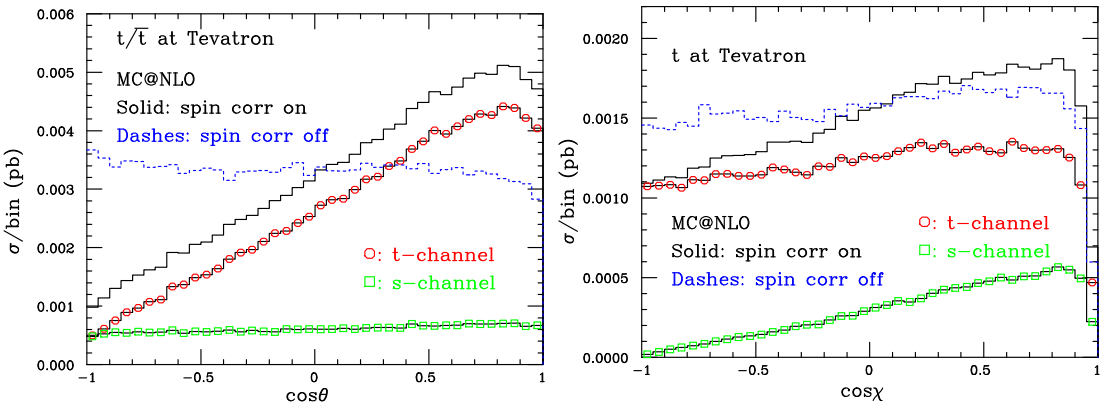

Figure 5.3: Angular correlations in single-top processes at the Tevatron: $\cos\theta$ in single-$t/\bar{t}$ production (left pane), and $\cos\chi$ in single-t production (right pane). Histograms without symbols are the sums of s- and t-channel contributions.

As can be seen from fig. 5.3, this result is due to the contribution of the t-channel, the s-channel having a very small asymmetry. We remark that the asymmetry is also compatible with zero if spin correlations are switched off. It is important to notice that our results follow the same pattern (and are actually close numerically) of those of refs. [13, 14]. Although we did not carry out a comprehensive study, this fact implies that not only is the $\cos\theta$ asymmetry fairly robust when including higher order corrections, but it is also stable when passing from a parton-level description such as that of refs. [13, 14] to a more realistic hadron-level description such as that of MC@NLO.

We conclude by presenting in the right pane of fig. 5.3 the distribution in the cosine of the angle χ, which is defined analogously to the angle θ, except for the fact that the reference direction is chosen to be that of the antiproton beam (at variance with the case of $\cos\theta$, we have limited ourselves here to considering t production, rather than $t+\bar{t}$ production). As expected [12], the dominant contribution to the asymmetry is due in this case to the s-channel. An extremely small non-zero asymmetry may also be visible in the case in which angular correlations are not included; we have verified that this is an artifact of the cuts adopted in the present analysis.

5.4 Conclusions

We have presented a method for the efficient inclusion of angular correlations due to production spin correlations in Monte Carlo event generators. The method has

been demonstrated in detail for vector boson and top quark decays, but it is in fact quite general, relying only on the fact that the matrix elements do not contain sharp features that would lead to unacceptably low efficiency. The method is exact, and equivalent to what is currently implemented in LO-accurate event generators such as HERWIG. When the event generator is matched to NLO predictions, as is the case for MC@NLO and POWHEG, the resulting correlations are correct to LO in soft and collinear regions and to NLO elsewhere. The method has been implemented in MC@NLO for WW, $t\bar{t}$ and single-top hadroproduction and leptonic decay, and we have presented illustrative results for the latter two cases. These results show that significant correlations are present in suitably chosen observables. Version 3.3 of MC@NLO implements off-shell effects only in the case of WW production. Future versions will include off-shell effects in top decay; also, vector bosons and top quarks decaying hadronically can be simulated using the formalism presented here, bearing in mind that NLO corrections to decays are neglected.

References

[1] Stefano Frixione and Bryan R. Webber. Matching nlo qcd computations and parton shower simulations. *JHEP*, 06:029, 2002.

[2] Stefano Frixione, Paolo Nason, and Bryan R. Webber. Matching nlo qcd and parton showers in heavy flavour production. *JHEP*, 08:007, 2003.

[3] Paolo Nason. A new method for combining nlo qcd with shower monte carlo algorithms. *JHEP*, 11:040, 2004.

[4] E. Merzbacher. *Quantum mechanics*. Quantum mechanics / Eugen Merzbacher. New York : Wiley, c1998., 1998.

[5] Stafano Frixione and Bryan R. Webber. The mc@nlo 3.3 event generator. 2006.

[6] John Campbell, R. K. Ellis, and Francesco Tramontano. Single top production and decay at next-to-leading order. *Phys. Rev.*, D70:094012, 2004.

[7] Qing-Hong Cao and C. P. Yuan. Single top quark production and decay at next-to-leading order in hadron collision. *Phys. Rev.*, D71:054022, 2005.

[8] P. Nason. Embedding nlo calculations in shower event generators with positive weights. Prepared for 14th International Workshop on Deep Inelastic Scattering (DIS 2006), Tsukuba, Japan, 20-24 Apr 2006.

[9] A. D. Martin, R. G. Roberts, W. J. Stirling, and R. S. Thorne. Uncertainties of predictions from parton distributions. i: Experimental errors. ((t)). *Eur. Phys. J.*, C28:455–473, 2003.

[10] S. Catani, Yu. L. Dokshitzer, M. H. Seymour, and B. R. Webber. Longitudinally invariant k(t) clustering algorithms for hadron-hadron collisions. *Nucl. Phys.*, B406:187–224, 1993.

[11] W. Bernreuther, A. Brandenburg, Z. G. Si, and P. Uwer. Top quark pair production and decay at hadron colliders. *Nucl. Phys.*, B690:81–137, 2004.

[12] Gregory Mahlon and Stephen Parke. Angular correlations in top quark pair production and decay at hadron colliders. *Phys. Rev.*, D53:4886–4896, 1996.

[13] T. Stelzer, Z. Sullivan, and S. Willenbrock. Single top quark production at hadron colliders. *Phys. Rev.*, D58:094021, 1998.

[14] Zack Sullivan. Angular correlations in single-top-quark and w j j production at next-to-leading order. 2005.

Chapter 6

Single-top production through the Wt mode

The top quark, discovered in 1995 [1, 2], is a prime study object at the Tevatron, which has produced a few thousand. The forthcoming LHC will be a veritable top quark factory. The large mass of the top, close to electroweak scale, enables direct scrutiny of its behavior in collisions, unshrouded by hadronization effects. Being so heavy, the top quark should also be sensitive to effects of new physics, the scale of which is thought to be near the electroweak scale. As reviewed in earlier chapters, an interesting process to study in this regard is the production of single t's, via the weak interaction. The Standard Model predicts this cross section to be somewhat smaller than the already observed $t\bar{t}$ pair production via the strong interaction. This, together with difficult-to-remove backgrounds, has so far prevented this production process from being definitively identified in Tevatron experiments.

In a leading order description, single top production can happen in 3 modes, depicted in fig. 6.1. Each of these allows a separate and complementary exam-

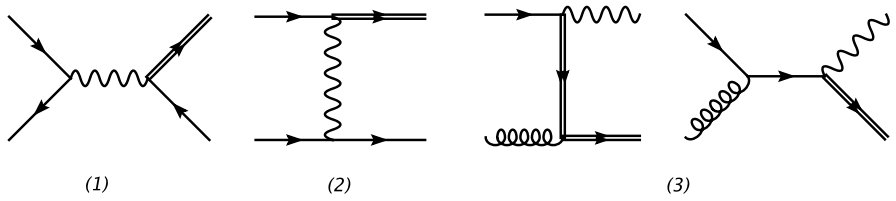

Figure 6.1: Leading order diagrams for single-t production in the (1) s-channel, (2) t-channel and (3) Wt-mode. The t-quark line is doubled.

ination of the Wtb vertex. Such an examination can consist of determining the

vertex's flavour structure (V_{tb}), its chiral structure, strength etc [3]. The s-channel mode involves a time-like, off-shell W and might reveal new resonances (heavy W'); the t-channel mode involves a space-like W and is sensitive to Flavour Changing Neutral Currents (FCNC's). The Wtb vertex in the Wt production mode has an on-shell W with an off-shell fermion connected to it, and is therefore complementary. At the Tevatron the latter process has far too small a cross section to be observed, but at the LHC its cross section is significant.

For accurate estimates of rates and some distributions, necessary for reliably confronting theoretical predictions with data, next-to-leading order (NLO) calculations are required. Calculations of fully-differential NLO single-t cross sections for Wt production have been performed in refs. [4, 5]. On the other hand, in order to optimize acceptance cuts in an experimental analysis or to perform full detector simulations, one needs realistic hadron-level events, which are obtained with Monte Carlo event generators that incorporate the simulation of parton showers and hadronization models.

The complementary benefits of fixed-order computations and parton shower simulations are by now well-known, as are the advantages of combining them into a framework which would retain the strong points of each of them. The MC@NLO approach [6, 7] provides a way of achieving this, by allowing one to match cross sections computed at NLO in QCD with an event generator. No modifications to the latter are necessary, and therefore existing parton shower Monte Carlos can be used for this purpose.

In earlier chapters we included the s- and t-channel modes into the MC@NLO framework, and extended the framework by including angular correlations of leptons and quarks arising from vector boson and top quark decays. In this chapter we include the Wt single top production mode into the MC@NLO framework. We thereby complete the full MC@NLO description of the single-top production process for both the Tevatron and the LHC, including spin-correlations of its decay products.

As we will make clear below, the NLO calculation of the present process has challenging peculiarities of its own, which make the inclusion into MC@NLO nontrivial. Chief among these is the interference with the $t\bar{t}$ process. A careful and meaningful definition is then required to define the Wt process, and we will consider and compare various ones.

This chapter is organized as follows. In section 6.1 we discuss the NLO computation of Wt production. Section 6.2 briefly discusses the definition of the MC subtraction terms needed for the matching with the NLO result in the MC@NLO inclusion. Some results are shown and discussed in section 6.3. Conclusions in section 6.4 are followed by two appendices in which some technical details are collected.

6.1 $W+t$ associated production

In this section we discuss the calculations necessary to describe Wt production at NLO. Rather than go into great detail, we shall focus on those aspects of this mode that differ from the s and t channel mode, which merit special attention.

6.1.1 NLO computation

In what follows we shall denote where no confusion is possible the light quark attached to the Wtb vertex as a b, which thus implicitly represents any CKM-allowed down type quark. The lowest order calculation of the Wt process is based on the Feynman diagrams in fig. 6.1, involving a bg initial state. The NLO calculation involves virtual corrections to these diagrams, some of which are shown in fig. 6.2, as well as real emission diagrams. In order to implement a process in MC@NLO its NLO cross section must be computed according to the subtraction formalism presented in refs. [8, 9], denoted as FKS henceforth. Parts of the calculational methods we use were already employed for the NLO calculation for the Wc process in [10], for which the diagrams are almost identical. However, because in that case the phase space slicing method [11, 12, 13] was used rather than the FKS method, we recalculated most of the diagrams using the latter method.

Our description is confined to single top quark production. As explained in appendix F, for single anti-top quark production no new diagrams need be computed, so we do not discuss it further here.

6.1.2 Born

The lowest order parton level process is

$$b(p_1)+g(p_2)\longrightarrow t(k_1)+W^-(k_2)\,. \tag{6.1}$$

We define the invariants

$$s=(p_1+p_2)^2,\quad t_1=t-m^2=(k_1-p_1)^2-m^2,\quad u_1=u-m^2=(k_2-p_1)^2-m^2 \tag{6.2}$$

for which $s+t_1+u_1=m_W^2-m^2$, with m denoting the top quark mass. The lowest order cross section is

$$d\sigma^{(0)}=\frac{1}{2s}\frac{1}{4}\frac{1}{N(N^2-1)}g^2\frac{g_w^2}{8}\,|\mathcal{A}^{(0)}|^2\,d\,\mathrm{PS}(2)\,, \tag{6.3}$$

where g, g_w are the QCD and EW couplings, N is the number of colours, and where the spin-summed lowest order matrix element squared is given by

$$\mathcal{M}^{(0)} = |\mathcal{A}^{(0)}|^2 = 16NC_F \Bigg\{ \left[-\left(\frac{s}{t_1} + \frac{t_1}{s}\right)\left(1 + \frac{m^2}{2m_W^2}\right)\right] + 2\left[\left(\frac{m_W^2(s+t_1)t_1 + m^2 m_W^2 s}{s t_1^2}\right)\left(1 - \frac{m^2}{2m_W^2} - \frac{m^4}{2m_W^4}\right)\right] - \frac{m_W^2}{s t_1}\left(2 + \frac{3m^2}{m_W^2} - \frac{m^6}{m_W^6}\right) - \frac{m^2}{m_W^2}\Bigg\}. \quad (6.4)$$

6.1.3 Virtual diagrams

The one-loop diagrams that constitute the virtual corrections are shown in fig. 6.2.

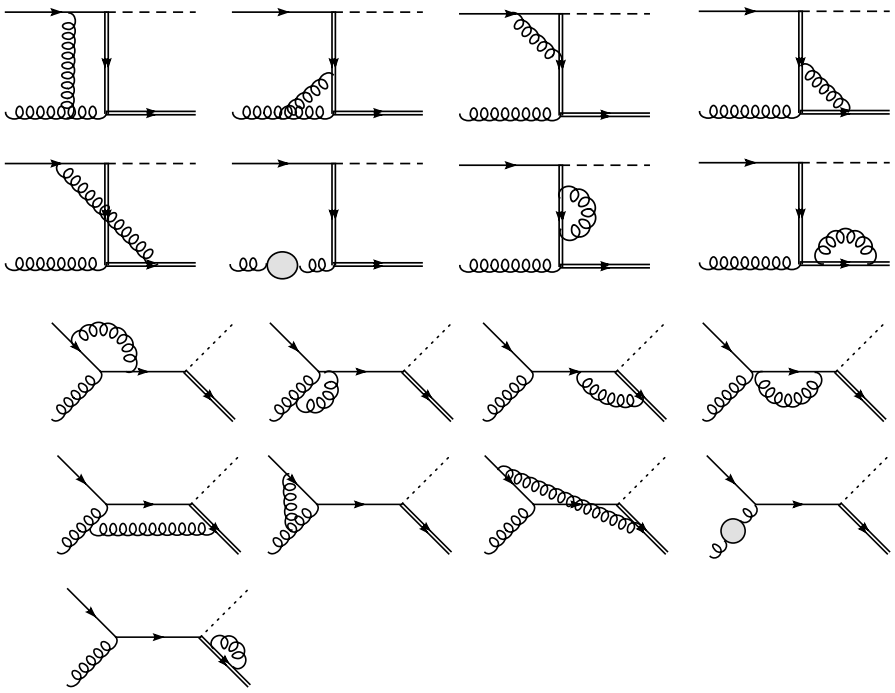

Figure 6.2: One-loop diagrams for Wt.

We have calculated them using a standard procedure. Working in $d = 4-2\epsilon$ dimensions we reduced tensor, and vector loop integrals to scalar ones using Passarino-Veltman reduction. We used the computer program FORM [14] for much of the

algebra, together with the packages FeynArts [15] and FormCalc [16]. The results were checked against the virtual contributions obtained for $W + c$ associated production in ref. [10] and were found to be in agreement.

The results are a Laurent series in the parameter ϵ, the double and single poles representing infrared, initial-state collinear and ultraviolet singularities. To remove the ultraviolet ones we renormalize the top quark mass using an on-shell condition, and the QCD coupling in the $\overline{\text{MS}}$ scheme, modified so that the top quark loop contribution is also subtracted on-shell. This particular scheme [17] ensures that the top quark virtual contributions decouple in the limit of small external momenta. Specifically, the coupling is renormalized through next-to-leading order as

$$g \to g(\mu_R^2)\left[1 + \left(\frac{\alpha_s(\mu_R^2)}{8\pi}\right)\left(\frac{-1}{\epsilon} + \gamma_E - \ln 4\pi\right)\beta_0\left(\frac{\mu^2}{\mu_R^2}\right)^{\epsilon} + \left(\frac{\alpha_s(\mu_R^2)}{8\pi}\right)\frac{2}{3}\ln\left(\frac{\mu_R^2}{m^2}\right)\right] \tag{6.5}$$

where μ is the scale used in dimensional regularization to make all dimensionalities explicit, and μ_R is the renormalization scale. Furthermore, $\beta_0 = (11N - 2n_f)/3$ with n_f equal to the number of light flavours (here 5) plus 1. From this condition one can derive the following relation for the renormalized QCD coupling

$$\mu_R^2 \frac{dg(\mu_R^2)}{d\mu_R^2} = -g(\mu_R^2)\left(\frac{\alpha_s(\mu_R^2)}{8\pi}\right)\left(\beta_0 + \frac{2}{3}\right) + \mathcal{O}(g^5)\,, \tag{6.6}$$

which indeed removes the top quark loop from the β-function. The top quark mass renormalization condition reads

$$m \to m + \delta m = m\left[1 + \left(\frac{\alpha_s(\mu_R^2)}{4\pi}\right)C_F\left(\frac{-3}{\epsilon} + \gamma_E - \ln 4\pi - 4 - 3\ln\left(\frac{\mu^2}{m^2}\right)\right)\right]. \tag{6.7}$$

In contrast to the s and t channel the top quark occurs as an internal line in the Born amplitude. Its mass renormalization therefore requires a derived quantity in terms of the amplitude $\mathcal{A}'^{(0)}$, which is identical to $\mathcal{A}^{(0)}$ except that the top propagator is "squared" because of mass renormalization

$$\frac{i}{\not{p} - (m + \delta m)} = \frac{i}{\not{p} - m} + \frac{i}{\not{p} - m}\delta m \frac{1}{\not{p} - m} \tag{6.8}$$

The resulting contribution to the cross section is

$$d\sigma_{\delta m}^{(1),V} = (\delta m)_{\text{finite}} \frac{1}{2s}\frac{1}{4}\frac{1}{N(N^2-1)} g^2 \frac{g_w^2}{8}\,\mathcal{M}'^{(0)}\,d\,\text{PS}(2)\,, \tag{6.9}$$

where

$$\mathcal{M}'^{(0)} = |\mathcal{A}^{(0)}\mathcal{A}'^{(0)} + \mathcal{A}'^{(0)}\mathcal{A}^{(0)}| = -16NC_F\frac{m^2}{m_W^2 s t_1^3}\Big\{ \left(4m^6 s + 4m^4 s(m_W^2 + t_1)\right) + m^2\left(-8m_W^4 s + 2m_W^2 s t_1 + t_1(t_1+u_1)(s+2u_1)\right) + t_1\left(t_1 u_1(t_1+u_1) + m_W^2(-s(t_1-2u_1) + 4u_1(t_1+u_1))\right)\Big\}. \quad (6.10)$$

After renormalization, soft and collinear singularities, appearing as $1/\epsilon^2$ and $1/\epsilon$ poles, remain and are proportional to the Born cross section

$$d\sigma^{(1),V} = C_\epsilon g^2\left[-\frac{2}{\epsilon^2}(C_F + C_A) + \frac{2}{\epsilon}C_A\left(\ln\frac{s}{m^2} + \ln\frac{-t_1}{m^2} - \ln\frac{-u_1}{m^2}\right) + C_F\left(2\ln\frac{-u_1}{m^2} - 1\right)\right] d\sigma^{(0)} + d\sigma^{(1),V}_{\text{finite}} \quad (6.11)$$

where

$$C_\epsilon = \frac{(4\pi e^{-\gamma_E})^\epsilon}{16\pi^2}\left(\frac{\mu^2}{m^2}\right)^\epsilon. \quad (6.12)$$

These remaining poles are cancelled by similar contributions in the real contributions and by the collinear counterterms that arise from the renormalization of the parton densities, in a form prescribed by the FKS formalism.

6.1.4 Real contributions

The basic idea in the FKS method is that the phase space of the real-emission contributions to the process is partitioned such that the parts do not overlap, cover the whole of phase space, and each contain at most one collinear and one soft singularity. In each such region it is natural to select that parton (dubbed the FKS parton) with which the singularities are associated. While this requires some care in processes with massless final state partons, in the present case collinear singularities are only associated with incoming partons, therefore requiring no special effort to separate regions.

The actual computation of the real radiative graphs was done in a manner similar to that of the Wc process in [10]. The amplitudes for the fictitious W-decays

$$W(q) \longrightarrow t(p) + \mathbf{b}_3(q_3) + g_4(q_4) + g_5(q_5)\,, \quad (6.13)$$

and

$$W(q) \longrightarrow t(p) + \mathbf{b}_3(q_3) + b_4(q_4) + \mathbf{b}_5(q_5)\,. \quad (6.14)$$

were decomposed into colour-ordered amplitudes, and computed. The radiative graphs for Wt were then obtained by crossing and summing over colour orders, saving somewhat on calculational effort[1]. These methods are quite standard and were also employed for the calculational of the s and t channel modes.

One aspect of the Wt single top production mode that is different from the s and t channel modes involves the initial state collinear regions. While the standard FKS subtractions can be employed to remove actual initial state collinear divergences, it is important for proper numerical sampling of the near-collinear regions to understand the finite parts of the collinear limits of squared radiative amplitudes. Let us denote by $\mathcal{M}_{ab}^{real}$ the amplitude squared

$$\lim_{k\|p_i} \mathcal{M}_{ab}^{real} = \frac{4\pi\alpha_S\mu^{2\epsilon}}{k\cdot p_i}\Delta_{ab}(p_i,k) + \frac{4\pi\alpha_S\mu^{2\epsilon}}{k\cdot p_i}P_{ab}^{<}(z,\epsilon)\mathcal{M}^{(0)}(p_i), \tag{6.15}$$

where k is the 4-momentum of the FKS parton emitted from initial leg p_i, $P_{ab}^{<}$ is an Altarelli-Parisi splitting function with momentum fraction $z<1$, and $\mathcal{M}^{(0)}$ the squared Born amplitude summed over helicities. Here $\{a,b\}$ are partonic indices for the emitted particle and the radiating initial leg, respectively. The function $\Delta_{ab}(p_i,k)$ depends on the azimuthal angle of the emitted parton, and vanishes when averaged over the azimuthal angle of the collinearly emitted parton. It is nonzero when the particular radiative process involves an exchanged gluon, e.g. $(b,g;t,W,g)$. Such radiative processes do not occur in the s and t channel mode of single top production, but they do here. This term is proportional (up to an overall phase) to:

$$\tilde{\mathcal{M}} = 2\,\mathrm{Re}\left[\mathcal{A}_+^{(0)\dagger}\mathcal{A}_-^{(0)}\right], \tag{6.16}$$

with $\mathcal{A}_\pm$ the Born amplitude for Wt production with a positive/negative helicity initial gluon respectively. In appendix E we demonstrate how to calculate this term explicitly.

Partonic processes

Here we briefly discuss the various radiative amplitudes that constitute the real contributions. We recall that b symbolically denotes the down-type quark connected to the top with a W vertex, and q is a light quark or antiquark. We shall use the shorthand notation

$$(\alpha,\beta;t,W,\delta) \tag{6.17}$$

for the momentum assignments

$$\alpha(p_1)+\beta(p_2) \longrightarrow t(k_1)+W(k_2)+\delta(k)\,, \tag{6.18}$$

[1]The colour-ordered amplitudes served a second purpose, namely in the accounting of colour connections in the parton shower stage of the MC@NLO construction.

where α and β are the incoming partons from the left ($p_1^3 > 0$) and from the right ($p_2^3 < 0$) respectively; δ is the FKS parton for NLO tree-level processes; it is absent in the case of $2 \to 2$ processes.

The singularity structure of some of the radiative amplitudes depends on the particular flavours α, β, δ. Thus, for $\alpha\beta = gg$ we have $\delta = \bar{b}$, the latter implicitly representing any CKM-allowed down type anti-quark, and only initial-state collinear singularities involving gluon to $b\bar{b}$ splitting are present. For $\alpha, \beta = bg$ we have $\delta = g$ and we have both soft and collinear (involving gluon-to-gluon splitting) singularities. Finally, we discuss the case where both α and β are quarks. For $\alpha\beta = q\bar{q}$ the singularity structure depends on the flavour of q. If $q = u, c$ or a downtype quark not equal to δ then there are no singularities. If either α or β is equal to δ (e.g a $\bar{b}$) then a collinear singularity is present. Similarly, if $\alpha\beta = bq$ for any q then again a collinear singularity is present.

In our method we have carefully distinguished and treated all these cases separately.

Interference with $t\bar{t}$ production

The theoretical (and experimental) definition of the Wt mode is not as straightforward as a LO calculation would suggest. At NLO, there are final states involving a t, a W^- and a $\bar{b}$. These can also arise from a LO $t\bar{t}$ production process, with subsequent decay of the $\bar{t}$, see fig. 6.3. These two production processes will there-

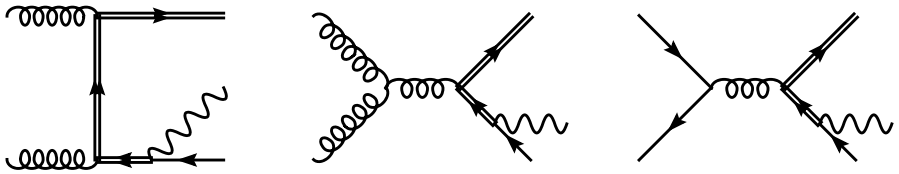

Figure 6.3: Diagrams that are doubly-resonant, in the sense that the intermediate $\bar{t}$ can be on-shell.

fore interfere, and their separation becomes a matter of careful definition. This $t\bar{t}$ process is in fact included in the $q\bar{q}$ and gg channel where some of the diagrams in the amplitude can become resonant when the $W^-\mathbf{b}$ pair approaches the top quark mass. The Wt single top production mode must be separated from the $t\bar{t}$ production process by a meaningful definition.

Although this subject has been addressed earlier [3, 4], we address it here for our specific context. We define three methods to effect this separation. Each has its advantages and drawbacks, which we will mention.

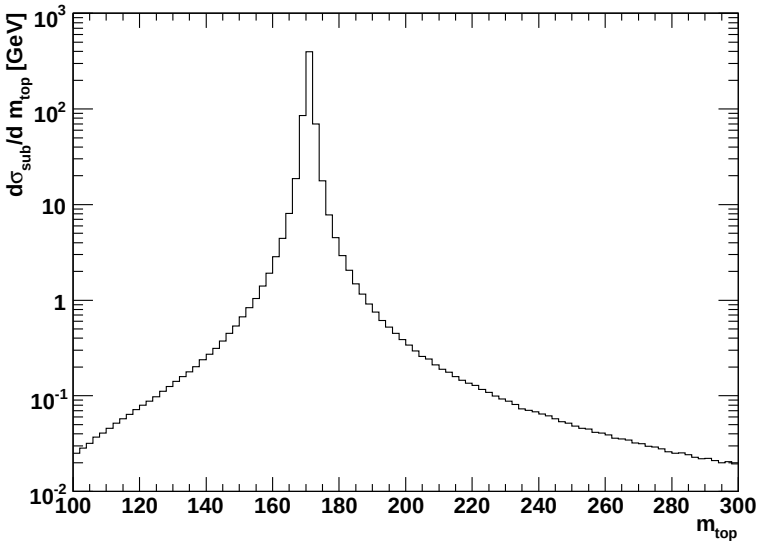

Figure 6.4: Subtraction term vs. off-shellness q_t^2.

Diagram removal

One simply removes the diagrams that are doubly-resonant. This works well numerically, but has obvious theoretical drawbacks.

Subtraction

This amounts to removal of doubly-resonant diagrams by subtraction in the narrow-width approximation (NWA). The subtraction term has the schematic form

$$|\mathcal{A}(ab \to t\bar{t})|^2 \times \frac{\mathrm{BW}(q_t^2)}{\mathrm{BW}(m^2)} \times |\mathcal{A}(\bar{t} \to W\bar{b})|^2 \tag{6.19}$$

where $ab = gg$ or $q\bar{q}$, and $\mathrm{BW}(q_t^2)/\mathrm{BW}(m^2)$ represents a ratio of the Breit-Wigner for an off-shell $\bar{t}$ with off-shellness q_t^2 to a Breit-Wigner with an on-shell top. The subtraction term, plotted by itself, is shown in fig. 6.4. It is clearly peaked around the top quark mass, but is non-zero for other values of q_t^2. This is because a momentum reshuffling is implemented in the code that put the $\bar{t}$ on-shell. This is later compensated to some extent in the MC@NLO code.

A drawback of this method is that a fully consistent implementation would require including a width all real contributions and their subtractions as well. This is at present not yet done.

Process removal

A more drastic solution than diagram removal simply removes the complete gg and $q\bar{q}$ channels from Wt production. In this way one removes a complete gauge-invariant set. The drawback of this method is that the absence of these channels upsets the renormalization group invariance of the complete process. However, because the numerical contribution of the gg and $q\bar{q}$ channels is quite small, the overall result is not much affected.

Having identified three methods to remove the doubly-resonant (i.e. with both on-shell top and anti-top) contributions, a further, experimentally implementable criterion is necessary that removes most of the $t\bar{t}$ background, while not removing too much of the Wt signal. An interesting suggestion to separate singly and doubly-resonant physics was made in ref. [4]. It involved using as a discriminant the transverse momentum of the second-hardest (in p_T) b-quark or b-hadron in an event, being most likely not from top quark decay. I.e. events in which the second-hardest b-quark is quite large are more likely to come from the decay of a resonant anti-top quark, whereas events in which the second-hardest b-quark has small p_T are more likely Wt events. Therefore, the p_T of second-hardest b-quark (or b-hadron) can be used as a veto in the definition of Wt events. In the results section we will be able to see the impact of the various removal definitions and the veto condition on the NLO calculation.

6.2 MC@NLO

The implementation of the Wt mode into the MC@NLO framework is fairly straightforward. The inclusion of this process however brings in a number of features which are different from previously included processes. We mention first the presence of two massive particles (W and t) with *different* masses. Also, in regard to spin correlations, they have different decays. Finally, there is the interference with $t\bar{t}$, which we have previously discussed. Below we discuss only the MC subtraction terms. Further details will be given in ref. [18].

6.2.1 MC subtraction terms

The MC subtraction terms constitute the first order expansion of the parton shower algorithm [19] in the HERWIG [20] Monte Carlo. These algorithms depend on such quantities as the starting scale, and the colour state of the emitters. We write these

terms as

$$d\sigma\Big|_{\rm MC} = \sum_{i,j}\sum_{L}\sum_{l} d\sigma_{i,j}^{(L,l)}\Big|_{\rm MC}\,, \tag{6.20}$$

The index L assumes the values $+$, $-$, and f_1 (for emissions from partons with momenta p_1, p_2, and from the top quark respectively). The index l, which runs over colour structures, assumes the values $q_i \cdot q_j$, where q_i and q_j are the four-momenta of the colour partners relevant to the emission considered; in this way, the shower scale is

$$E_0^2 = |l| \equiv |q_i \cdot q_j|. \tag{6.21}$$

We have

$$d\sigma_{i,j}^{(+,l)}\Big|_{\rm MC} = \frac{1}{z_+^{(l)}} f_a^{(H_1)}(\bar{x}_{1i}/z_+^{(l)}) f_b^{(H_2)}(\bar{x}_{2i})\, d\hat{\sigma}_{i,j}^{(+,l)}\Big|_{\rm MC} d\bar{x}_{1i}\, d\bar{x}_{2i}\,, \tag{6.22}$$

$$d\sigma_{i,j}^{(-,l)}\Big|_{\rm MC} = \frac{1}{z_-^{(l)}} f_a^{(H_1)}(\bar{x}_{1i}) f_b^{(H_2)}(\bar{x}_{2i}/z_-^{(l)})\, d\hat{\sigma}_{i,j}^{(-,l)}\Big|_{\rm MC} d\bar{x}_{1i}\, d\bar{x}_{2i}\,, \tag{6.23}$$

$$d\sigma_{i,j}^{(f_1,l)}\Big|_{\rm MC} = f_a^{(H_1)}(\bar{x}_{1f}) f_b^{(H_2)}(\bar{x}_{2f})\, d\hat{\sigma}_{i,j}^{(f_1,l)}\Big|_{\rm MC} d\bar{x}_{1f}\, d\bar{x}_{2f}\,, \tag{6.24}$$

The expressions for the short-distance cross sections are

$$d\hat{\sigma}_{i,j}^{(\pm,l)}\Big|_{\rm MC} = \frac{1}{\mathcal{N}}\frac{\alpha_s}{2\pi}\frac{d\xi_\pm^{(l)}}{\xi_\pm^{(l)}} dz_\pm^{(l)} P_{a'b'}^{(0)}(z_\pm^{(l)})\, d\bar{\sigma}_{i',3}\Theta\left((z_\pm^{(l)})^2 - \xi_\pm^{(l)}\right), \tag{6.25}$$

$$d\hat{\sigma}_{i,j}^{(f_1,l)}\Big|_{\rm MC} = \frac{\alpha_s}{2\pi}\frac{d\xi_{f_1}^{(l)}}{\xi_{f_1}^{(l)}} dz_{f_1}^{(l)} P_{a'b'}^{(0)}(z_{f_1}^{(l)})\, d\bar{\sigma}_{i,3}\Theta\left(1-\xi_{f_1}^{(l)}\right)\Theta\left(z_{f_1}^{(l)} - \frac{m_1}{E_0\sqrt{\xi_{f_1}^{(l)}}}\right), \tag{6.26}$$

where the flavours a', b', and the value of i' are determined by the singularity structures of the real emission contributions. The factor $\mathcal{N}$ inserted in eqn. (6.25) is equal to 2 when the corresponding emission is due to the branching of a gluon (thus taking into account the fact that the gluon has two colour partners). In the case of quark branchings, $\mathcal{N} = 1$. In table 6.1 we list explicitly all the terms which give non-trivial contributions to eqn. (6.20). The shower scales to be used in eqs. (6.25) and (6.26) are equal to the absolute values of the dot products listed in the tables above.

6.3 Results

In this section we show results of phenomenological studies at the NLO and MC@NLO level. The studies will mostly address the sensitivity of the predictions to choice of scale, p_T veto and of the method to separate the channel from $t\bar{t}$. At the LO level we have checked that we have agreement with the predictions

NLO	$(b,g;t,W)$	$(g,b;t,W)$
$(g,g;t,W,\mathbf{b})$	$+(\mathbf{p}_1\cdot\mathbf{p}_2)$	$-(\mathbf{p}_1\cdot\mathbf{p}_2)$
$(b,q;t,W,q)$	$-(\mathbf{p}_1\cdot\mathbf{p}_2,\mathbf{p}_2\cdot\mathbf{k}_1)$	
$(q,b;t,W,q)$		$+(\mathbf{p}_1\cdot\mathbf{p}_2,\mathbf{p}_1\cdot\mathbf{k}_1)$
$(b,\mathbf{b};t,W,\mathbf{b})$	$-(\mathbf{p}_1\cdot\mathbf{p}_2,\mathbf{p}_2\cdot\mathbf{k}_1)$	
$(\mathbf{b},b;t,W,\mathbf{b})$		$+(\mathbf{p}_1\cdot\mathbf{p}_2,\mathbf{p}_1\cdot\mathbf{k}_1)$
$(b,b;t,W,b)$	$-(\mathbf{p}_1\cdot\mathbf{p}_2,\mathbf{p}_2\cdot\mathbf{k}_1)$	$+(\mathbf{p}_1\cdot\mathbf{p}_2,\mathbf{p}_1\cdot\mathbf{k}_1)$
$(b,g;t,W,g)$	$+, f_1(\mathbf{p}_1\cdot\mathbf{k}_1); -(\mathbf{p}_1\cdot\mathbf{p}_2,\mathbf{p}_2\cdot\mathbf{k}_1)$	
$(g,b;t,W,g)$		$-, f_1(\mathbf{p}_2\cdot\mathbf{k}_1); +(\mathbf{p}_1\cdot\mathbf{p}_2,\mathbf{p}_1\cdot\mathbf{k}_1)$

Table 6.1: Short-distance contributions to MC subtraction terms. The two columns correspond to the two possible Born cross sections. For a given process, the entries show the emitting legs, and in round brackets the value(s) of the shower scale(s) E_0 (up to a sign).

from MCFM [4]. Such a comparison at NLO was not possible due to different choice of subtraction formalism and method to separate the $t\bar{t}$ component. Results in this section have been obtained for the LHC by using the MRST2002 default PDF set [21], and by setting the top mass and width to $m = 170.9$ GeV and $\Gamma_t = 1.41$ GeV, respectively as well as the W mass and width to $m_W = 80.4$ GeV and $\Gamma_W = 2.141$ GeV. Our default choice for p_T^{veto} is 50 GeV, and for the renormalization and factorization scale it is the top quark mass.

With these choices and no further cuts the total rates for the Wt modes were found to be 47.8, 45.6 and 50.1 pb for diagram removal, subtraction, and process removal respectively. The fact that the rate for process removal is larger than diagram removal is because in process removal the (negative) FKS formalism counterevents for the gg channel are also removed.

We begin showing results for the NLO calculation. For more realistic final states, and for better comparison with MC@NLO results, we have included the (leading order) decay of the top quark to an anti-lepton, neutrino and b quark. In fig. 6.5 we show the effect of the NLO corrections for two different p_T distributions, and in fig. 6.6 for a rapidity and an azimuthal distibution. We see that for the distributions shown, the effects of including the QCD corrections is most noticeable in their overall size, whereas their shapes are less affected. In fig. 6.7 we show the effect of choosing different methods to remove $t\bar{t}$ contributions from the Wt mode, as discussed in section 6.1.4. We see that the diagram removal and subtraction are remarkably close, while the distributions for process removal are similar in shape but larger, as remarked upon above. The effect of an additional veto condition of the second-hardest b quark in the event is shown in fig. 6.8. Clearly, the tightest

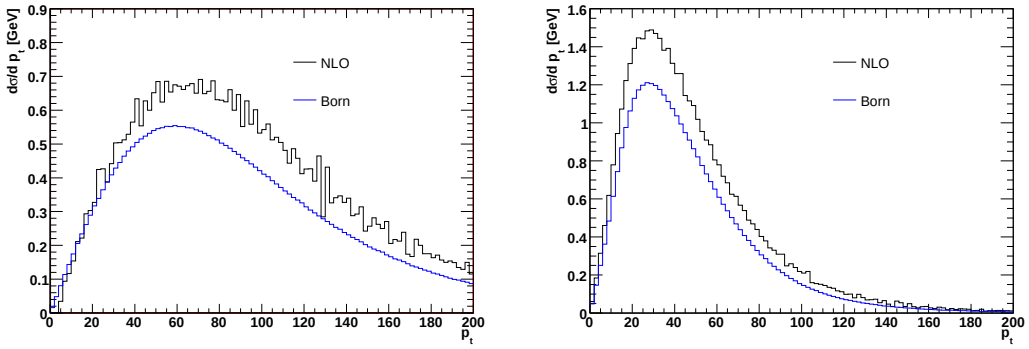

Figure 6.5: NLO vs. Born: transverse momentum of top quark, and its decay lepton.

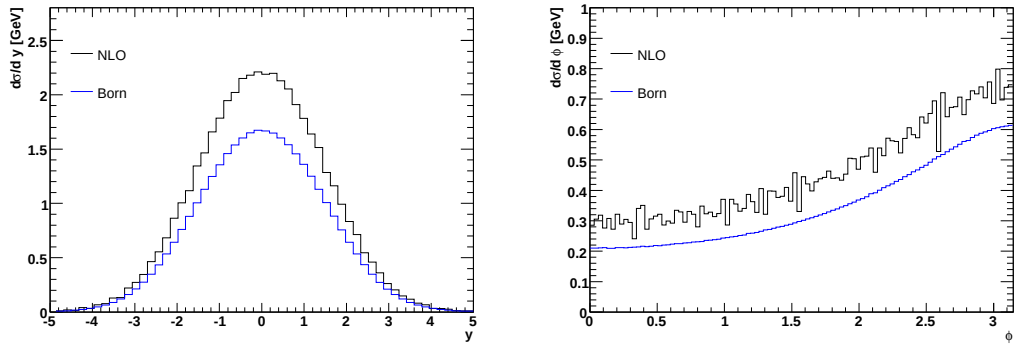

Figure 6.6: Born vs. NLO: the rapidity of the lepton from the W decay, together with the azimuthal distribution of the decay leptons.

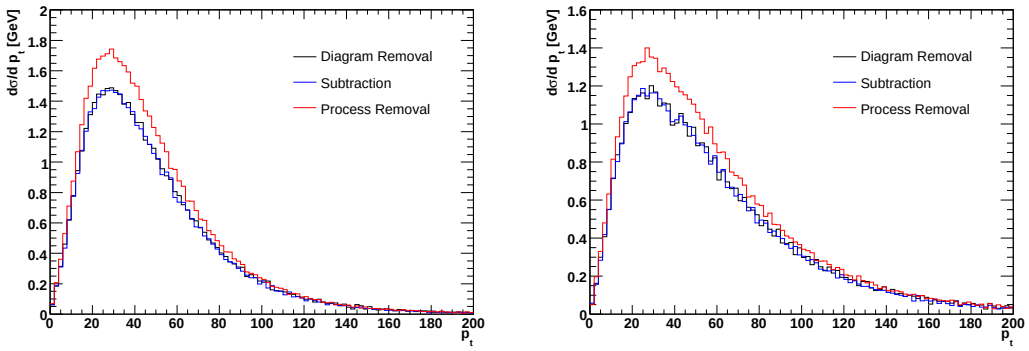

Figure 6.7: Comparison of diagram removal, diagram subtraction and process removal for the transverse momenta of the leptons from the top and W decays, respectively.

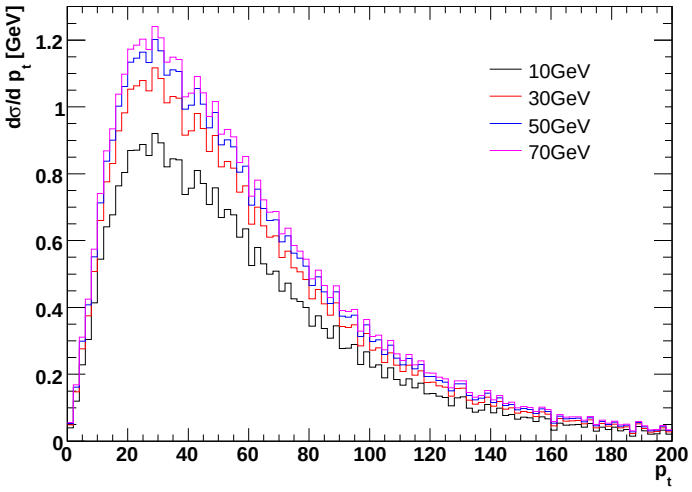

Figure 6.8: Dependence of the transverse momentum of the W upon the transverse momentum of the second-hardest b-quark, on which the veto-condition is imposed upon.

veto condition leads to the smallest cross section. Note that the results were computed using the diagram removal method. Finally, some results after varying

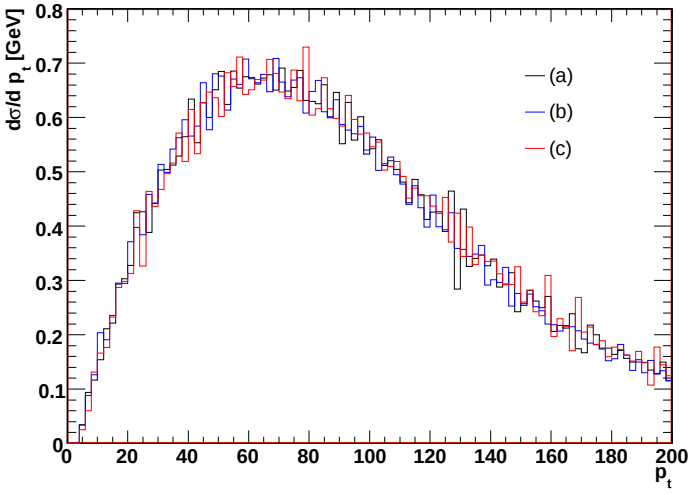

Figure 6.9: Scale dependence of the top quark transverse momentum distribution. The scale choices for the renormalization and factorization scale are, resp: (a) both equal to default; (b) twice and half the default resp.; (c) both equal to the transverse mass $m_T = \sqrt{m^2 + p_{T,top}^2}$.

the renormalization and factorization scales are shown in fig. 6.9. The differences are very small.

At the end of this section we also briefly show some MC@NLO results for this single-top production mode. We contrast in fig. 6.10 the top quark p_T distribution from the NLO and the MC@NLO calculations. As in the s and t channel case, the two descriptions for this very inclusive variable are very close. We also show the azimuthal angle difference between the top quark and the W boson. We see that the multiple emissions in MC@NLO allow for more decorrelation between the t and W directions.

6.4 Conclusions

In this chapter we have described the calculation of the QCD corrections for single-top production at the LHC via the Wt production mode in the FKS formalism. We have focussed on those aspects which distinguish this mode from the s and t channel ones, described in earlier chapters. We have also performed the inclusion of this

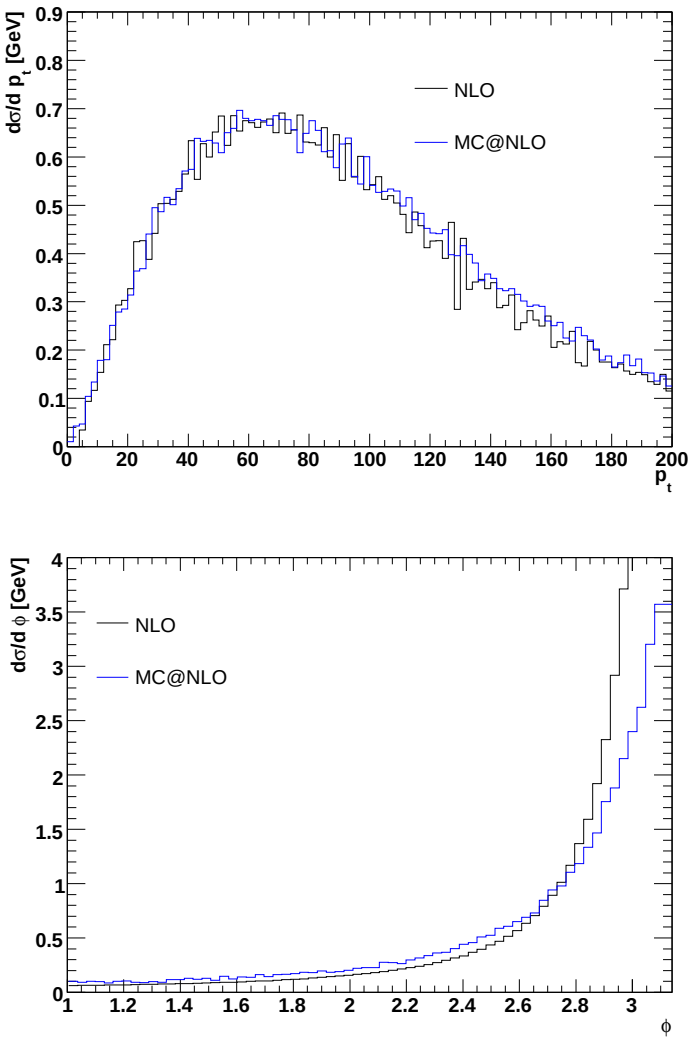

Figure 6.10: Upper figure: Top quark p_T distribution from the NLO and MC@NLO calculations. Lower figure: Azimuthal angle difference between the top quark and the W boson.

process into the MC@NLO framework. Thus, all major single top quark production modes have now been included in this framework, including spin correlations. Hence, the Standard Model description of single-top production at the LHC, a very important study objective of bothy the ATLAS and CMS experiments, is now in excellent shape.

References

[1] F. Abe et al. Observation of top quark production in anti-p p collisions. *Phys. Rev. Lett.*, 74:2626–2631, 1995.

[2] S. Abachi et al. Observation of the top quark. *Phys. Rev. Lett.*, 74:2632–2637, 1995.

[3] Tim M. P. Tait. The t w- mode of single top production. *Phys. Rev.*, D61:034001, 2000.

[4] John Campbell and Francesco Tramontano. Next-to-leading order corrections to w t production and decay. *Nucl. Phys.*, B726:109–130, 2005.

[5] S. Zhu. Next-to-leading order qcd corrections to b g $\rightarrow$ t w- at the cern large hadron collider. *Phys. Lett.*, B524:283–288, 2002.

[6] Stefano Frixione and Bryan R. Webber. Matching nlo qcd computations and parton shower simulations. *JHEP*, 06:029, 2002.

[7] Stefano Frixione, Paolo Nason, and Bryan R. Webber. Matching nlo qcd and parton showers in heavy flavour production. *JHEP*, 08:007, 2003.

[8] S. Frixione, Z. Kunszt, and A. Signer. Three-jet cross sections to next-to-leading order. *Nucl. Phys.*, B467:399–442, 1996.

[9] S. Frixione. A general approach to jet cross sections in qcd. *Nucl. Phys.*, B507:295–314, 1997.

[10] Walter T. Giele, Stephane Keller, and Eric Laenen. Qcd corrections to w boson plus heavy quark production at the tevatron. *Phys. Lett.*, B372:141–149, 1996.

[11] W. T. Giele and E. W. N. Glover. Higher order corrections to jet cross-sections in e+ e- annihilation. *Phys. Rev.*, D46:1980–2010, 1992.

[12] W. T. Giele, E. W. N. Glover, and David A. Kosower. Higher order corrections to jet cross-sections in hadron colliders. *Nucl. Phys.*, B403:633–670, 1993.

[13] Stephane Keller and Eric Laenen. Next-to-leading order cross-sections for tagged reactions. *Phys. Rev.*, D59:114004, 1999.

[14] J. A. M. Vermaseren. New features of form. 2000.

[15] Thomas Hahn. Generating feynman diagrams and amplitudes with feynarts 3. *Comput. Phys. Commun.*, 140:418–431, 2001.

[16] T. Hahn and M. Perez-Victoria. Automatized one-loop calculations in four and d dimensions. *Comput. Phys. Commun.*, 118:153–165, 1999.

[17] J. Collins, F. Wilczek, and A. Zee. Low-energy manifestations of heavy particles: Application to the neutral current. *Phys. Rev.*, D18:242, 1978.

[18] Stefano Frixione, Eric Laenen, Fabio Maltoni, Patrick Motylinski, Bryan R. Webber, and Chris White. Single top production through the wt mode. in preparation.

[19] G. Marchesini and B. R. Webber. Monte carlo simulation of general hard processes with coherent qcd radiation. *Nucl. Phys.*, B310:461, 1988.

[20] G. Marchesini et al. Herwig: A monte carlo event generator for simulating hadron emission reactions with interfering gluons. version 5.1 - april 1991. *Comput. Phys. Commun.*, 67:465–508, 1992.

[21] A. D. Martin, R. G. Roberts, W. J. Stirling, and R. S. Thorne. Uncertainties of predictions from parton distributions. i: Experimental errors. ((t)). *Eur. Phys. J.*, C28:455–473, 2003.

Conclusions

In the first part of this dissertation we have been focussing on perturbation theory and the predictive power of QCD. In particular Chapter 2 focussed on the issue of soft and collinear effects in joint- and threshold resummation for prompt photon production at both collider and fixed target kinematics. The inclusion of terms of the form

$$\alpha_s^i \sum_j^{2i-1} d_{ij} \frac{\ln^j N}{N} \,. \tag{6.27}$$

were implemented using the methods described in refs. [1, 2] this time, however, for a single-particle inclusive cross section. In the cases studied we found that the $\ln N/N$-effects were very small for the final state while for the initial state were, in general, appreciable. The combined $\ln N/N$-effect for both initial- and final state showed to be comparable with the NLL corrections. This leads us to conclude that further investigation of the the $\ln N/N$ is worth the effort.

Chapter 4 focussed on single-top production within the MC@NLO framework. First, general Monte Carlo methods were introduced and described followed by an example that illustrates what the challenges are when merging a higher order cross section with a Monte Carlo Shower.

Chapter 5 described the inclusion of angular correlations, which have their origin from production spin correlations in Monte Carlo event generators. These correlations have been implemented in MC@NLO for WW, $t\bar{t}$ and single-top hadroproduction and leptonic decay, and are very important for experimental analysis.

In chapter 6 we discussed the calculation of QCD corrections to the Wt production mode. We concentrated on the aspects that distinguish this production mode from the s and t channel modes, which were described in chapters 4 and 5. In particular, the inclusion of the Wt production in the MC@NLO framework finalizes the inclusion of the major single top quark production modes in this framework.

The work described in the last three chapters completes what is a very accurate description of single-top production, which, I believe, will be of great value to both the ATLAS and CMS experiments at the LHC.

Appendix A

Exponents and Constants

Here we list the exponents used in section 2.2. The initial state exponents (2.17) involve

$$h_a^{(0)}(\beta) = \frac{A_a^{(1)}}{2\pi b_0^2}\left[2\beta + \ln(1-2\beta)\right], \tag{A.1}$$

$$\begin{aligned} h_a^{(1)}(\beta,Q,\mu) &= \frac{A_a^{(1)} b_1}{2\pi b_0^3}\left[\frac{1}{2}\ln^2(1-2\beta) + \frac{2\beta+\ln(1-2\beta)}{1-2\beta}\right] + \frac{B_a^{(1)}}{\pi b_0}\ln(1-2\beta) \\ &+ \frac{1}{2\pi b_0}\left[A_a^{(1)}\ln\left(\frac{Q^2}{\mu^2}\right) - \frac{A_a^{(2)}}{\pi b_0}\right]\left[\frac{2\beta}{1-2\beta} + \ln(1-2\beta)\right]. \end{aligned} \tag{A.2}$$

Here

$$A_a^{(1)} = C_a, \qquad A_a^{(2)} = \tfrac{1}{2}C_a\left[C_A\left(\frac{67}{18} - \frac{\pi^2}{6}\right) - \frac{10}{9}T_R N_F\right] \tag{A.3}$$

where $C_q = C_F$ and $C_g = C_A$. Also

$$B_q^{(1)} = -\frac{3}{4}C_F, \qquad B_g^{(1)} = -\pi b_0\,. \tag{A.4}$$

The final state exponents (2.6) involve the functions

$$f_a^{(1)} = -\frac{A_a^{(1)}}{2\pi b_0 \lambda}[(1-2\lambda)\ln(1-2\lambda) - 2(1-\lambda)\ln(1-\lambda)] \tag{A.5}$$

$$\begin{aligned} f_a^{(2)} &= -\frac{A_a^{(1)} b_1}{2\pi b_0^3}[\ln(1-2\lambda) - 2\ln(1-\lambda) + \frac{1}{2}\ln^2(1-2\lambda) - \ln^2(1-\lambda)] \\ &+ \frac{B_a^{(1)}}{\pi b_0}\ln(1-\lambda) - \frac{A_a^{(1)}\gamma_E}{\pi b_0}[\ln(1-\lambda) - \ln(1-2\lambda)] - \frac{A_a^{(2)}}{2\pi^2 b_0^2}[2\ln(1-\lambda) - \ln(1-2\lambda)] \\ &+ \frac{A_a^{(1)}}{2\pi b_0}[2\ln(1-\lambda) - \ln(1-2\lambda)]\ln\frac{Q^2}{\mu^2} \end{aligned} \tag{A.6}$$

The wide-angle soft radiation exponents (2.13) are

$$g^{(1)}_{q\bar{q}g}(\lambda) = -\frac{C_A}{\pi b_0}\ln(1-2\lambda)\ln 2, \qquad g^{(1)}_{qgq}(\lambda) = -\frac{C_F}{\pi b_0}\ln(1-2\lambda)\ln 2 \tag{A.7}$$

In these equations

$$b_0 \;=\; \frac{11C_A - 4T_R N_F}{12\pi} \quad , \quad b_1 \;=\; \frac{17C_A^2 - 10C_A T_R N_F - 6C_F T_R N_F}{24\pi^2}\,. \tag{A.8}$$

where $T_R = 1/2$. These expressions are obtained by expanding the perturbative functions $A_a(\alpha_s)$, $B_d(\alpha_s)$ and $D_{ab\to d\gamma}$ in powers of α_s ,

$$A_a(\alpha_s) = \frac{\alpha_s}{\pi}A_a^{(1)} + \left(\frac{\alpha_s}{\pi}\right)^2 A_a^{(2)} + O(\alpha_s^3) \tag{A.9}$$

and so on.

Finally, the explicit forms of $C^{(ij\to\gamma k)}$ [3, 4] are

$$C^{q\bar{q}\to\gamma g} = 1 + \frac{\alpha_s}{\pi}\Bigg[-\frac{1}{2}(2C_F - C_A)\ln 2 + \frac{1}{2}K - K_q + 2\zeta(2)(2C_F - \frac{1}{2}C_A) \tag{A.10}$$

$$+ \frac{5}{4}(2C_F - \frac{1}{2}C_A)\ln^2 2 + \frac{3}{2}C_F(-\ln 2) - \pi b_0 \ln\frac{2p_T^2}{\mu^2}\Bigg] \tag{A.11}$$

$$C^{qg\to\gamma q} = 1 + \frac{\alpha_s}{\pi}\Bigg[-\frac{1}{10}(C_F - 2C_A)\ln 2 - \frac{1}{2}K_q + \frac{\zeta(2)}{10}(2C_F + 19C_A) \tag{A.12}$$

$$+ \frac{1}{2}C_F\ln^2 2 + \frac{3}{4}(C_F + \pi b_0)(-\ln 2) - \pi b_0 \ln\frac{2p_T^2}{\mu^2}\Bigg] \tag{A.13}$$

where

$$K = C_A\left(\frac{67}{18} - \frac{\pi^2}{6}\right) - \frac{10}{9}T_R N_F \qquad K_q = \left(\frac{7}{2} - \frac{\pi^2}{6}\right)C_F \tag{A.14}$$

We note that there is no factorization scale dependence in $h_a^{(1)}$ and the coefficient functions in Eq. (A.10) because of complete evolution from scale μ_F to Q/χ in Eqs. (2.21),(2.22) and (2.23).

Appendix B

Kinematics

In this section, we generalize the results of sect. 4 of **II** by considering the case of two final-state partons with unequal masses. Consistently with **II**, we use unbarred and barred symbols to denote quantities relevant to $2 \to 3$ and $2 \to 2$ processes respectively (see e.g. eqs. (6.18) and (4.41) for four-momentum assignments). Although in single-t production one of the final-state partons in $2 \to 2$ processes is massless, we shall derive our results in the most general case

$$\mathbf{k}_1^2 = m_1^2\,, \qquad \mathbf{k}_2^2 = m_2^2\,. \tag{B.1}$$

We start by defining the $2 \to 2$ reduced invariants as follows

$$\bar{s}_L = 2\mathbf{p}_1 \cdot \mathbf{p}_2\,, \qquad \bar{t}_L = -2\mathbf{p}_1 \cdot \mathbf{k}_1\,, \qquad \bar{u}_L = -2\mathbf{p}_1 \cdot \mathbf{k}_2\,, \tag{B.2}$$

with $L = +, -, f_1, f_2$. These invariants are used in the computations of the Born cross sections which appear in the MC cross sections expanded to NLO, hence the dependence on the branching leg L in eq. (B.2). We also get

$$-2\mathbf{p}_2 \cdot \mathbf{k}_2 = \bar{t}_L + \Delta m_{12}^2\,, \qquad -2\mathbf{p}_2 \cdot \mathbf{k}_1 = \bar{u}_L - \Delta m_{12}^2\,, \tag{B.3}$$

where $\Delta m_{12}^2 = m_1^2 - m_2^2$. As discussed in **II**, the $2 \to 2$ reduced invariants are functions of the invariants relevant to the $2 \to 3$ kinematics. The computations required to determine such functions are non-trivial; we only report the results

here:

$$\bar{s}_{\pm} = s + v_1 + v_2\,, \tag{B.4}$$

$$\bar{s}_{f_{1,2}} = s\,, \tag{B.5}$$

$$\bar{t}_{\pm} = -\frac{\bar{s}_{\pm}}{2}\left[1 - \frac{x_2(t_1-u_1)+x_1(t_2-u_2)}{2s\sqrt{x_+^2 - x_1x_2v_1v_2/s^2}}\right] - \frac{\Delta m_{12}^2}{2}\left(1 + \frac{x_-}{\sqrt{x_+^2 - x_1x_2v_1v_2/s^2}}\right), \tag{B.6}$$

$$\bar{t}_{f_1} = -\frac{1}{2}s\left[1 - \left(\frac{t_2-u_1}{s-w_1}\right)\frac{\bar{\beta}}{\beta_2}\right] - \frac{1}{2}\Delta m_{12}^2\,, \tag{B.7}$$

$$\bar{t}_{f_2} = -\frac{1}{2}s\left[1 - \left(\frac{t_1-u_2}{s-w_2}\right)\frac{\bar{\beta}}{\beta_1}\right] - \frac{1}{2}\Delta m_{12}^2\,, \tag{B.8}$$

$$\bar{u}_{\pm} = -\bar{s}_{\pm} - \bar{t}_{\pm}\,, \qquad \bar{u}_{f_{1,2}} = -s - \bar{t}_{f_{1,2}}\,, \tag{B.9}$$

where

$$\bar{\beta} = \sqrt{1 - 2\frac{\Sigma m_{12}^2}{\bar{s}} + \frac{\left(\Delta m_{12}^2\right)^2}{\bar{s}^2}}\,, \tag{B.10}$$

$$\beta_1 = \sqrt{\left(1 + \frac{\Delta m_{12}^2}{s-w_2}\right)^2 - \frac{4sm_1^2}{(s-w_2)^2}}\,, \tag{B.11}$$

$$\beta_2 = \sqrt{\left(1 - \frac{\Delta m_{12}^2}{s-w_1}\right)^2 - \frac{4sm_2^2}{(s-w_1)^2}}\,, \tag{B.12}$$

and $\Sigma m_{12}^2 = m_1^2 + m_2^2$. The $2 \to 3$ invariants that appear on the r.h.s. of eqs. (B.4)–(B.9) are labelled as in **II**; their definitions are also reported here in table B.1. Equations (B.2)–(B.12) give sufficient information, with tables 4.1–4.3, to compute the shower scales to be used in eqs. (4.39) and (4.40).

We finally summarize the formulae for HERWIG showering variables. The case of initial-state emissions is identical to that studied in **II**, the condition $m_1 \neq m_2$ being irrelevant here. When parton 1 branches, the showering variables z_+ and ξ_+ are related to the invariants as in eqn. (**II**.4.31) and eqn. (**II**.4.32):

$$v_1 = -2\frac{1-z_+}{z_+^2}\xi_+ E_0^2\,, \tag{B.13}$$

$$-\frac{v_2}{s} = \frac{1}{2}(1-z_+)(2-\xi_+)\,. \tag{B.14}$$

Label	Invariant	Relation
s	$2p_1 \cdot p_2$	
t_1	$-2p_1 \cdot k_1$	
t_2	$-2p_2 \cdot k_2$	
u_1	$-2p_1 \cdot k_2$	
u_2	$-2p_2 \cdot k_1$	
v_1	$-2p_1 \cdot k_3$	$-s - t_1 - u_1$
v_2	$-2p_2 \cdot k_3$	$-s - t_2 - u_2$
w_1	$2k_1 \cdot k_3$	$s + t_2 + u_1 - m_1^2 + m_2^2$
w_2	$2k_2 \cdot k_3$	$s + t_1 + u_2 + m_1^2 - m_2^2$
M_{12}^2	$(k_1 + k_2)^2$	$s + v_1 + v_2$

Table B.1: Notation for $2 \to 3$ kinematics.

Using eq. (4.34) we can write the solutions explicitly:

$$z_+^{(l)} = \frac{2|\bar{l}|}{v_1}\left[1 - \sqrt{1 - \frac{v_1}{|\bar{l}|}\left(1 + \frac{v_2}{s}\right)}\right], \tag{B.15}$$

$$\xi_+^{(l)} = 2\left[1 + \frac{v_2}{s(1 - z_+^{(l)})}\right], \tag{B.16}$$

which are identical to eqn. (**II**.4.33) and eqn. (**II**.4.34) except for the different definition of the scale $\bar{l}$.

The branching of parton 2 will be described in terms of the variables z_- and ξ_-; these can be obtained from eqs. (B.13)–(B.16) by interchanging variables v_1 and v_2.

The formulae for final-state emissions are affected by the condition $m_1 \neq m_2$. When the parton with momentum k_1 branches, eqn. (**II**.4.23) and eqn. (**II**.4.24) still formally hold

$$w_1 = 2z_{f_1}(1 - z_{f_1})\xi_{f_1}E_0^2\,, \tag{B.17}$$

$$\zeta_{f_1} = (1 - z_{f_1})\frac{1 + (1 - z_{f_1}\xi_{f_1})/\tilde{\beta}_1}{1 + \tilde{\beta}_1}\,, \tag{B.18}$$

with

$$\tilde{\beta}_1 = \sqrt{1 - (w_1 + m_1^2)/E_0^2}\,, \tag{B.19}$$

$$\zeta_{f_1} = \frac{(2s - (s - w_1)\varepsilon_2)w_2 + (s - w_1)\left[(w_1 + w_2)\beta_2 - \varepsilon_2 w_1\right]}{(s - w_1)\beta_2\left[2s - (s - w_1)\varepsilon_2 + (s - w_1)\beta_2\right]}\,, \tag{B.20}$$

$$\varepsilon_2 = 1 - \frac{\Delta m_{12}^2}{s - w_1}\,. \tag{B.21}$$

It is apparent that eq. (B.20) coincides with eqn. (**II**.4.27) when $m_1 = m_2$ (i.e. $\varepsilon_2 = 1$). Solving eqs. (B.19) and (B.20) we obtain

$$z_{f_1}^{(l)} = 1 - \tilde{\beta}_1 \zeta_{f_1} - \frac{w_1}{2(1+\tilde{\beta}_1)|\bar{l}|}\,, \tag{B.22}$$

$$\xi_{f_1}^{(l)} = \frac{w_1}{2z_{f_1}^{(l)}(1-z_{f_1}^{(l)})|\bar{l}|}\,, \tag{B.23}$$

which are identical to eqn. (**II**.4.28) and eqn. (**II**.4.29) except for the different definition of the scale $\bar{l}$.

The branching of the parton with momentum k_2 can be treated along the same lines. The showering variables $z_{f_2}^{(l)}$ and $\xi_{f_2}^{(l)}$ will be obtained from eqs. (B.22) and (B.23) by formally interchanging labels 1 and 2. Note that in this way the quantity ε_1 appears in the expression for ζ_{f_2}, and

$$\varepsilon_1 = 1 + \frac{\Delta m_{12}^2}{s - w_2}\,. \tag{B.24}$$

Appendix C

MC subtraction terms

In this section, we construct explicitly the MC subtraction terms for single-t production, expressing them in terms of the variables used in the NLO computation. In order to do this, we start by introducing the phase-space parametrizations used in ref. [5] to deal with initial- and final-state emissions; in both cases, we integrate out the trivial azimuthal angles. We have

$$d\phi_3^{(\text{IN})} = \frac{s}{1024\pi^4}\,\bar{\beta}\left((1-\xi_i)s\right)\,\xi_i\,d\xi_i dy_i d\cos\theta d\varphi\,, \tag{C.1}$$

$$d\phi_3^{(\text{OUT})} = \frac{s}{512\pi^4}\,\frac{\xi_j}{2-\xi_i(1-y_j)}\,\xi_i\,d\xi_i dy_i dy_j d\varphi_j\,, \tag{C.2}$$

where $\bar{\beta}(s)$ is given in eq. (B.10), and[1]

$$\xi_j = \frac{2(1-m_1^2/s-\xi_i)}{2-\xi_i(1-y_j)}\,. \tag{C.3}$$

The variables labelled with index i refer to the FKS parton (see eqn. (**FKS**.4.3)), and those labelled with index j refer to the massless final-state parton that can become collinear to the FKS parton (see eqn. (**FKS**.4.57)). Note that ξ_i is related to the variable x used in **I** and **II** by the following equation

$$x \equiv 1-\xi_i\,. \tag{C.4}$$

This implies that eq. (C.1) coincides with eqn. (**II**.B.22). We rewrite the real-emission finite contributions to the single-t cross section (eqn. (**FKS**.4.37) and eqn. (**FKS**.4.65)) as follows:

$$d\sigma_i^{(in,f)} = \tfrac{1}{2}\left(\tfrac{1}{\xi_i}\right)_c\left[\left(\tfrac{1}{1-y_i}\right)_\delta + \left(\tfrac{1}{1+y_i}\right)_\delta\right]\left((1-y_i^2)\xi_i^2\mathcal{M}^{(r)}\right)\mathcal{S}_i^{(0)}\,d\tilde{\phi}_3^{(\text{IN})}\,, \tag{C.5}$$

$$d\sigma_{ij}^{(out,f)} = \left(\tfrac{1}{\xi_i}\right)_c\left(\tfrac{1}{1-y_j}\right)_\delta\left((1-y_j)\xi_i^2\mathcal{M}^{(r)}\right)\mathcal{S}_{ij}^{(1)}\,d\tilde{\phi}_3^{(\text{OUT})}\,, \tag{C.6}$$

[1] Since this section is specific to single-t production, we set $m_2 = 0$ here.

where

$$d\phi_3^{(\rm IN)} = \xi_i \, d\tilde{\phi}_3^{(\rm IN)} , \qquad d\phi_3^{(\rm OUT)} = \xi_i \, d\tilde{\phi}_3^{(\rm OUT)} . \tag{C.7}$$

As discussed in **I** and **II**, MC subtraction terms can be obtained from the MC cross sections expanded to NLO. Thus, following eqn. (**II**.B.21), in order to construct them we must write eq. (4.39) in the same form as eq. (C.5) (after relabeling), and eq. (4.40) in the same form as eq. (C.6) (after relabeling). In order to do this, we note that the Born cross sections that appear in the MC subtraction terms have the following forms (in order to simplify the notation, we neglect here most of the indices)

$$d\bar{\sigma} = \mathcal{M}^{(b)}(\bar{s}_\pm, \bar{t}_\pm) \, \frac{\bar{\beta}(\bar{s}_\pm)}{16\pi} \, d\cos\theta_{in} , \tag{C.8}$$

$$d\bar{\sigma} = \mathcal{M}^{(b)}(\bar{s}_{f_\alpha}, \bar{t}_{f_\alpha}) \, \frac{\bar{\beta}(\bar{s}_{f_\alpha})}{16\pi} \, d\cos\theta_{out} , \tag{C.9}$$

for initial- and final-state branchings respectively. Here $\mathcal{M}^{(b)}$ is the Born matrix element, and the angles θ_{in} and θ_{out} have been introduced in eqn. (**II**.B.32) and eqn. (**II**.B.33) respectively. As discussed in **II**, it is not restrictive to obtain these scattering angles in the zero-angle-emission limits, which leads to

$$\theta_{in} = \theta , \qquad \theta_{out} = y_j , \tag{C.10}$$

where θ and y_j are integration variables in eqs. (C.1) and (C.2) respectively. The first relation in eq. (C.10) coincides with eqn. (**II**.B.35). We also note that, in the zero-angle-emission limits, the (trivial) azimuthal angles generated by the showers can be chosen to coincide with the angles φ and φ_j of eqs. (C.1) and (C.2) for initial- and final-state branchings respectively. We shall therefore insert the factors $d\varphi/(2\pi)$ and $d\varphi_j/(2\pi)$ in eqs. (4.39) and (4.40). We rewrite eq. (4.39) as follows

$$\begin{aligned} d\hat{\sigma}^{(\pm)}\Big|_{\rm MC} &= \frac{1}{(1-y_i^2)\xi_i} (1-y_i^2)\xi_i \, \frac{g_{\rm S}^2}{256\pi^4} \, \frac{P(z_\pm)}{\xi_\pm} \, \frac{\partial(\xi_\pm, z_\pm)}{\partial(\xi_i, y_i)} \\ &\times \mathcal{M}^{(b)}(\bar{s}_\pm, \bar{t}_\pm) \, \Theta\left((z_\pm^{(l)})^2 - \xi_\pm^{(l)}\right) \bar{\beta}(\bar{s}_\pm) \, d\xi_i dy_i d\cos\theta d\varphi , \end{aligned} \tag{C.11}$$

where the first factor on the r.h.s. matches the "event" part of eq. (C.5), i.e. that obtained by replacing the distributions with ordinary functions. Using eqs. (C.1) and (B.4), we get

$$\bar{\beta}(\bar{s}_\pm) d\xi_i dy_i d\cos\theta d\varphi = \frac{1024\pi^4}{s} d\tilde{\phi}_3^{(\rm IN)} . \tag{C.12}$$

Therefore

$$d\hat{\sigma}^{(\pm)}\Big|_{\rm MC} = \frac{1}{2\xi_i}\left[\frac{1}{1-y_i}+\frac{1}{1+y_i}\right]\left((1-y_i^2)\xi_i^2\frac{d\Sigma^{(L=\pm)}}{d\phi_3^{(\rm IN)}}\Big|_{\rm MC}\right)d\tilde{\phi}_3^{(\rm IN)}\,, \tag{C.13}$$

$$\frac{d\Sigma^{(L=\pm)}}{d\phi_3^{(\rm IN)}}\Big|_{\rm MC} = \frac{4g_{\rm S}^2}{s}\frac{P(z_\pm)}{\xi_i\xi_\pm}\frac{\partial(\xi_\pm,z_\pm)}{\partial(\xi_i,y_i)}\,\mathcal{M}^{(b)}(\bar{s}_\pm,\bar{t}_\pm)\,\Theta\left((z_\pm^{(l)})^2-\xi_\pm^{(l)}\right), \tag{C.14}$$

which is identical (up to notational differences) to eqn. (**I**.A.72) and eqn. (**I**.A.73). The MC subtraction terms that enter eq. (4.43) are readily obtained from eq. (C.14) using eqn. (**I**.4.18):

$$\frac{d\overline{\Sigma}^{(L=\pm)}}{d\phi_3^{(\rm IN)}}\Big|_{\rm MC} = \frac{\partial(\bar{x}_{1i},\bar{x}_{2i})}{\partial(x_1,x_2)}\frac{d\Sigma^{(L=\pm)}}{d\phi_3^{(\rm IN)}}\Big|_{\rm MC}\,. \tag{C.15}$$

The reduced Bjorken x's $\bar{x}_{1i}$ and $\bar{x}_{2i}$ are given in eqn. (**II**.4.20) or eqn. (**II**.4.22).

We now turn to the case of final-state emissions, and we rewrite eq. (4.40) as follows

$$\begin{aligned} d\hat{\sigma}^{(f_\alpha)}\Big|_{\rm MC} &= \frac{1}{(1-y_j)\xi_i}(1-y_j)\xi_i\,\frac{g_{\rm S}^2}{256\pi^4}\,\frac{P(z_{f_\alpha})}{\xi_{f_\alpha}}\,\frac{\partial(\xi_{f_\alpha},z_{f_\alpha})}{\partial(\xi_i,y_j)}\,\mathcal{M}^{(b)}(\bar{s}_{f_\alpha},\bar{t}_{f_\alpha}) \\ &\times\ \Theta\left(1-\xi_{f_\alpha}^{(l)}\right)\Theta\left(z_{f_\alpha}^{(l)}-\frac{m_\alpha}{E_0\sqrt{\xi_{f_\alpha}^{(l)}}}\right)\bar{\beta}(\bar{s}_{f_\alpha})\,d\xi_i dy_i dy_j d\varphi_j\,. \end{aligned} \tag{C.16}$$

Using eq. (C.2) we get

$$d\xi_i dy_i dy_j d\varphi_j = \frac{512\pi^4}{s}\,\frac{2-\xi_i(1-y_j)}{\xi_j}\,d\tilde{\phi}_3^{(\rm OUT)}\,. \tag{C.17}$$

Inserting this equation into eq. (C.16), and using eq. (B.5) we obtain

$$d\hat{\sigma}^{(f_\alpha)}\Big|_{\rm MC} = \frac{1}{\xi_i}\frac{1}{1-y_j}\left((1-y_j)\xi_i^2\frac{d\overline{\Sigma}^{(L=f_\alpha)}}{d\phi_3^{(\rm OUT)}}\right)d\tilde{\phi}_3^{(\rm OUT)}\,, \tag{C.18}$$

$$\begin{aligned} \frac{d\overline{\Sigma}^{(L=f_\alpha)}}{d\phi_3^{(\rm OUT)}} &= \frac{2g_{\rm S}^2}{s}\,\frac{2-\xi_i(1-y_j)}{\xi_i\xi_j}\,\bar{\beta}(s)\,\frac{P(z_{f_\alpha})}{\xi_{f_\alpha}}\,\frac{\partial(\xi_{f_\alpha},z_{f_\alpha})}{\partial(\xi_i,y_j)}\,\mathcal{M}^{(b)}(s,\bar{t}_{f_\alpha}) \\ &\times\ \Theta\left(1-\xi_{f_\alpha}^{(l)}\right)\Theta\left(z_{f_\alpha}^{(l)}-\frac{m_\alpha}{E_0\sqrt{\xi_{f_\alpha}^{(l)}}}\right). \end{aligned} \tag{C.19}$$

Note that we directly defined $\overline{\Sigma}$ (rather than Σ as in eq. (C.13)) thanks to eqn. (**II**.4.7).

We have checked analytically that the MC counterterms introduced above locally cancel the collinear divergences of the real matrix elements. As already discussed in **I** and **II**, this happens in the soft limit only after angular integration. We therefore adopt here the same solutions as in eqn. (**II**.B.43). As in the previous cases, we checked that the parametric dependence introduced in this way is totally negligible, as we expect from power-suppressed effects.

Appendix D

Upper bounds in vector boson production

In this appendix, we present an alternative derivation of eq. (5.31). One introduces the quantity

$$N^\nu \equiv M^\mu \frac{i}{q^2 - m_V^2 + i m_V \Gamma_V} \left(-g_\mu{}^\nu + \frac{q_\mu q^\nu}{m_V^2} \right) , \tag{D.1}$$

with which eq. (5.18) becomes

$$\sum_{\text{spins}} |A|^2 = F_V^2 \, \mathrm{Tr}\left[\left(V_{Vl}^2 + A_{Vl}^2 - 2 V_{Vl} A_{Vl} \gamma_5 \right) \not{k}_1 \not{N} \not{k}_2 \not{N}^* \right] . \tag{D.2}$$

Evaluating this in the rest-frame of the (virtual) vector boson, with the z-axis along the direction of the lepton 3-momentum, we find

$$\sum_{\text{spins}} |A|^2 = 2 q^2 F_V^2 \, \left[\left(V_{Vl}^2 + A_{Vl}^2 \right) \left(N^1 N^{1*} + N^2 N^{2*} \right) + 4 V_{Vl} A_{Vl} \, \mathrm{Im} \left(N^1 N^{2*} \right) \right] . \tag{D.3}$$

To establish an upper bound on this quantity, we note that

$$2 \left| \mathrm{Im} \left(N^1 N^{2*} \right) \right| \leq 2 \left| N^1 \right| \left| N^2 \right| \leq N^1 N^{1*} + N^2 N^{2*} \tag{D.4}$$

and so

$$\begin{aligned} \sum_{\text{spins}} |A|^2 &\leq 2 q^2 F_V^2 \, \left(|V_{Vl}| + |A_{Vl}| \right)^2 \left(N^1 N^{1*} + N^2 N^{2*} \right) \\ &= \frac{2 q^2 F_V^2 \, \left(|V_{Vl}| + |A_{Vl}| \right)^2}{(q^2 - m_V^2)^2 + (m_V \Gamma_V)^2} \left(M^1 M^{1*} + M^2 M^{2*} \right) . \end{aligned} \tag{D.5}$$

Note that $M^{1,2}$ in this expression are strictly off-mass-shell quantities: no on-shell approximations have been made at this stage.

Now consider the production of a stable vector boson of mass m_V. Denoting the amplitude for this by $\bar{A}$, we have (again in the vector boson rest frame)

$$\begin{aligned}\sum_{\text{spins}} \left|\bar{A}\right|^2 &= \bar{M}^\mu \bar{M}^\nu \left(-g_{\mu\nu} + \frac{q_\mu q_\nu}{m_V^2}\right)_{q^2=m_V^2} \\ &= \bar{M}^1 \bar{M}^{1*} + \bar{M}^2 \bar{M}^{2*} + \bar{M}^3 \bar{M}^{3*} \end{aligned} \tag{D.6}$$

where $\bar{M}^\mu$ denotes the on-mass-shell value of M^μ. Therefore, as long as

$$M^1 M^{1*} + M^2 M^{2*} \leq \bar{M}^1 \bar{M}^{1*} + \bar{M}^2 \bar{M}^{2*} + \bar{M}^3 \bar{M}^{3*} \tag{D.7}$$

we have

$$\sum_{\text{spins}} |A|^2 \leq \frac{2q^2 F_V^2 \left(|V_{Vl}| + |A_{Vl}|\right)^2}{(q^2 - m_V^2)^2 + (m_V \Gamma_V)^2} \sum_{\text{spins}} \left|\bar{A}\right|^2 \tag{D.8}$$

and hence

$$\frac{d\sigma_{l\bar{l}}}{d\Phi_{2+1^\star}} \leq \frac{2q^2 F_V^2 \left(|V_{Vl}| + |A_{Vl}|\right)^2}{(q^2 - m_V^2)^2 + (m_V \Gamma_V)^2} \frac{d\sigma_V}{d\Phi_{1+1^\star}} \,, \tag{D.9}$$

which is identical to eq. (5.31), given the fact that $V_{Vl} A_{Vl} > 0$, and that both equations are valid on-shell.

Clearly, one may check whether the bounds given in eqs. (5.31) and (D.9) are not violated in the case of off-shell vector bosons. This is indeed the case, provided that the off-shellness is not too large or too small (typically, this happens within $\pm 30 \Gamma_V$ of the pole mass). A good strategy is that of using eq. (5.31) for $q^2 < m_V^2$, and eq. (D.9) for $q^2 > m_V^2$. However, one should bear in mind that in the case of off-shell particles the values of Bjorken x's, and hence of the PDFs, may change, thus potentially affecting the bound.

Appendix E

Calculation of $\tilde{\mathcal{M}}$ in the Helicity Formalism

In this appendix we calculate the interference term

$$\tilde{\mathcal{M}} = 2\,\mathrm{Re}\left[\mathcal{A}_+^\dagger \mathcal{A}_-\right], \tag{E.1}$$

that is necessary for proper numerical sampling of the initial state collinear regions. We have dropped the superscript (0) compared to eqn. (6.16) for brevity.

We shall use helicity methods [cite]. The relevant diagrams are illustrated in figure E.1. As well as the null momenta p_1 and p_2, we define the further null vector:

$$p_5 = p_4 - \frac{m^2}{t_1} p_2, \tag{E.2}$$

where $t_1 = t - m^2 = (p_2 + p_4)^2 - m^2$. We also adopt the common notation:

$$|k^\pm\rangle \equiv u_\pm(k), \quad \langle k^\pm| \equiv \bar{u}_\pm(k) \tag{E.3}$$

for massless quark spinors. Then the propagator for t-channel graphs is:

$$\frac{i}{t_1}(\not{p}_2 + \not{p}_4) = \frac{i}{t_1}\left[\frac{t}{t_1}\,\not{p}_2 + \not{p}_5\right] \tag{E.4}$$

$$= \frac{i}{t_1}\left[\frac{t}{t_1}\left(|2+\rangle\langle 2-| + |2-\rangle\langle 2-|\right) + |5+\rangle\langle 5+| + |5-\rangle\langle 5-|\right], \tag{E.5}$$

using completeness relations for the slashed momenta. We also define the Mandelstam invariants:

$$s = (p_1 + p_2)^2; \quad u = (p_1 + p_4)^2. \tag{E.6}$$

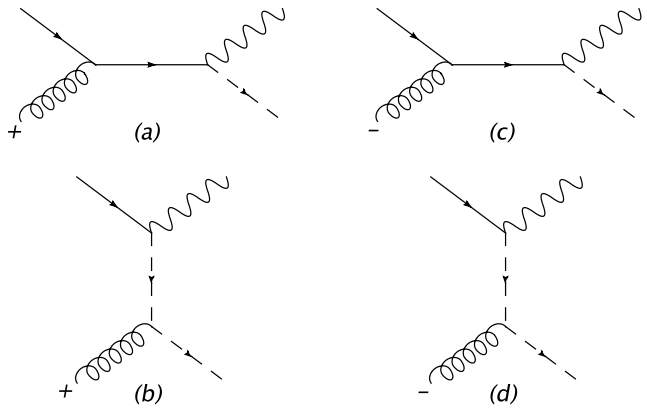

Figure E.1: Diagrams used in the calculation of $2\,\mathrm{Re}\left[\mathcal{A}_+^\dagger \mathcal{A}_-\right]$ for $b(p_1) + g(p_2) \to W^-(p_3) + t(p_4)$, where all momenta are defined to be outgoing.

The positive helicity diagrams (denoted (a) and (b) respectively in figure E.1) are then given by (neglecting coupling factors):

$$\mathcal{A}_+^{(s)} = -\frac{2i\sqrt{2}}{s\langle 12\rangle}\epsilon_\mu(p_3)\bar{u}(p_4)\gamma^\mu|2-\rangle\langle 21\rangle\langle 2+|u(p_1); \tag{E.7}$$

$$\mathcal{A}_+^{(t)} = \frac{2i\sqrt{2}}{t_1\langle 12\rangle}\epsilon_\mu(p_3)\bar{u}(p_4)\left[|1+\rangle[25]\langle 5-| + m|2-\rangle\langle 1-|\right]\gamma^\mu u(p_1), \tag{E.8}$$

where $\epsilon_\mu(p_3)$ is the polarisation vector of the W boson, and we have used the standard notation:

$$[ij] = \langle i+|j-\rangle, \quad \langle ij\rangle = \langle i-|j+\rangle. \tag{E.9}$$

In deriving equations (E.7,E.8) we have used the following expressions for the gluon polarisation vectors:

$$\epsilon_{+,\mu}(p_2,q) = \frac{\langle q-|\gamma_\mu|2-\rangle}{\sqrt{2}\langle q2\rangle}, \quad \epsilon_{-,\mu}(p_2,q) = \frac{\langle q+|\gamma_\mu|2+\rangle}{\sqrt{2}\langle [2q]\rangle}. \tag{E.10}$$

Here q is an arbitrary null reference momentum, which has been set to p_1. One is in principle able to choose a different reference momentum for the negative helicity diagrams, owing to the fact that helicity amplitudes are separately gauge invariant. However, if one also chooses $q_2 = p_1$ in the negative helicity case then diagram (c) in figure E.1 vanishes. This relies on the helicity of the light quark line being fixed by the chiral boson coupling. Then the negative helicity amplitude is given solely

by diagram (d):

$$\mathcal{A}_- = \frac{2i\sqrt{2}}{t_1[21]}\epsilon_\mu(p_3)\bar{u}(p_4)\left[\frac{t}{t_1}|2+\rangle[12]\langle 2-| + |2+\rangle[15]\langle 5-| + m|1-\rangle\langle 2-|\right]\gamma^\mu u(p_1). \tag{E.11}$$

To evaluate squared amplitudes one needs the following dot products (where $(ij) = 2p_i \cdot p_j$):

$$(13) = t - M_W^2; \tag{E.12}$$
$$(24) = t_1; \tag{E.13}$$
$$(34) = s - m^2 - M_W^2; \tag{E.14}$$
$$(23) = -s - t_1; \tag{E.15}$$
$$(14) = -s - t + M_W^2; \tag{E.16}$$
$$(15) = -\frac{ts}{t_1} - t + M_W^2; \tag{E.17}$$
$$(25) = t_1; \tag{E.18}$$
$$(35) = \frac{ts}{t_1} - M_W^2. \tag{E.19}$$

It can be checked that $|\mathcal{A}_+|^2 + |\mathcal{A}_-|^2$, after summing over the W boson and quark spins, is equal to the known Born result. For the helicity interference term we need:

$$\begin{aligned}\tilde{\mathcal{M}} &= 2\,\mathrm{Re}\left[\mathcal{A}_+^\dagger \mathcal{A}_-\right] \\ &= 2\,\mathrm{Re}\left[\mathcal{A}_+^{(s)\dagger}\mathcal{A}_- + \mathcal{A}_+^{(t)\dagger}\mathcal{A}_-\right].\end{aligned} \tag{E.20}$$

Using equations (E.7, E.8, E.11, E.12-E.19) one finds:

$$\mathcal{A}_+^{(s)\dagger}\mathcal{A}_- = \frac{8}{t_1}\frac{[15]^2\langle 25\rangle^2}{[12]^2}\left(2 + \frac{m^2}{M_W^2}\right); \tag{E.21}$$
$$\mathcal{A}_+^{(t)\dagger}\mathcal{A}_- = \frac{8}{t_1^2}\frac{[15]^2\langle 25\rangle^2}{[12]^2}\left\{2M_W^2 - 2t_1 + m^2\left[-1 - \frac{t_1}{M_W^2}\right] - \frac{m^4}{M_W^2}\right\}. \tag{E.22}$$

Putting things together:

$$\mathcal{A}_+^\dagger\mathcal{A}_- = \frac{8}{t_1^2 M_W^2}\frac{[15]^2\langle 25\rangle^2}{[12]^2}(M_W^2 - m^2)(2M_W^2 + m^2). \tag{E.23}$$

Note the presence of squared spinor products, which can not immediately be evaluated to form dot products. This is to be expected, given that $\tilde{\mathcal{M}}$ is not a Lorentz

invariant quantity. To evaluate the quantities in equation (E.23) one can parameterise 4-momenta in the centre of mass frame of the incoming particles as follows:

$$p_1 = \left(\frac{\sqrt{s}}{2}, 0, 0, \frac{\sqrt{s}}{2}\right); \tag{E.24}$$

$$p_2 = \left(\frac{\sqrt{s}}{2}, 0, 0, -\frac{\sqrt{s}}{2}\right); \tag{E.25}$$

$$p_5 = (E, E\sin\theta\cos\phi, E\sin\theta\sin\phi, E\cos\theta)\,. \tag{E.26}$$

Given equation (E.2) and the fact that p_1 and p_2 have no transverse components, we may interpret ϕ as the azimuthal scattering angle of the top quark (relative to the incoming particle axis) in this frame. Basis spinors satisfying the massless Dirac equation with conventional normalisation $u^\dagger(p_i)u(p_i) = 2p_i^0$ are (choosing arbitrary phases):

$$\begin{aligned} u_-(p_5) &= \begin{pmatrix} 0 \\ 0 \\ -\sqrt{E(1-\cos\theta)}e^{-i\phi} \\ \sqrt{E(1+\cos\theta)} \end{pmatrix}; \quad u_\lambda(p_1) = \begin{pmatrix} s^{\frac{1}{4}}\delta_{\lambda+} \\ 0 \\ 0 \\ s^{\frac{1}{4}}\delta_{\lambda-} \end{pmatrix}; \\ u_\lambda(p_2) &= \begin{pmatrix} 0 \\ s^{\frac{1}{4}}\delta_{\lambda+} \\ s^{\frac{1}{4}}\delta_{\lambda-} \\ 0 \end{pmatrix}, \end{aligned} \tag{E.27}$$

from which one finds:

$$2\,\mathrm{Re}\left\{[15]^2\langle 25\rangle^2\right\} = 2(15)(25)[2\cos^2\phi - 1]. \tag{E.28}$$

Combining this with equations (E.20, E.23, E.12-E.19) gives finally:

$$\tilde{\mathcal{M}} = \frac{16}{s\,t_1^2 M_W^2}(2\cos^2\phi - 1)(M_W^2 - m^2)(2M_W^2 + m^2)(M_W^2 m^2 - ut). \tag{E.29}$$

Appendix F

Wt production

In this appendix we demonstrate that the squared amplitudes for single top production with an associated W boson are independent of whether the final state top is a quark or antiquark.
Considering the squared amplitudes for Wt production, only interference terms can give rise to a difference between quark and antiquark amplitudes, as any amplitude squared with itself must give the same result if the charge conjugation operation is applied. Each interference diagram for Wt production has an open or closed fermion loop associated with the top quark (and the b quark from top decay). The replacement $t \to \bar{t}$ can affect the amplitude in two ways:

1. It changes the sign of all momenta which occur in uncut propagators along the top quark line[1]. If p_i are the propagating momenta, the fermion trace in each diagram will contain the following terms:

$$(p_1 - m)(p_2 - m)\dots(p_N - m), \tag{F.1}$$

where N is the number of uncut fermion momenta, and there may be additional Dirac matrices between the propagator factors. Interchanging top and antitop quarks results gives instead the terms:

$$(-p_1 - m)(-p_2 - m)\dots(-p_N - m) = (-1)^N(p_1 + m)(p_2 + m)\dots(p_N + m). \tag{F.2}$$

Given that the number of Dirac matrices in each interference graph is even, only terms involving an even number of masses survive. Then the amplitude for antiquark production is related to that for quark production via:

$$\begin{aligned}\mathcal{A}_{\bar{t}} &= C_{diag}\mathcal{A}_t \\ &= (-1)^N\mathcal{A}_t,\end{aligned} \tag{F.3}$$

[1]Cut propagators correspond to terms in the fermion trace of form $\not{p} \pm m$ depending on whether quark or antiquark spinors are involved i.e. the sign of the momentum is not changed.

where $\mathcal{A}_{t,\bar{t}}$ is the amplitude associated with a given interference diagram. Here C_{diag} is the parity under $t \to \bar{t}$ of the diagram i.e. $C_{diag} = \pm 1$.

2. The colour factor may be affected. In each of the diagrams for Wt production, one always has:
$$\mathcal{C}_{\bar{t}} = C_{col}\mathcal{C}_t, \tag{F.4}$$
where $\mathcal{C}_{t,\bar{t}}$ are the colour factors for the amplitude with a top and antitop quark respectively, and $C_{col} = \pm 1$.

The total parity under $t \to \bar{t}$ is then given by:

$$C = C_{diag}C_{col} = \pm 1. \tag{F.5}$$

There are, in total, 48 interference diagrams for Wt production at NLO. These can be subdivided into gg, bb, bg and $b\bar{b}$ initial states. Diagrams with other down-type quarks in the initial state form a subset of those already specified. The gg and $b\bar{b}$ diagrams are always associated with real emissions, and the relevant interference terms are depicted in figures F.1 and F.2. For the bb (and, hence, qq) initial state, there is only one Feynman amplitude and hence no interference term is possible. The qg initial states can be associated with real (figure F.3) or virtual (figure F.4) emissions. By evaluating the number of uncut fermion propagators and the colour factor for each graph, one can find its parity under $t \to \bar{t}$ using equation F.5.

Looking at the diagrams in figures F.1-F.4 one sees that they fall into two types:

1. Diagrams no triple gluon coupling. These all have symmetric colour factors under $t \to \bar{t}$, and an even number of uncut fermion propagators. Hence $C = 1$ for such graphs.

2. Diagrams with a triple gluon coupling. These all have antisymmetric colour factors, and an odd number of uncut fermion propagators (this latter fact can be easily appreciated by considering removing a gluon line from a fermion in graphs of type 1 and reattaching it to a gluon line). Hence $C = (-1)^2 = +1$ for these graphs.

As an example, consider the upper graph in figure F.4. This has 4 uncut fermion propagators and a colour factor $\mathrm{Tr}\,[t^b t^a t^b t^a]$, where a and b are the colours of the initial state and virtual gluons respectively. The corresponding antiquark diagram has the same colour factor, and thus one has $C_{diag} = C_{col} = C = 1$.

The diagram beneath this, however, has 3 uncut fermion propagators and hence $C_{diag} = -1$. The colour factor is $f^{abc}\mathrm{Tr}\,[t^c t^b t^a]$, where a denotes the initial state

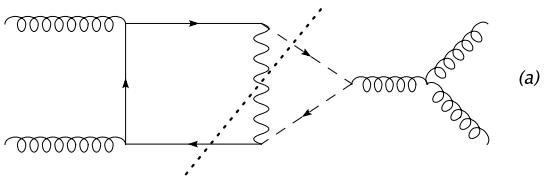

Figure F.1: Cut interference diagrams at NLO in Wt production, for gg initial states. Dashed lines represent the top quark, and the cuts are shown as short dashed lines.

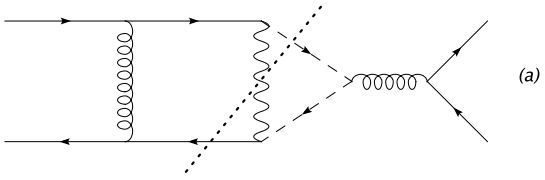

Figure F.2: Cut interference diagrams at NLO in Wt production, for $b\bar{b}$ initial states. Note that this includes $q\bar{q}$ initial states as a special case, where diagram (c) is the only one present. Dashed lines represent the top quark, and the cuts are shown as short dashed lines.

gluon and b and c the two virtual gluons. The antitop diagram has instead a colour factor $f^{abc}\mathrm{Tr}\left[t^a t^b t^c\right] = -f^{abc}\mathrm{Tr}\left[t^c t^b t^a\right]$, thus $C_{col} = -1$. Finally, one has $C = 1$ for the complete diagram including the colour factor.

In a similar fashion one finds that every graph is even upon replacing top quarks by antitop quarks, and so the total squared amplitude for Wt production is the same for both t and $\bar{t}$.

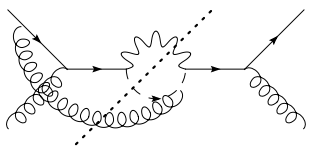

Figure F.3: Cut interference diagrams at NLO in Wt production, for qg initial states. Dashed lines represent the top quark, and the cuts are shown as short dashed lines.

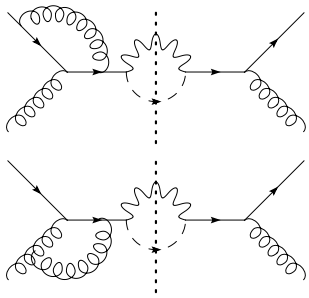

Figure F.4: Cut interference diagrams for virtual corrections to Wt production. Dashed lines represent the top quark, and the cuts are shown as short dashed lines.

References

[1] A. Kulesza, G. Sterman and W. Vogelsang, Phys. Rev. **D66**, 014011 (2002), [hep-ph/0202251].

[2] A. Kulesza, G. Sterman and W. Vogelsang, Phys. Rev. **D69**, 014012 (2004), [hep-ph/0309264].

[3] S. Catani, M. L. Mangano and P. Nason, JHEP **9807**, 024 (1998), [hep-ph/9806484].

[4] S. Catani, M. L. Mangano, P. Nason, C. Oleari and W. Vogelsang, JHEP **9903**, 025 (1999), [hep-ph/9903436].

[5] S. Frixione, Z. Kunszt and A. Signer, Nucl. Phys. **B467**, 399 (1996), [hep-ph/9512328].

Samenvatting

Aspecten van Perturbatieve QCD

Een "prompt" foton is een foton dat direkt gecreëerd wordt in botsingen tussen partonen. "Partonen" is de verzamelnaam voor de bestanddelen (quarks) van een proton of neutron, en de lijmdeeltjes (gluonen) die ze bij elkaar houden. Prompte fotonen zijn dus boodschappers van de quark-gluon dynamica, zoals beschreven door de Quantum Chromodynamica (QCD) theorie, die plaatsvindt wanneer twee nucleonen op elkaar botsen. Dat betekent o.a. dat wij door het bestuderen van zulke prompte fotonen informatie kunnen verkrijgen over de parton verdeling binnen een proton. In zulke studies is het van belang om effekten van van lage-energie (zachte) gluonen mee te nemen.

Prompt photon produktie kan ook beschouwd worden als een relatief eenvoudige, theoretische proeftuin voor het beschrijven van de QCD dynamica van $2 \to 2$ processen. Een prompt photon moet namelijk geproduceerd worden tegelijk met een parton, vanwegen impulsbehoud. Een belangrijke reden dat prompte fotonen zo geschikt zijn als boodschappers van QCD dynamica, is dat ze na produktie geen verandering meer ondergaan, in tegenstelling tot partonen, die veranderen in een stroom (jet) van deeltjes.

In de meest directe benadering worden prompte fotonen geproduceerd in een zgn. quark-gluon Compton proces (met een inkomend quark en een inkomend gluon, en een uitgaand foton plus quark), in een quark anti-quark annihilatie process, waarbij een foton en gluon gemaakt worden. Tenslotte is er ook het fragmentatie proces, waarbij een photon door een quark wordt afgestraald. Dit proces is minder belangrijk, en wordt niet verder besproken.

Het blijkt dat de beste theoretische voorspellingen voor het prompt foton proces, waarin de eerste orde correcties zijn meegenomen (next-to-leading order), de data van experimenten bij fixed target en collider versnellers niet goed kunnen verklaren. Het lijkt erop dat bij die data waarbij het prompte foton een lage transversale impuls heeft, een grote rol door de zachte gluonen gespeeld wordt. In de twee eerste hoofdstukken van dit proefschrift wordt het kader van hersommatie van zachte gluon effecten opgesteld en uitgebreid het meenemen met soft-collineaire

effekten, en vervolgens toegepast op prompt foton produktie. Een definitieve conclusie over overeenstemming van theorie en data kan echter nog niet getrokken worden.

Single Top Productie

Het hoofdbestanddeel van dit proefschrift bestaat uit de fysica van enkelvoudige geproduceerde (single) top quarks en de geavanceerde simulatie technieken die gebruikt worden om meer precieze voorspellingen van observabelen in dit verband te kunnen doen. De produktie van losse top quarks (in tegenstelling tot top anti-top paarproduktie) is nog niet met zekerheid geobserveerd in versnellerexperimenten. Dit proces is heel belangrijk in de verdere studie van het Standaard Model, omdat het beschouwd kan worden als een mogelijke poort naar nieuwe ontdekkingen.

In hoofdstuk 4 worden next-to-leading order QCD resultaten voor de single-top produktie in proton botsingen gecombineerd met zgn. parton shower Monte Carlo simulaties. Dit wordt gedaan in het MC@NLO kader, waarin next-to-leading order en parton shower beschrijvingen zo gecombineerd worden dat er geen bijdrage dubbelgeteld wordt, en de beste aspecten van beide beschrijvingen overeind blijven. Dit kader wordt in dit hoofstuk verder uitgebreid met processen met collineaire divergenties in de eindtoestand, denk aan eerdergenoemde jets. Er wordt aangetoond, dat het MC@NLO kader ook na uitbreiding goed functioneert.

Correlaties in de hoekverdelingen van deeltjes in de eindtoestand bij het vervallen van vector bosonen en top quarks zijn van groot belang in het begrijpen van de single top quark produktie dynamica. In hoofdstuk 5 wordt via het beschouwen van lepton-paren die onstaan uit zulke vervallen, uitgewerkt hoe hoekcorrelaties in een Monte Carlo parton shower programma, eventueel gecombineerd met next-to-leading order QCD berekeningen, efficient ingebouwd kunnen worden. In het geval van top quark verval wordt ook de informatie van de resulterende bottom quarks behouden. Resultaten van de implementatie in MC@NLO worden getoond.

In hoofdstuk 6 wordt de berekening van een belangrijk single-top proces, de produktie van een W boson samen met een top quark, tot op next-to-leading orde beschreven. Daarnaast wordt de interface met de parton shower beschrijving en implementatie in MC@NLO afgeleid. Dit Wt-process geeft een unieke blik op de interactie van een top quark, bottom quark en een W-boson. Met de LHC, die naar verwachting in 2008 zal opstarten, zal dit process ook experimenteel bestudeert kunnen worden.

Acknowledgments

To begin with I would like to thank my supervisor prof. Eric Laenen. Besides always being available for helping and giving advise, he often spent considerable amount of time on discussing and explaining adjacent topics, thereby broadening my horizon. Also, I enjoyed our weekly jogging which gave an opportunity to discuss topics such as history, linguistics and life in general.
I wish to thank the people in the Theory Group at Nikhef for, first of all, being a nice bunch of people and, secondly, helping in creating a scientifically stimulating and informal environment.

Despite of being located at the edge of Amsterdam, almost detached from the city, Nikhef has offered a rich social life. Especially I will be remembering the coffee breaks after lunch and at 3 o'clock p.m. where everything between Heaven and Earth... and beyond has been discussed and laughed of. Furthermore I spent significant amounts of time with Sipho, Duncan, Aras, Marcello, Sascha, Freya, Jeroen, Jeroen, Claudine, Gordon and many others both during working hours as well as in the spare-time. Thanks for some really good times!
During my stay in the Netherlands I have been member of a fine rock band, bearing the noble name On Leaf of Absynthe. And what does that have to do with this thesis, one might ask? Fair question. The band AC/DC made it clear to the World that "It's A Long Way To The *Top* (If you Wanna Rock 'n' Roll)". To this I can add that sometimes when one goes for the *top* it can be pretty far away from Rock 'n' Roll. So what I am trying to say is, that On Leaf of Absynthe was something that helped me finding the balance between (the) *top* and Rock 'n' Roll. In this context I would especially like to thank Wouter Vijvers, Alexis Gillett, Erik Wessels and Chris White: Guys thanks for some really good times, lots of fun and for putting up with the amplifiers being turned up to 11 so many times! And speaking of music also I should mention my music-collector-partner-in-crime, Cedran, who always eagerly informs me about *new* releases of *old* rock music this way keeping me up(down?) to date.

In particular I owe many thanks to my dear parents, Jerzy and Urszula, for their

unconditional love, support and understanding, and for having faith in me and my abilities. Z całego serca pragnę Was podziękować za Waszą miłość, za nieograniczoną troskę, za to że zawsze mogłem na Was polegać i za to że zawsze stwarzaliście najlepsze warunki dla mojego brata i mnie do nauki i osobistego rozwoju. To dla Was, kochani rodzice, poświęcam tę pracę.

I also thank my brother, Brian, from the bottom of my heart for always being ready to help and support me. Tusind tak, broder!

Last but not least I would like to thank my beloved girlfriend, Anna Širillová, for her love, care, great support, patience and understanding during the process of making this thesis.